

**ATOMISTIC MODELING AND SIMULATION OF
NANOPOLYCRYSTALLINE SOLIDS**

by Zidong Yang

B.S. in Biological Science, June 2009, Wuhan University

B.S. in Mechanical Engineering, June 2009, Huazhong University of Science and
Technology

A Dissertation Submitted to

The Faculty of
The School of Engineering and Applied Science
of The George Washington University in partial fulfillment
of the requirements for the degree of Doctor of Philosophy

Jan 31, 2015

Dissertation directed by

James D. Lee
Professor of Engineering and Applied Science
and

Azim Eskandarian
Professor of Engineering and Applied Science

UMI Number: 3680325

All rights reserved

INFORMATION TO ALL USERS

The quality of this reproduction is dependent upon the quality of the copy submitted.

In the unlikely event that the author did not send a complete manuscript and there are missing pages, these will be noted. Also, if material had to be removed, a note will indicate the deletion.



UMI 3680325

Published by ProQuest LLC (2015). Copyright in the Dissertation held by the Author.

Microform Edition © ProQuest LLC.

All rights reserved. This work is protected against unauthorized copying under Title 17, United States Code



ProQuest LLC.
789 East Eisenhower Parkway
P.O. Box 1346
Ann Arbor, MI 48106 - 1346

The School of Engineering and Applied Science of The George Washington University certifies that Zidong Yang has passed the Final Examination for the degree of Doctor of Philosophy as of Dec 16, 2014. This is the final and approved form of the dissertation.

ATOMISTIC MODELING AND SIMULATION OF NANOPOLYCRYSTALLINE SOLIDS

Zidong Yang

Dissertation Research Committee:

James D. Lee, Professor of Engineering and Applied Science,
Dissertation Co-Director

Azim Eskandarian, Professor of Engineering and Applied Science,
Dissertation Co-Director

Michael Plesniak, Professor of Engineering and Applied Science,
Committee Member

Yongsheng Leng, Associate Professor of Engineering and Applied Science,
Committee Member

Saniya LeBlanc, Assistant Professor of Engineering and Applied Science,
Committee Member

James Chen, Assistant Professor of Mechanical Engineering and Material
Sciences, The Pennsylvania State University, Altoona,
Committee Member

© Copyright 2014 by Zidong Yang
All rights reserved

DEDICATION

To my dear grandmother Wang and my dear grandfather Ye
for their everlasting love.

ACKNOWLEDGEMENTS

I would like to thank my advisor Prof. James Lee and co-advisor Prof. Azim Eskandarian for their motivation, guidance, and support. I would like to extend my gratitude to Prof. Plesniak, Prof. Leng, Prof. Chen and Prof. LeBlanc for serving on the committee.

I would like to express my sincere gratitude to every one of the research group: Prof. Xianqiao Wang, Prof. James Chen, Dr. Yajie Lei, Xianyan Chen, Tejas Ruparel, Leyu Wang, Jiaoyan Li, Zhen Zhang, Der-you Kao, and William Jessup.

I would like to thank my GWU fellows: Jian Li, Taisen Zhuang, Huachuan Wang, Junfeng Wang, Rongguang Xu, Liangwei Li and many others that have helped me in so many ways during my study at GWU.

I also would like to take this opportunity to thank Zephra Coles, Joyce Jeffrey, Cindy Arnold, Mark Wagner, William Rutkowski, and Tom Punte, who are part of MAE, for their longtime support.

My most heartfelt thanks go to my parents and my wife, without whom I would never have gone so far. Thank you for your great understanding and encouragement.

The author greatly appreciates the support from the Federal Highway Administration of the US Department of Transportation under the award No. DTFH61-10-H-00005.

ABSTRACT

ATOMISTIC MODELING AND SIMULATION OF NANOPOLYCRYSTALLINE SOLIDS

In the past decades, nanostructured materials have opened new and fascinating avenues for research. Nanopolycrystalline solids, which consist of nano-sized crystalline grains and significant volume fractions of amorphous grain boundaries, are believed to have substantially different response to the thermal-mechanical-electric-magnetic loads, as compared to the response of single-crystalline materials. Nanopolycrystalline materials are expected to play a key role in the next generation of smart materials.

This research presents a framework (1) to generate full atomistic models, (2) to perform non-equilibrium molecular dynamics simulations, and (3) to study multi-physics phenomena of nanopolycrystalline solids. This work starts the physical model and mathematical representation with the framework of molecular dynamics. In addition to the latest theories and techniques of molecular dynamics simulations, this work implemented principle of objectivity and incorporates multi-physics features. Further, a database of empirical interatomic potentials is established and the combination scheme for potentials is revisited, which enables investigation of a broad spectrum of chemical elements (as in periodic table) and compounds (such as rocksalt, perovskite, wurtzite, diamond, etc.). The configurational model of nanopolycrystalline solids consists of two spatial components: (1) crystalline grains, which can be obtained through crystal structure optimization, and (2)

amorphous grain boundaries, which can be obtained through amorphization process. Therefore, multi-grain multi-phase nanopolycrystalline material system can be constructed by partitioning the space for grains, followed by filling the inter-grain space with amorphous grain boundaries.

Computational simulations are performed on several representative crystalline materials and their mixture, such as rocksalt, perovskite and diamond. Problems of relaxation, mechanical loading, thermal stability, heat conduction, electrical field response, magnetic field response are studied. The simulation results of the mechanical, thermal, electrical and magnetic properties are expected to facilitate the rational design and application of nanostructured materials.

TABLE OF CONTENTS

| | |
|--|-------------|
| DEDICATION..... | iv |
| ACKNOWLEDGEMENTS..... | v |
| ABSTRACT | vi |
| TABLE OF CONTENTS..... | viii |
| LIST OF FIGURES..... | xiv |
| LIST OF TABLES..... | xx |
| LIST OF ACRONYMS..... | xxi |
| LIST OF SYMBOLS..... | xxii |
| UNIT CONVERSION..... | xxiv |
| CHAPTER 1: INTRODUCTION..... | 1 |
| 1.1 Introduction to Nanopolycrystalline Solids | 1 |
| 1.1.1 Crystallites | 2 |
| 1.1.2 Polymorphism..... | 4 |
| 1.1.3 Grain Boundaries..... | 6 |
| 1.2 Previous Research..... | 7 |

| | |
|---|-----------|
| 1.2.1 Experimental Work | 7 |
| 1.2.2 Numerical Modeling and Simulation..... | 9 |
| 1.3 Challenges..... | 13 |
| 1.4 Goal and Objective | 15 |
| CHAPTER 2: MOLECULAR DYNAMICS SIMULATION..... | 16 |
| 2.1 Classical Molecular Dynamics Simulations | 17 |
| 2.2 Non-Equilibrium Molecular Dynamics Simulations..... | 19 |
| 2.2.1 Temperature in Molecular Dynamics | 20 |
| 2.2.2 Thermostat Algorithms | 22 |
| 2.2.2.1 Velocity rescaling..... | 23 |
| 2.2.2.2 Berendsen Thermostat..... | 25 |
| 2.2.2.3 Gaussian Constraints..... | 25 |
| 2.2.2.4 Nose-Hoover thermostat | 26 |
| 2.3 Objectivity Incorporated Molecular Dynamics | 27 |
| 2.3.1 Groundwork of Objectivity..... | 28 |
| 2.3.2 Objectivity Incorporated Molecular Dynamics | 30 |
| 2.4 Molecular Dynamics in Electromagnetic Field | 33 |
| 2.4.1 Governing Equation | 33 |
| 2.4.2 Maxwell Equation at Atomic Scale | 34 |
| 2.4.3 Induced Electromagnetic Quantities | 35 |
| 2.5 Numerical Procedure for MD Simulations | 36 |
| 2.5.1 Simple Procedure of Classical MD..... | 36 |

| | |
|---|-----------|
| 2.5.2 Velocity Verlet Method..... | 38 |
| 2.5.3 Heun's Method..... | 39 |
| 2.5.4 Inverse Method for MD in EM Field..... | 40 |
| 2.6 Summary | 42 |
| CHAPTER 3: MOLECULAR MECHANICS FORCE FIELDS..... | 43 |
| 3.1 Empirical Interatomic Potentials..... | 44 |
| 3.1.1 Coulomb Interaction..... | 44 |
| 3.1.1.1 Computational Methods for Coulomb Interaction | 45 |
| 3.1.2 Two-Body Potentials..... | 53 |
| 3.1.3 Many Body Potentials | 57 |
| 3.2 Parameters for Empirical Interatomic Potentials..... | 61 |
| 3.2.1 Parametrization Methods and Data Source..... | 61 |
| 3.2.2 Combining Scheme | 68 |
| 3.2.3 Remedy to Avoid Buckingham Catastrophe | 82 |
| 3.3 Summary | 83 |
| CHAPTER 4: NANOPOLYCRYSTALLINE MATERIAL SYSTEM..... | 85 |
| 4.1 Crystal Structures..... | 86 |
| 4.1.1 Rocksalt | 86 |
| 4.1.2 Perovskite..... | 87 |
| 4.1.3 Wurtzite | 88 |
| 4.1.4 Pyrochlore..... | 90 |

| | |
|--|------------|
| 4.2 Structural Optimization of Crystals..... | 90 |
| 4.3 Geometric Modeling of Nanopolycrystals..... | 93 |
| 4.3.1 Generating Crystalline Grains..... | 95 |
| 4.3.1.1 Voronoi Method | 95 |
| 4.3.1.2 Grain Nucleation Method..... | 98 |
| 4.3.2 Grain Orientation and Euler Angles | 100 |
| 4.3.3 Generating Amorphous Grain Boundaries | 103 |
| 4.3.4 Combining Grains and Grain Boundaries..... | 104 |
| 4.4 Characterization of Nanopolycrystals | 104 |
| 4.4.1 Characterizing Indices | 104 |
| 4.4.2 Examples..... | 105 |
| 4.5 Summary | 108 |
| CHAPTER 5: SIMULATED BEHAVIORS OF NANOPOLYCRYSTALS..... | 109 |
| 5.1 Mechanical Behaviors | 109 |
| 5.1.1 Simple Tests on Single Nanocrystalline Solids..... | 109 |
| 5.1.1.1 Simple Tension..... | 112 |
| 5.1.1.2 Simple Compression | 115 |
| 5.1.1.3 Simple Shear..... | 119 |
| 5.1.2 Mechanical Loading on Nanopolycrystals | 121 |
| 5.2 Thermal Behaviors..... | 125 |
| 5.2.1 Thermal Behaviors with Uniform Heat Bath | 125 |
| 5.2.1.1 Relaxation to Near Absolute Zero Temperature | 125 |

| | |
|--|------------|
| 5.2.1.2 Heating..... | 127 |
| 5.2.1.3 Melting..... | 129 |
| 5.2.1.4 Cooling and Grain Growth..... | 133 |
| 5.2.2 Heat Conduction..... | 136 |
| 5.3 Electromagnetic Behaviors..... | 141 |
| 5.3.1 Electric Effects..... | 142 |
| 5.3.2 Magnetic Effects..... | 143 |
| 5.3.2.1 Response to Magnetic Field at Zero Temperature | 143 |
| 5.3.2.2 Response to Magnetic Field at Non-Zero Temperature..... | 143 |
| 5.4 Summary | 149 |
| CHAPTER 6: CONCLUSION AND FUTURE WORK | 150 |
| 6.1 Conclusion | 150 |
| 6.1.1 Non-equilibrium molecular dynamics | 150 |
| 6.1.2 Numerical scheme | 151 |
| 6.1.3 Interatomic potential database..... | 152 |
| 6.1.4 Structure optimization and prediction of multiple phases of crystallites..... | 153 |
| 6.1.5 Multi-grain nanopolycrystalline material system..... | 154 |
| 6.1.6 Simulated behaviors | 155 |
| 6.2 Recommendations for Future Studies..... | 157 |
| 6.2.1 Parametric studies of material properties influenced by different interatomic potentials and potential parameters..... | 158 |
| 6.2.2 Parametric studies of material behaviors influenced by structural variables.... | 158 |

| | |
|---|------------|
| 6.2.3 Thermo-mechanical-electrical-magnetic coupling..... | 159 |
| BIBLIOGRAPHY..... | 160 |
| APPENDICES..... | 176 |
| APPENDIX - I PROOF OF THE OBJECTIVITY OF THE THERMAL VELOCITY..... | 176 |
| APPENDIX - II DERIVATION OF FICTITIOUS FORCE AND PROOF OF THE OBJECTIVITY OF THE DIFFERENCE BETWEEN THE APPARENT ACCELERATION AND THE FICTITIOUS FORCE-INDUCED ACCELERATION..... | 182 |
| APPENDIX - III FLOW CHART OF PROGRAM POLY | 186 |

LIST OF FIGURES

| | |
|---|----|
| <p>Figure 1-1: Polycrystalline structures composed of crystallites. Clockwise from top left a) malleable iron b) electrical steel without coating c) Solar cells made of polycrystalline silicon d) galvanized surface of zinc e) Micrograph of acid etched metal highlighting grain boundaries.....</p> | 3 |
| <p>Figure 1-2: Illustration of the microstructure of crystalline, polycrystalline and amorphous.....</p> | 3 |
| <p>Figure 1-3: SiO₂ exists in many crystalline forms (called polymorphs). (Red balls are oxygen atoms and gray balls are silicon atoms.).....</p> | 5 |
| <p>Figure 1-4: A cross-section of a deformed 12 nm grain size Ni sample containing 15 grains. Light grey atoms indicate the grains, black the grain boundary regions, and dark grey the hexagonal close-packed atoms [21].....</p> | 10 |
| <p>Figure 1-5: The twinned nc-Al sample with an average grain diameter of 12 nm [27]</p> | 12 |
| <p>Figure 3-1: Potential energy vs. R (cutoff). Different lines represent different values of α (R in units of Å, and α in units of Å^{-1}).....</p> | 50 |
| <p>Figure 3-2: Potential energy vs. α (damping). Different lines represent different values of R (R in units of Å, and α in units of Å^{-1})</p> | 51 |
| <p>Figure 3-3: Protocols that link different data sources of potential parameters.</p> | 69 |
| <p>Figure 3-4: Potential energy and force profiles of O²⁻ – O²⁻ with the parameters from Table 3-11</p> | 71 |

| | |
|--|----|
| Figure 3-5: Potential energy and force profiles of 1 st set, 3 rd set of O ²⁻ – O ²⁻ and their interpolation by common combination rule (Mirskaya) | 73 |
| Figure 3-6: Potential energy and force profiles of 1 st set, 2 nd set of O ²⁻ – O ²⁻ and their optimal interpolation | 76 |
| Figure 3-7: Potential energy and force profiles of 1 st set, 3 rd set of O ²⁻ – O ²⁻ and their optimal interpolation | 77 |
| Figure 3-8: Potential energy and force profiles of 1 st set, 4 th set of O ²⁻ – O ²⁻ and their optimal interpolation | 78 |
| Figure 3-9: Potential energy and force profiles of 2 nd set, 3 rd set of O ²⁻ – O ²⁻ and their optimal interpolation | 79 |
| Figure 3-10: Potential energy and force profiles of 2 nd set, 4 th set of O ²⁻ – O ²⁻ and their optimal interpolation | 80 |
| Figure 3-11: Potential energy and force profiles of 3 rd set, 4 th set of O ²⁻ – O ²⁻ and their optimal interpolation | 81 |
| Figure 4-1: Structure of rocksalt (e.g. MgO) | 87 |
| Figure 4-2: Structure of perovskite (ABO ₃)..... | 88 |
| Figure 4-3: Structure of perovskite (ABO ₃)..... | 89 |
| Figure 4-4: A 2D Voronoi diagram with 20 seeds and associated cells..... | 96 |
| Figure 4-5: The schematic arrangement of atoms by Voronoi method (Left picture shows the grain partition, right picture shows the filling of the first grain) | 97 |

| | |
|--|-----|
| Figure 4-6: Nano-polycrystalline block of 1.6 million atoms generated using Voronoi method | 97 |
| Figure 4-7: The schematic arrangement of atoms by grain nucleation method..... | 99 |
| Figure 4-8: Nanopolycrystalline block of 0.33 million atoms generated using grain nucleation method | 100 |
| Figure 4-9: Proper Euler angles representing rotations about z, N, and Z axes. The xyz (original) system is shown in blue, the XYZ (rotated) system is shown in red. The line of nodes (N) is shown in green. | 102 |
| Figure 4-10: A series of section view from back to front of a block of polycrystal..... | 106 |
| Figure 4-11: Configuration of a 15 grain polycrystal | 106 |
| Figure 4-12: (a) Centrosymmetric parameter (b) Resultant force (c) Coordination number (d) Von Mises stress (based on Virial stress)..... | 107 |
| Figure 5-1: Schematic drawing of the specimen with three types of mechanical loadings..... | 110 |
| Figure 5-2: The loading history of the displacement specified boundary condition | 111 |
| Figure 5-3: Structural evolution of MgO specimen under tensile loading..... | 112 |
| Figure 5-4: History of the boundary force of the MgO specimen under tensile loading.... | 114 |
| Figure 5-5: History of T_{33} component of the virial stress, averaged over the center part of the MgO specimen under tensile loading | 115 |
| Figure 5-6: Structural evolution of MgO specimen under compressive loading..... | 116 |

| | |
|--|-----|
| Figure 5-7: History of the boundary force of the MgO specimen under compressive loading..... | 117 |
| Figure 5-8: History of T_{33} component of the virial stress, averaged over the center part of the MgO specimen under compressive loading. | 118 |
| Figure 5-9: Structural evolution of MgO specimen under shear loading..... | 120 |
| Figure 5-10: History of the boundary force of the MgO specimen under shear loading.... | 120 |
| Figure 5-11: History of T_{13} component of the virial stress, averaged over the center part of the MgO specimen under shear loading..... | 121 |
| Figure 5-12: A nanopolycrystalline specimen, consisting of 10 grains, and the displacement specified boundary condition..... | 122 |
| Figure 5-13: Structural evolution of nanopolycrystalline specimen under mechanical loading..... | 124 |
| Figure 5-14: A nanopolycrystalline specimen of 15 grains (MgO + CaO). This figure shows the initial configuration (before relaxation)..... | 126 |
| Figure 5-15: A nanopolycrystalline specimen of 15 grains (MgO + CaO). This figure shows the relaxed configuration (after damped relaxation). $T \approx 0$ K. | 127 |
| Figure 5-16: Temperature history of the nanopolycrystalline specimen during the heating process. | 128 |
| Figure 5-17: A nanopolycrystalline specimen of 15 grains (MgO + CaO). This figure shows the configuration when it is heated up to $T = 2,000$ K..... | 129 |

| | |
|--|-----|
| Figure 5-18: Temperature history of the nanopolycrystalline specimen during the continued heating process. | 131 |
| Figure 5-19: A nanopolycrystalline specimen of 15 grains (MgO + CaO). This figure shows the configuration at T = 3,000 K, which is a few moment before melting. | 132 |
| Figure 5-20: A nanopolycrystalline specimen (MgO + CaO). This figure shows the melted configuration at T = 4,000 K..... | 133 |
| Figure 5-21: A slab of nanopolycrystals, with grains of 2-D Voronoi pattern. This figure shows the initial configuration. | 134 |
| Figure 5-22: A slab of nanopolycrystals, with grains of 2-D Voronoi pattern. This figure shows the configuration at T = 2,000 K..... | 135 |
| Figure 5-23: A slab of nanopolycrystals, with grains of 2-D Voronoi pattern. This figure shows the final configuration after cooling process. | 135 |
| Figure 5-24: A slab of nanopolycrystalline specimen consisting of MgO and CaO. | 136 |
| Figure 5-25: Schematics of distributed temperatures control – heat conduction case-1 | 137 |
| Figure 5-26: Temperature distribution after a long time simulation – Heat conduction case-1 | 138 |
| Figure 5-27: Temperature history by groups – Heat conduction case-1 | 139 |
| Figure 5-28: Schematics of distributed temperature control – heat conduction case-2..... | 140 |

| | |
|---|-----|
| Figure 5-29: Temperature distribution after a long time simulation – Heat conduction case-2 | 140 |
| Figure 5-30: History of linear momentum of a material body under the effect of a magnetic field $\mathbf{B} = (1, 0, 0)$ | 144 |
| Figure 5-31: History of angular momentum of a material body under the effect of a magnetic field $\mathbf{B} = (1, 0, 0)$ | 145 |
| Figure 5-32: History of linear momentum of a material body under the effect of a magnetic field $\mathbf{B} = (1, 1, 1)$ | 145 |
| Figure 5-33: History of angular momentum of a material body under the effect of a magnetic field $\mathbf{B} = (1, 1, 1)$ | 146 |
| Figure 5-34: History of linear momentum of a material body under the effect of a magnetic field $\mathbf{B} = (1, 1, 1)$, as obtained by inversed method..... | 148 |
| Figure 5-35: History of angular momentum of a material body under the effect of a magnetic field $\mathbf{B} = (1, 1, 1)$, as obtained by inversed method..... | 148 |

LIST OF TABLES

| | |
|--|----|
| Table 3-1: Buckingham potential parameter, Lewis et al (1985)..... | 62 |
| Table 3-2: Buckingham potential parameter, Collins et al (1992)..... | 62 |
| Table 3-3: Buckingham potential parameter, Bush et al (1994)..... | 63 |
| Table 3-4: Buckingham potential parameter, Perovskite $A^{3+}B^{3+}O_3$ – Grimes (2004)..... | 64 |
| Table 3-5: Buckingham potential parameter, Pyrochlore - Grimes (2002)..... | 65 |
| Table 3-6: Buckingham potential parameters for $PbTiO_3$ | 66 |
| Table 3-7: Buckingham potential parameters for $BaTiO_3$ | 66 |
| Table 3-8: Buckingham potential parameters for $BiScO_3$ | 67 |
| Table 3-9: Buckingham potential parameters for $KNbO_3$ | 67 |
| Table 3-10: Buckingham potential parameters for $KTaO_3$ | 67 |
| Table 3-11: $O^{2-} - O^{2-}$ parameters from four sources..... | 70 |
| Table 3-12: The combination rule of mixing $O^{2-} - O^{2-}$ parameters from the data sets in Table 3-11..... | 75 |
| Table 3-13: Periodic table (red colored elements are covered in the potential parameter database)..... | 84 |
| Table 4-1: Structural Optimization Results and Experimental Results for Several Crystals..... | 93 |

LIST OF ACRONYMS

| | |
|---------------|---|
| MD | Molecular Dynamics |
| NEMD | Non-Equilibrium Molecular Dynamics |
| OIMD | Objectivity Incorporated Molecular Dynamics |
| NH thermostat | Nose-Hoover thermostat |
| SW potential | Stillinger-Weber potential |
| EM field | Electromagnetic Field |
| A.U. | Atomic Unit |

LIST OF SYMBOLS

| | |
|------------------------------------|---|
| m^i | mass of atom i |
| \mathbf{r}^i | position of atom i |
| $\mathbf{v}^i, \dot{\mathbf{r}}^i$ | velocity of atom i |
| \mathbf{f}^i | force on atom i |
| V | potential energy |
| K | kinetic energy |
| \mathbf{x} | position vector |
| $\mathbf{Q}(t)$ | time dependent orthogonal transformation tensor |
| $\mathbf{b}(t)$ | time dependent translation |
| δ_{ij} | Kronecker delta |
| $\tilde{\mathbf{v}}$ | thermal velocity or objective velocity |
| \mathbf{i} | fictitious force |
| Ω | volume of the region |
| T | temperature |

k_b Boltzmann constant

σ stress tensor

p pressure

\mathbf{E} electric field

\mathbf{B} magnetic field

UNIT CONVERSION

Atomic units (A.U.) form a system of natural units which is especially convenient for atomic physics calculations. For this reason, most of the units used in this work are atomic units (A.U.). The conversions between some atomic units and SI units are listed as follows:

$$1 \text{ A.U. mass} = 9.110 \times 10^{-31} \text{ kg}$$

$$1 \text{ A.U. charge} = 1.602 \times 10^{-19} \text{ C}$$

$$1 \text{ A.U. angular momentum} = 1.055 \times 10^{-34} \text{ J}\cdot\text{s}$$

$$1 \text{ A.U. momentum} = 1.993 \times 10^{-24} \text{ kg}\cdot\text{m}\cdot\text{s}^{-1}$$

$$1 \text{ A.U. length} = 1 \text{ Bohr} = 5.292 \times 10^{-11} \text{ m}$$

$$1 \text{ A.U. energy} = 1 \text{ Hartree} = 4.360 \times 10^{-18} \text{ J}$$

$$1 \text{ A.U. force} = 0.824 \times 10^{-7} \text{ N}$$

$$1 \text{ A.U. time} = 2.419 \times 10^{-17} \text{ s}$$

$$1 \text{ A.U. temperature} = 1.0 \text{ K}$$

$$1 \text{ A.U. pressure} = 2.942 \times 10^{13} \text{ Pa}$$

$$1 \text{ A.U. electric field} = 5.142 \times 10^9 \text{ V}\cdot\text{cm}^{-1}$$

$$1 \text{ A.U. magnetic field} = 2.351 \times 10^9 \text{ Gauss}$$

CHAPTER 1: INTRODUCTION

1.1 Introduction to Nanopolycrystalline Solids

Nanopolycrystalline materials in general are single- or multi-phase polycrystalline solids with a grain size of a few nanometers ($1 \text{ nm} = 10^{-9} \text{ m} = 10 \text{ \AA}$), typically less than 100 nm [1]. Since the grain sizes are so small, a significant volume of the microstructure in nanopolycrystalline materials is composed of interfaces, mainly grain boundaries, i.e., a large volume fraction of the atoms resides in grain boundaries. Consequently, nanopolycrystalline materials exhibit properties that are significantly different from, and often improved over, their conventional coarse-grained polycrystalline counterparts. Materials with microstructural features of nanometric dimensions are referred to in the literature as nanocrystalline materials (a very generic term), nanocrystals, nanostructured materials, nanophase materials, nanometer-sized crystalline solids, or solids with nanometer-sized microstructural features [2]. This research is dealing with solids of nanometric dimensions, with grains made up of crystals and grain boundaries made up of amorphous phase atoms, thus the term “nanopolycrystalline solids” is adopted to best describe the features of these materials.

1.1.1 Crystallites

Polycrystals, as commonly seen in most metals, ceramics, ice, rocks, etc., are made of a large number of single crystals – crystallites. Figure 1-1 illustrates the polycrystalline materials in engineering applications. In a crystallite, constituent atoms, molecules, or ions are arranged in an ordered pattern extending in all three spatial dimensions. A crystal structure (an arrangement of atoms in a crystal) is characterized by its unit cell, a small imaginary box containing one or more atoms in a specific spatial arrangement. The unit cells are repeated at lattice points so as to stack up in three-dimensional space to form the crystal. Comparing to a single crystal, which has atoms in a near-perfect periodic arrangement, a polycrystal is composed of many microscopic crystals (called "crystallites" or "grains"), while an amorphous solid (such as glass) has no periodic arrangement even microscopically. Figure 1-2 illustrates the microstructure of crystalline, polycrystalline and amorphous.

The size of a crystal can vary from a few nanometers to several millimeters. Macroscopic solid objects that are large enough to see and handle are rarely composed of a single crystal, except for a few cases (gems, silicon single crystals for the electronics industry, etc.). In polycrystals, crystallites are usually referred to as grains, or grain cells. If the individual grains are oriented randomly, a large enough volume of polycrystalline material will be approximately isotropic. This property helps the simplifying assumptions of continuum mechanics to apply to real-world solids.

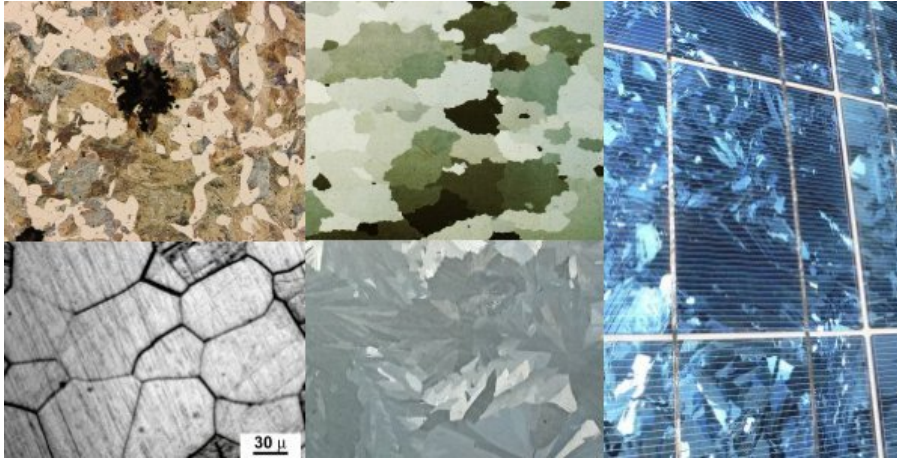


Figure 1-1: Polycrystalline structures composed of crystallites.
 Clockwise from top left a) malleable iron b) electrical steel without coating c) Solar cells made of polycrystalline silicon d) galvanized surface of zinc e) Micrograph of acid etched metal highlighting grain boundaries

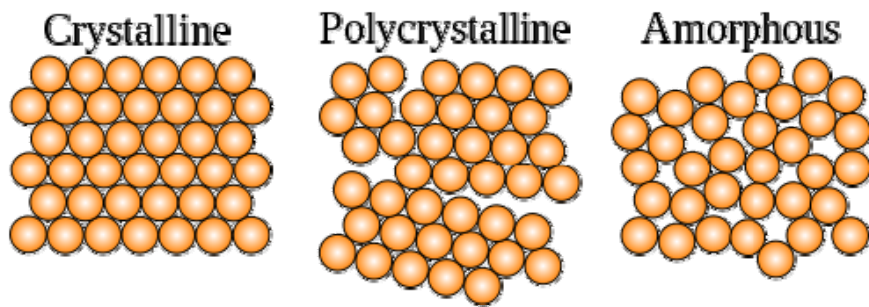


Figure 1-2: Illustration of the microstructure of crystalline, polycrystalline and amorphous

1.1.2 Polymorphism

The same group of atoms can often solidify in many different ways. Polymorphism refers to the ability of a solid to exist in more than one crystalline form or structure [3-5]. The different polymorphs are usually called different phases. According to Gibbs' rules of phase equilibria [6], these unique crystalline phases will be dependent on intensive variables such as pressure and temperature. Polymorphism can potentially be found in many crystalline materials including polymers, minerals, and metals, and is related to allotropy, which refers to different structural modification of an element.

One example of polymorphism is the quartz form of silicon dioxide, or SiO_2 . In the vast majority of silicates, the Si atom shows tetrahedral coordination by 4 oxygens. All but one of the crystalline forms involves tetrahedral SiO_4 units linked together by shared vertices in different arrangements. In different minerals the tetrahedra show different degrees of networking and polymerization. For example, they occur singly, joined together in pairs, in larger finite clusters including rings, in chains, double chains, sheets, and three-dimensional frameworks. The minerals are classified into groups based on these structures. In each of its 7 thermodynamically stable crystalline forms or polymorphs of crystalline quartz, only 2 out of 4 of each the edges of the SiO_4 tetrahedra are shared with others, yielding the net chemical formula for silica: SiO_2 .

Figure 1-3 shows only a few polymorphs of SiO_2 .

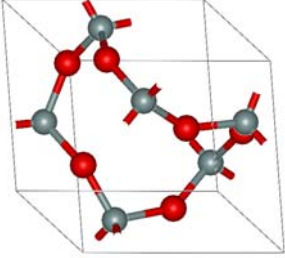

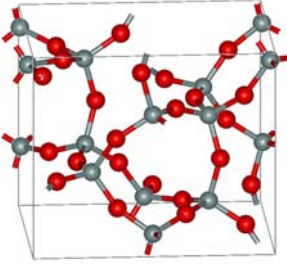
| Form | Crystal symmetry | Structure |
|------------------|------------------|--|
| α -quartz | rhombohedral |  |
| β -quartz | hexagonal |  |
| keatite | tetragonal |  |

Figure 1-3: SiO_2 exists in many crystalline forms (called polymorphs).

(Red balls indicate oxygen atoms, gray balls indicate silicon atoms.)

Polymorphs have different stabilities and may spontaneously convert from a metastable form (or thermodynamically unstable form) to the stable form at a particular temperature. They also exhibit different melting points, solubilities, and X-ray diffraction patterns [4].

Polymorphism is one of the most fascinating phenomena of solid state chemistry and indeed is a “difficult” phenomenon, studied for many decades mainly, and separately, in the fields of organic and inorganic chemistry. In spite of the huge efforts of many researchers our knowledge of the phenomenon is still embryonic, and the relationship between growth of a crystalline phase and nucleation of the first crystallites is often mysterious [5].

1.1.3 Grain Boundaries

Grain boundaries are interfaces between grains, or crystallites, in polycrystalline materials. The term "crystallite boundary" is sometimes, though rarely, used. Grain boundary areas contain those atoms that have been perturbed from their original lattice sites, dislocations, and impurities that have migrated to the lower energy grain boundary. In a polycrystal, each of the small grain is a true crystal with a periodic arrangement of atoms, but the whole polycrystal does not have a periodic arrangement of atoms, because the periodic pattern is broken at the grain boundaries.

Grain boundaries in general can be only a few nanometers wide. In common materials, crystallites are large enough that grain boundaries account for a small fraction of the material. However, very small grain sizes are achievable. In nanopolycrystalline solids, grain boundaries become a significant volume fraction of the material, with profound effects on such properties as diffusion and plasticity. In the limit of small crystallites, as the volume fraction of grain boundaries approaches 100%, the material ceases to have any crystalline character, and thus becomes an amorphous solid.

1.2 Previous Research

Nanopolycrystalline solids are of technological interest, mainly because their strength and hardness often are far above what is seen in coarse-grained polycrystalline materials and single-crystalline materials. The researchers are interested from a technological point of view, but also from a theoretical and computational point of view. Nanopolycrystalline solids have been an attractive group of materials to model for many years.

1.2.1 Experimental Work

Early in the 20th century, when “microstructures” were revealed primarily with the optical microscope, it was recognized that refined microstructures, for example, small grain sizes,

often provided attractive properties such as increased strength and toughness in structural materials. A classic example of property enhancement due to a refined microstructure – with features too small to resolve with the optical microscope – was age hardening of aluminum alloys. The phenomenon, discovered by Alfred Wilm in 1906 [7], was essentially explained by Merica, Waltenberg, and Scott in 1919 [8], and the microstructural features responsible first inferred by the X-ray studies of Guinier and Preston in 1938 [9,10]. With the advent of transmission electron microscopy [11] and sophisticated X-ray diffraction methods [12] it is now known that the fine precipitates responsible for age hardening. In later years also there are a number of other examples of nanoscale microstructures providing optimized properties. Gleiter and coworkers synthesized ultrafine-grained materials (with a grain size of a few nanometers) by the in situ consolidation of nanoscale atomic clusters and showed that these materials have properties significantly different from those of conventional grain sized ($>1\ \mu\text{m}$) polycrystalline or amorphous materials of the same chemical composition [13].

These technological findings and results stimulated research activities on different aspects of nanopolycrystalline materials. The subject of nanopolycrystalline materials has attracted the attention of materials scientists, physicists, chemists, mechanical engineers, electrical engineers, and chemical engineers [2].

However, in many cases, the nanocrystalline structures and deformation mechanisms operating in them cannot be unambiguously identified with the help of contemporary experimental methods, because of high precision demands on experiments at the atomic

and nanoscale levels. In these circumstances, analytical theoretical models and computer simulations of the structure, plastic deformation and fracture processes are very important for understanding the fundamental nature of the outstanding properties of nanopolycrystalline materials. Besides, the approach involving theoretical models and computer simulations can serve as a basis for development of high technologies exploiting the unique characteristics of nanopolycrystalline materials.

1.2.2 Numerical Modeling and Simulation

Beginning in the 1980s, there have been made many attempts to model the grain microstructure and especially the microstructural evolution under realistic conditions with the help of computer simulations.

In recent years, impressive results in atomistic simulations of nanopolycrystalline materials have been obtained. The most effective approach to atomistic simulations of nanocrystalline structures is recognized to be molecular dynamics [14-16]. With this approach, the real-time behaviors of diverse nanocrystalline structures under mechanical loads have been simulated.

The molecular dynamics operates with Newton's equations for systems consisting of millions of atoms whose interactions are calculated using prescribed interatomic interaction

potential functions. This approach accounts for crystal lattice anharmonicity and highly inhomogeneous internal stresses in deformed atomic structures [17,16].

Van Swygenhoven and her colleagues have pioneered the simulation of nanocrystalline metals. One of their earliest studies [18,19,14,20,21] and Yamakov et al [22,23,15] focused on nickel, with a mean grain size ranging from 3.4 to 12 nm with high angle grain boundaries, as shown in Figure 1-4. In an investigation of the role of the grain-boundary structure [19,18], simulations of nickel and copper with mean grain sizes ranging from 5 to 12 nm and high angle grain boundaries were performed.

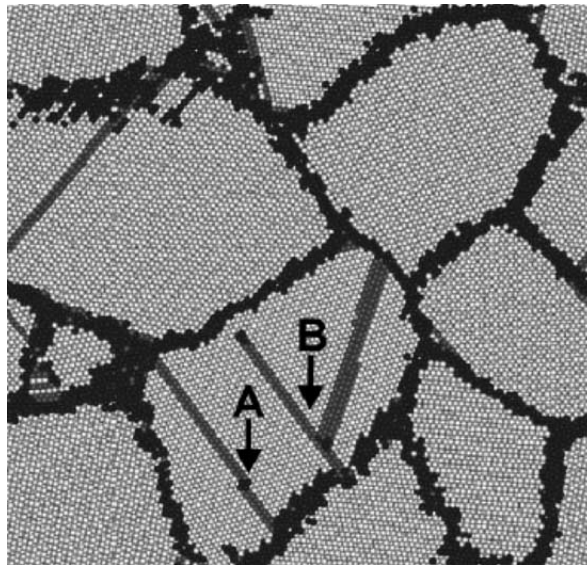


Figure 1-4: A cross-section of a deformed 12 nm grain size Ni sample containing 15 grains. Light grey atoms indicate the grains, black the grain boundary regions, and dark grey the hexagonal close-packed atoms [21]

An excellent summary of general results of molecular dynamics studies is presented in Derlet et al. [21]. They also remark that the grain boundaries are generally not equilibrium grain boundaries and are sensitive to how the grains are numerically synthesized. In their Voronoi-generated models, the grains are usually in compression and the grain boundaries in tension. However, there are regions of compression and tension in the grain boundaries depending on the misfit areas. Their summary [24] of the mechanical behavior of molecular dynamics simulations indicates that the plasticity is dominated by inter-grain deformation mechanisms below ~ 10 nm. They conclude that the only meaningful information that can be extracted from MD simulations is the classification of the atomic processes occurring during the deformation.

While most of the simulations of nanocrystalline materials involve uniaxial deformations, other dynamic phenomena have been studied. For example, Samaras et al. [25] explored the formation of stacking fault tetrahedra due to irradiation. Nanoindentation is investigated by defining a moving repulsive potential [26]. Froseth et al. depict the emission of individual partial dislocations from the grain boundary [27], as shown in Figure 1-5.

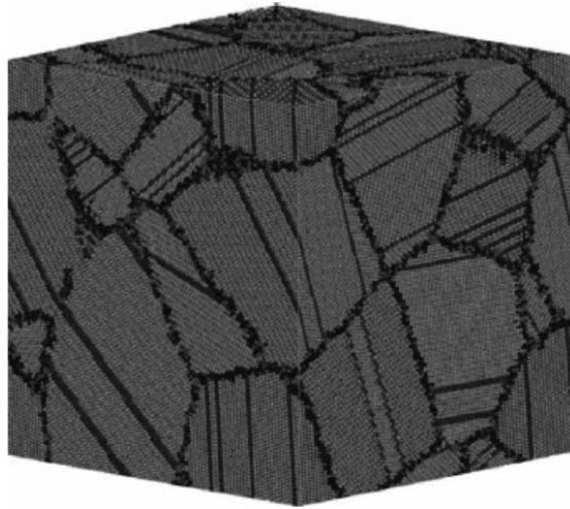


Figure 1-5: The twinned nc-Al sample with an average grain diameter of 12 nm [27]

Besides these attractive achievements, there are fundamental limitations of molecular dynamics approach. One limitation comes from the extremely short time window inherent to molecular dynamics simulations of real-time behavior and validity of prescribed interatomic interaction potentials. For instance, typical values of deformation time scale and strain rate handled by molecular dynamics are around 10 ns (10^{-8} s) and 10^7 s $^{-1}$, respectively. These values are unrealistic for most experiments on plastic deformation of nanopolycrystalline materials with typical strain rates ranging from 10^{-5} s $^{-1}$ to 10^3 s $^{-1}$. As a corollary, results of computer simulations of deformation processes in nanocrystalline structures are discussive. Also, unrealistically high strain-rate deformation simulated by molecular dynamics hardly involves thermally activated processes that often play a very important role in deformation and fracture of diverse materials especially at intermediate and high temperatures.

As to interatomic interactions, they are described by interaction potential functions of empirical or semi-empirical origin. Most atomistic simulations handle monatomic nanostructured solids. Their application to analysis of evolution of polyatomic and composite nanostructures is limited to difficulties in a correct description of interatomic interaction potentials in the case of two or more kinds of atoms.

Nevertheless, molecular-dynamics-based atomistic simulations of plastic deformation of nanocrystalline materials provide important information on possible structural transformations occurring in mechanically loaded nanopolycrystalline materials. This approach is considered to be one of effective methods of nanomaterials science and expected to grow rapidly in the future in parallel with progress in hardware and software of computer simulations.

1.3 Challenges

The physical properties of a nanopolycrystalline material are influenced by many factors, including (1) its chemical constituents, for example MgO or PbTiO₃, (2) its crystallite phases, for example wurtzite ZnO or Zincblende ZnO, and (3) its microstructure, for example grain-boundaries, dislocations and point defects. Accordingly, to generate atomistic models, which are sufficiently realistic in that they can be used to calculate properties or simulate processes with sufficient accuracy to be of benefit to experiment, the following challenges need to be overcome:

- 1) the first challenge is to find/establish a capable, credible and accurate physical model and mathematical representation that is suitable to solve a supposed atomistic material system (as a matter of theory),
- 2) the theory needs to incorporate multiple physics phenomena, such as thermal mechanical electrical magnetic effects (as a matter of theory),
- 3) the supposed material system may contain multiple kinds of chemical compounds, i.e. various elements as many as possible in periodic table (as a matter of parameters),
- 4) the supposed material system may contain multiple kinds of crystallites, each of which may have different chemical constituents and different crystalline phases (as a matter of modeling and structural optimization),
- 5) the supposed material system may contain both crystalline grains and amorphous grain boundaries (as a matter of geometric modeling),
- 6) the grains in the supposed material system may be randomly arranged with arbitrary geometric variables, such as distribution, size, shape, orientation (as a matter of geometric modeling),
- 7) the last challenge is to demonstrate that the devised method is applicable to solve many proposed problems for the supposed material system (as a matter of verification and demonstration)

1.4 Goal and Objective

The goal of this research is to explore, formulate, implement, verify and improve techniques in modeling and simulation of nanopolycrystalline material from atomistic basis. As a result, a systematic approach is to be established such that it can provide better insights into material behavior and structural responses under various conditions and loading scenarios.

The objectives of this research are:

- 1) to construct a multi-physics non-equilibrium molecular dynamics theory for atomistic material systems (to be addressed in Chapter 2),
- 2) to establish a database of interatomic potentials and potential parameters, and to validate the combination scheme for these interatomic potentials and potential parameters (to be addressed in Chapter 3),
- 3) to model the heterogeneous multi-grain multi-phase structure of nanopolycrystalline solids (to be addressed in Chapter 4), and
- 4) to demonstrate the capability, stability and accuracy of the proposed methodology in modeling and analysis of nanopolycrystalline solids (to be addressed in Chapter 5).

CHAPTER 2: MOLECULAR DYNAMICS SIMULATION

The computing power nowadays available enables simulations of large systems. The molecular dynamics (MD) simulation is a technique for computing the equilibrium and transport properties of a classical many-body system [28-31]. In MD, the trajectories of atoms are determined by numerically solving the Newton's equations of motion for a system of interacting atoms, where forces between the atoms and potential energy are defined by molecular mechanics force fields.

MD simulations can be very similar to real experiments in many aspects. When a real experiment is performed, the sample is connected to a measuring instrument, and the property of interest is measured during a certain time interval. If the measurements are subject to statistical noise, then the longer time they are averaged, the more accurate these measurements become. In fact, some of the most common mistakes that can be made when performing a computer experiment are very similar to the mistakes that can be made in real experiments (e.g. the sample is not prepared correctly, the measurement is too short, the system undergoes an irreversible change during the experiment, what are measured are not what are supposed to be measured). To measure an observable quantity in an MD simulation, first of all it must be able to show that this observable can be expressed as a function of the position or the momenta of the particles in the system. Secondly, it needs to

be confirmed that these expressions can be properly linked to macroscopic physical quantities.

In this chapter, the existing theories and techniques of classical molecular dynamics and non-equilibrium molecular dynamics (NEMD) are introduced and reviewed. Then, in addition to the existing method, several new features are proposed in this research to extend the credibility and capability in simulating nanopolycrystalline materials.

2.1 Classical Molecular Dynamics Simulations

In a classical MD simulation, for a model system consisting of n particles, Newton's equations of motion are solved until the properties of the system no longer change with time. The actual measurements are performed after equilibration.

The governing equation in classical molecular dynamics is

$$m^i \ddot{\mathbf{r}}^i = \mathbf{f}^i + \boldsymbol{\varphi}^i \quad i = 1, 2, 3, \dots, n \quad (2.1)$$

where n is the total number of atoms in the system; m^i , \mathbf{r}^i , and $\ddot{\mathbf{r}}^i$ are the mass, position vector and acceleration vector of atom i , respectively; \mathbf{f}^i and $\boldsymbol{\varphi}^i$ are the interatomic force and body force acting on atom i , respectively. Here it is emphasized that \mathbf{f}^i is the interatomic force acting on atom i due to the interaction between atom i and all the other

atoms in the system. Similar to stress tensor, which is the derivative of a scalar-valued function, named potential energy per unit volume or strain energy density function, with respect to strain tensor, in MD the interatomic force vector \mathbf{f}^i can also be expressed as the derivative of potential energy V with respect to the position vector \mathbf{r}^i as

$$V = V(\mathbf{r}^1, \mathbf{r}^2, \mathbf{r}^3, \dots, \mathbf{r}^n) \equiv V(\mathbf{r}) \quad (2.2)$$

$$\mathbf{f}^i = -\frac{\partial V}{\partial \mathbf{r}^i} \quad (2.3)$$

The total energy T of the system is equal to the sum of kinetic energy K and potential energy V :

$$\begin{aligned} T &= K + V \\ &= \sum_{i=1}^n \frac{1}{2} m^i \dot{\mathbf{r}}^i \cdot \dot{\mathbf{r}}^i + V(\mathbf{r}) \end{aligned} \quad (2.4)$$

The work done by the body force can be calculated as an integral

$$W(t) = \sum_{i=1}^n \int_0^t \boldsymbol{\phi}^i(\tau) \cdot \dot{\mathbf{r}}^i(\tau) d\tau \quad (2.5)$$

It is seen that the integrand is the inner product of the body force on atom i and velocity of atom i , which is equal to the rate of work done on atom i . One may readily show that

$$\begin{aligned}
\frac{dT}{dt} &= \frac{d(K+V)}{dt} = \sum_{i=1}^n m^i \ddot{\mathbf{r}}^i \cdot \dot{\mathbf{r}}^i + \sum_{i=1}^n \frac{dV(\mathbf{r})}{dt} \\
&= \left\{ \sum_{i=1}^n m^i \ddot{\mathbf{r}}^i + \sum_{i=1}^n \frac{dV(\mathbf{r})}{d\mathbf{r}^i} \right\} \dot{\mathbf{r}}^i \\
&= \left\{ \sum_{i=1}^n m^i \ddot{\mathbf{r}}^i - \sum_{i=1}^n \mathbf{f}^i \right\} \dot{\mathbf{r}}^i
\end{aligned} \tag{2.6}$$

$$\begin{aligned}
\frac{dW(t)}{dt} &= \sum_{i=1}^n \frac{d}{dt} \int_0^t \boldsymbol{\varphi}^i(\tau) \cdot \dot{\mathbf{r}}^i(\tau) d\tau \\
&= \sum_{i=1}^n \boldsymbol{\varphi}^i(t) \cdot \dot{\mathbf{r}}^i(t)
\end{aligned} \tag{2.7}$$

Finally it gives

$$\frac{dT}{dt} - \frac{dW}{dt} = \sum_{i=1}^n (m^i \ddot{\mathbf{r}}^i - \mathbf{f}^i - \boldsymbol{\varphi}^i) \cdot \dot{\mathbf{r}}^i = 0 \tag{2.8}$$

If the body force is zero, i.e., the system is isolated from its environment, then Eq.(2.8) says that the total energy is a constant. Eq.(2.8) is actually the law of conservation of energy in MD. Therefore, in a way, Eq.(2.1) and Eq.(2.3) define classical molecular dynamics.

2.2 Non-Equilibrium Molecular Dynamics Simulations

The MD method discussed aforementioned is a scheme for studying the natural time evolution of a classical system of N particles in volume V . In such simulations, the total

energy E is a constant. If it is assumed that time average are equivalent to ensemble average, then the time average obtained in a conventional MD simulation are equivalent to ensemble averages in the microcanonical (constant-NVE) ensemble. Unlike equilibrium molecular dynamics, non-equilibrium molecular dynamics (NEMD) provides a consistent microscopic basis for the irreversible macroscopic Second Law of Thermodynamics. The key idea to the development of NEMD was the replacement of external thermodynamics environment by internal control variables. The new variables can control temperature, or pressure, etc. These thermostat and barostat variables can control and maintain non-equilibrium states of the atomistic material system. Attribute to its capability and popularity, NEMD is a powerful simulation tool in modern nanoscience and nanotechnology.

2.2.1 Temperature in Molecular Dynamics

In molecular dynamics, temperature for a group of N atoms is calculated as

$$3Nk_B T(t; \Delta t) = \frac{1}{\Delta t} \int_{\tau=t}^{\tau+t+\Delta t} \sum_{i=1}^N m^i (\dot{\mathbf{u}}^i(\tau) - \bar{\mathbf{u}}^i) \cdot (\dot{\mathbf{u}}^i(\tau) - \bar{\mathbf{u}}^i) d\tau \quad (2.9)$$

where $\bar{\mathbf{u}}^i$ is the time-interval averaged velocity of atom i defined as

$$\bar{\mathbf{u}}^i(t; \Delta t) \equiv \frac{1}{\Delta t} \int_{\tau=t}^{\tau+t+\Delta t} \mathbf{u}^i(\tau) d\tau \quad (2.10)$$

k_B is the Boltzmann constant; m^i is the mass of atom i . It is seen that the temperature T according to this definition, Eq.(2.9), is the space-time average of the velocities of N atoms for a time period between t and $t + \Delta t$. It is worthwhile to note that the definition of temperature can be reduced to two special cases:

Space Averaged Temperature

$$3Nk_B T = \sum_{i=1}^N m^i (\mathbf{u}^i - \hat{\mathbf{u}}) \cdot (\mathbf{u}^i - \hat{\mathbf{u}}) \quad (2.11)$$

$$\hat{\mathbf{u}} \equiv \frac{\sum_{i=1}^N m^i \mathbf{u}^i}{M}, \quad M \equiv \sum_{i=1}^N m^i$$

Time Averaged Temperature [32,33]

$$3k_B T(t; \Delta t) = \frac{1}{\Delta t} \int_{\tau=t}^{\tau+t+\Delta t} m (\mathbf{u}(\tau) - \bar{\mathbf{u}}) \cdot (\mathbf{u}(\tau) - \bar{\mathbf{u}}) d\tau \quad (2.12)$$

$$\bar{\mathbf{u}}(t; \Delta t) \equiv \frac{1}{\Delta t} \int_{\tau=t}^{\tau+t+\Delta t} \mathbf{u}(\tau) d\tau$$

It is seen that, in MD, temperature is not an independent variable; instead it is derivable from the velocities of atoms. One may specify temperature as boundary conditions or consider the temperature of the whole system as a given function of time. For this purpose, a temperature control algorithm is needed.

2.2.2 Thermostat Algorithms

A modification of the Newtonian MD scheme with the purpose of generating a thermodynamical ensemble at constant temperature is called a thermostat algorithm. The use of a thermostat can be motivated by one (or a number) of the following reasons:

- (i) to match experimental conditions;
- (ii) to study temperature-dependent process (e.g., determination of thermal coefficients, investigation of temperature-dependent conformation or phase transitions);
- (iii) to evacuate the heat in dissipative non-equilibrium MD simulations (e.g., computation of transport coefficient η in viscous-flow or heat-flow simulations);
- (iv) to enhance the efficiency of a conformation search (e.g. high-temperature dynamics, simulated annealing);
- (v) to avoid steady energy drifts caused by the accumulation of numerical errors during MD simulations.

Popular techniques to control temperature include velocity rescaling [34-40], Anderson thermostat [41-49], Nosé-Hoover thermostat [50-58], Nosé-Hoover chains [59], stochastic

dynamics thermostat[60,61], Gaussian constraints [62,48], and the Berendsen thermostat [63-67].

In the following, several existing methods to implement MD simulation with given constraints due to the consideration of temperature are reviewed.

2.2.2.1 Velocity rescaling

Suppose, in the numerical procedure, at the n -th time step ($t = n\Delta t$) for a group of N atoms, it is found that

$$\begin{aligned}\bar{\mathbf{v}} &= \frac{1}{M} \sum_{i=1}^N m^i \mathbf{v}^i \\ T &= \frac{1}{3k_B N} \sum_{i=1}^N m^i (\mathbf{v}^i - \bar{\mathbf{v}})^2\end{aligned}\tag{2.13}$$

It is understood that this group of N atoms may or may not be the whole specimen. This enables the freedom to specify different kinds of boundary conditions. If the desired (specified) temperature is $T^* \neq T$, then the velocities of the N atoms are simply modified as

$$\mathbf{v}^{i*} = \sqrt{\frac{T^*}{T}} (\mathbf{v}^i - \bar{\mathbf{v}}) + \bar{\mathbf{v}}\tag{2.14}$$

while keeping the positions of the atoms unchanged. It is straightforward to check

$$\begin{aligned}\bar{\mathbf{v}}^* &= \frac{1}{M} \sum_{i=1}^N m^i \mathbf{v}^{i*} = \frac{1}{M} \sum_{i=1}^N m^i \left(\sqrt{T^*/T} (\mathbf{v}^i - \bar{\mathbf{v}}) + \bar{\mathbf{v}} \right) = \bar{\mathbf{v}} \\ \frac{1}{3k_B N} \sum_{i=1}^N m^i (\mathbf{v}^{i*} - \bar{\mathbf{v}}^*)^2 &= \frac{1}{3k_B N} \sum_{i=1}^N m^i \left(\sqrt{T^*/T} (\mathbf{v}^i - \bar{\mathbf{v}}) + \bar{\mathbf{v}} - \bar{\mathbf{v}} \right)^2 = T^*\end{aligned}\quad (2.15)$$

This means that the temperature has been upgraded to T^* and, although the velocities have been changed, the total momentum is conserved because

$$M\bar{\mathbf{v}}^* = \sum_{i=1}^N m^i \mathbf{v}^{i*} = M\bar{\mathbf{v}} = \sum_{i=1}^N m^i \mathbf{v}^i \quad (2.16)$$

Since the positions of the atoms are kept unchanged, the total potential energy is unchanged. On the other hand, the kinetic energy has been changed from

$$E_{kinetic} = \frac{1}{2} \sum_{i=1}^N m^i \mathbf{v}^i \cdot \mathbf{v}^i \quad (2.17)$$

to

$$\begin{aligned}E_{kinetic}^* &= \frac{1}{2} \sum_{i=1}^N m^i \mathbf{v}^{i*} \cdot \mathbf{v}^{i*} \\ &= \frac{1}{2} \sum_{i=1}^N m^i \left(\sqrt{T^*/T} (\mathbf{v}^i - \bar{\mathbf{v}}) + \bar{\mathbf{v}} \right)^2 \\ &= \frac{T^*}{T} E_{kinetic} + \left(1 - \frac{T^*}{T}\right) \frac{1}{2} M\bar{\mathbf{v}} \cdot \bar{\mathbf{v}}\end{aligned}\quad (2.18)$$

2.2.2.2 Berendsen Thermostat

The Berendsen algorithm can be better understood by rewriting the governing equations as

$$\begin{aligned} \mathbf{v}^i(t + \frac{1}{2}\Delta t) &= \{\mathbf{v}^i(t - \frac{1}{2}\Delta t) + \Delta t[\mathbf{f}^i(t) + \boldsymbol{\phi}^i(t)] / m^i\} \chi(t) \\ \mathbf{v}^i(t) &= \{\mathbf{v}^i(t + \frac{1}{2}\Delta t) + \mathbf{v}^i(t - \frac{1}{2}\Delta t)\} / 2 \\ \chi(t) &= \sqrt{1 + \frac{\Delta t}{\tau} \left(\frac{T^*}{T} - 1\right)} \\ \mathbf{r}^i(t + \Delta t) &= \mathbf{r}^i(t) + \Delta t \mathbf{v}^i(t + \frac{1}{2}\Delta t) \end{aligned} \quad (2.19)$$

It is seen that if $T = T^* \rightarrow \chi = 1$, then Eq.(2.19) is essentially Eq.(2.1) in finite difference form.

2.2.2.3 Gaussian Constraints

In Gaussian Constraints algorithm, the governing equations are the same as Eq.(2.1).

However the idea behind it is quite different. Rewrite the temperature of N atoms as

$$T = \frac{1}{3k_B N} \sum_{i=1}^N (m^i \mathbf{v}^i)^2 / m^i \quad (2.20)$$

If the temperature reaches equilibrium, i.e., $T = T^*$, or it is considered to be true, then

$$\frac{dT}{dt} \sim \frac{d}{dt} \left(\sum_{i=1}^N (m^i \mathbf{v}^i)^2 \right) \sim \sum_{i=1}^N m^i \mathbf{v}^i \cdot [\mathbf{f}^i + \boldsymbol{\phi}^i] = 0 \quad (2.21)$$

Therefore χ is chosen to be

$$\chi(t) = \frac{\sum_{i=1}^N m^i \mathbf{v}^i \cdot (\mathbf{f}^i + \boldsymbol{\phi}^i)}{\sum_{i=1}^N (m^i \mathbf{v}^i)^2} \quad (2.22)$$

It is noticed that by writing the temperature as in Eq.(2.21) one implicitly assume the total momentum of this group of atoms is zero.

2.2.2.4 Nose-Hoover thermostat

In this algorithm, the governing equations, Eq.(2.1), are modified to

$$\begin{aligned} \dot{\mathbf{r}}^i &= \mathbf{v}^i \\ \dot{\mathbf{v}}^i &= (\mathbf{f}^i + \boldsymbol{\phi}^i) / m^i - \chi(t) \mathbf{v}^i \end{aligned} \quad (2.23)$$

and the so-called “friction coefficient”, χ , is a scalar-valued function controlled by the first order differential equation

$$\dot{\chi} = \frac{1}{T^* \tau^2} (T(t) - T^*) \quad (2.24)$$

where τ is a specified time constant, normally in the range 0.5~2 picoseconds.

Note: In using velocity upgrade or random number generation, one modifies the velocities once in a while without changing the governing equations. It is noticed that these governing equations are actually the Newton's second Law for those atoms. Modification of the velocities is essentially an action to implement the boundary condition, which reflects the interaction between the material body and its environment. On the contrary, in using Nose-Hoover thermostat, Berendsen thermostat, or Gaussian constraints, one has to modify the governing equations.

2.3 Objectivity Incorporated Molecular Dynamics

Since the first introduction of MD, most simulations have been performed in an inertial reference frame, which means the reference frame is at still or at a constant velocity. However, rare discussion has been given with respect to non-inertial reference frames, e.g. a reference frame that undergoes rotation or acceleration, which is more general and common in nature. It is essentially important to investigate into physical phenomena in the non-inertial reference frame, while features of the existing NEMD should be preserved. To achieve this goal, the simulation scheme needs to include additional physical laws to accommodate the change/motion of reference frames.

Principle of objectivity, which is a basic concept in continuum mechanics, plays an essential role in capturing the invariance of mechanics of materials under the change of reference frame. The simple idea of this notion is that material measurements made in different reference frames are required to be the objectively equivalent and are not subject to the motion of the observers. Following this principle, this research proposes the theory of Objectivity Incorporated Molecular Dynamics (OIMD) [68].

2.3.1 Groundwork of Objectivity

The concept of objectivity has been introduced in almost every continuum mechanics textbook. For example, in *Mechanics of Continua* [69] and *Microcontinuum Field Theories* [70,71], it is clear that the material properties do not depend on the reference frame selected. The measurements made by an observer, whether he/she is in motion or not, should be the same. With this viewpoint taken, the measurements made in one reference frame are sufficient to determine the material properties in all other frames which are in rigid motion with respect to one another. In the formulation of the response functions, it is desirable to employ quantities that are not dependent on the motions of the observer. Such quantities are called objective or material frame-indifferent. For example, the velocity of an automobile will appear different to two observers, one stands on the roadside and the other rides in the car. Therefore, the velocity vector is not objective. Similarly, the acceleration is not an objective vector. The distance between two points and angles between two

directions are independent of the rigid motions of the reference frame (the observer). Hence, they are objective quantities.

Definition 1. Two motions $x_k(\mathbf{X}, t)$ and $x_k^*(\mathbf{X}, t^*)$ are called objectively equivalent if and only if

$$x_k^*(\mathbf{X}, t^*) = Q_{kl}(t)x_l(\mathbf{X}, t) + b_k(t), \quad t^* = t - a \quad (2.25)$$

Or in matrix notation,

$$\mathbf{x}^*(\mathbf{X}, t^*) = \mathbf{Q}(t)\mathbf{x}(\mathbf{X}, t) + \mathbf{b}(t) \quad (2.26)$$

where a is a constant time shift, $\mathbf{b}(t)$ is a time-dependent translation, and $\mathbf{Q}(t)$ is time-dependent orthogonal transformations, i.e.

$$Q_{kl}Q_{ml} = Q_{lk}Q_{lm} = \delta_{km}, \quad \det(\mathbf{Q}) = +1 \quad (2.27)$$

It is seen that Q_{kl} consists of all rigid rotations ($\det \mathbf{Q} = +1$). Two objectively equivalent motions differ only in relative frame and time.

Definition 2 (Objectivity). Any tensorial quantity that obeys the tensor transformation law under Eq.(2.25) is said to be objective or material frame-indifferent.

For example, a vector a_k and a tensor t_{kl} are objective if they obey the transformation laws.

$$\begin{aligned} a_k^*(\mathbf{X}, t^*) &= Q_{kl}(t) a_l(\mathbf{X}, t) \\ t_{kl}^*(\mathbf{X}, t^*) &= Q_{km}(t) Q_{ln}(t) t_{mn}(\mathbf{X}, t) \end{aligned} \quad (2.28)$$

2.3.2 Objectivity Incorporated Molecular Dynamics

In Objectivity Incorporated Molecular Dynamics (OIMD), the equations of motion are

$$m^i (\dot{\mathbf{v}}^i - \dot{\mathbf{i}}^i) = \mathbf{f}^i \quad \text{or} \quad m^i \dot{\mathbf{v}}^i = \mathbf{f}^i + m^i \dot{\mathbf{i}}^i \quad (2.29)$$

$$\begin{aligned} \mathbf{f}^i &= \Phi_0^i(\mathbf{r}^i) + \Phi_1^i(\tilde{\mathbf{v}}^i) + \Phi_2^i(\tilde{T}) + \Phi_3^i(\tilde{\mathbf{p}}) + \dots \\ &= -\frac{\partial V}{\partial \mathbf{r}^i} + \Phi_1^i(\tilde{\mathbf{v}}^i) + \Phi_2^i(\tilde{T}) + \Phi_3^i(\tilde{\mathbf{p}}) + \dots \end{aligned} \quad (2.30)$$

where Eq.(2.29) and Eq.(2.30) may be regarded as the governing equation and the constitutive equations, respectively; m^i , \mathbf{r}^i , \mathbf{v}^i are the mass, position and velocity of the i^{th} atom, respectively. The fictitious force $m^i \dot{\mathbf{i}}^i$, which accounts for the motion of the reference frame itself, can be calculated as

$$\dot{\mathbf{i}}^i = -2\boldsymbol{\omega} \times (\mathbf{v}^i - \dot{\mathbf{b}}) - \boldsymbol{\omega} \times (\boldsymbol{\omega} \times (\mathbf{r}^i - \mathbf{b})) - \dot{\boldsymbol{\omega}} \times (\mathbf{r}^i - \mathbf{b}) + \ddot{\mathbf{b}} \quad (2.31)$$

where $\boldsymbol{\omega}$ and $\dot{\mathbf{b}}$ are the angular velocity and translational velocity of the reference frame in simulation, which are non-vanishing in non-inertial reference frame.

The driving force \mathbf{f}^i of the i^{th} atom is a linear combination of various types of body forces

$\{\Phi_0, \Phi_1, \Phi_2, \Phi_3, \dots\}$; $\Phi_0^i(\mathbf{r}^i) = -\frac{\partial V}{\partial \mathbf{r}^i}$ is the interatomic force, where V is the interatomic potential of the system; $\Phi_1^i(\tilde{\mathbf{v}}^i)$ is the damping force, $\Phi_2^i(\tilde{T})$ is the temperature force; and $\Phi_3^i(\tilde{p})$ is the pressure force. Moreover, OIMD requires that each term of the body force must be objective, i.e. it obeys the transformation law as in Eq.(2.25). To satisfy this requirement, the objective velocity $\tilde{\mathbf{v}}$, may also be called thermal velocity or disturbance velocity [72,73] is defined as:

$$\tilde{\mathbf{v}}^i \equiv \mathbf{v}^i - \bar{\mathbf{v}} - \boldsymbol{\eta}^i \quad (2.32)$$

where $\bar{\mathbf{v}}$ and $\boldsymbol{\eta}^i$ can be found by the following procedure

$$M \equiv \sum_{i=1}^N m^i, \quad \bar{\mathbf{r}} \equiv \left(\sum_{i=1}^N m^i \mathbf{r}^i \right) / M, \quad \bar{\mathbf{v}} \equiv \left(\sum_{i=1}^N m^i \mathbf{v}^i \right) / M \quad (2.33)$$

$$\hat{\mathbf{r}}^i \equiv \mathbf{r}^i - \bar{\mathbf{r}}, \quad \hat{\mathbf{v}}^i \equiv \mathbf{v}^i - \bar{\mathbf{v}} \quad (2.34)$$

$$\mathbf{L} = \sum_{i=1}^N m^i \hat{\mathbf{r}}^i \times \hat{\mathbf{v}}^i, \quad \mathbf{J} = \sum_{i=1}^N m^i \left[(\hat{\mathbf{r}}^i \hat{\mathbf{r}}^i) \mathbf{I} - \hat{\mathbf{r}}^i \otimes \hat{\mathbf{r}}^i \right] \quad (2.35)$$

$$\boldsymbol{\eta}^i = (\mathbf{J}^{-1} \cdot \mathbf{L}) \times \hat{\mathbf{r}}^i \equiv \boldsymbol{\omega} \times \hat{\mathbf{r}}^i \quad (2.36)$$

It is proved that the thermal velocity $\tilde{\mathbf{v}}$ satisfies the tensor transformation law (c.f. APPENDIX-I):

$$\tilde{\mathbf{v}}^* = \mathbf{Q}\tilde{\mathbf{v}} \quad (2.37)$$

Therefore, the objective temperature \tilde{T} can be defined as:

$$\tilde{T} = \frac{1}{N^{dof} k_B} \sum_{i \in \Omega} m^i \tilde{\mathbf{v}}^i \cdot \tilde{\mathbf{v}}^i \quad (2.38)$$

The objective virial stress $\tilde{\boldsymbol{\sigma}}$ can be defined as:

$$\tilde{\boldsymbol{\sigma}} = \frac{1}{\Omega} \sum_{i \in \Omega} \left(-m^i \tilde{\mathbf{v}}^i \otimes \tilde{\mathbf{v}}^i - \frac{1}{2} \sum_{j \neq i}^N \mathbf{r}^{ij} \otimes \mathbf{f}^{ij} \right) \quad (2.39)$$

The objective pressure \tilde{p} can be defined as:

$$\begin{aligned} \tilde{P} &= \frac{1}{3\Omega} \left(\sum_{i \in \Omega} m^i \tilde{\mathbf{v}}^i \cdot \tilde{\mathbf{v}}^i + \frac{1}{2} \sum_{i \in \Omega} \sum_{j \neq i}^N \mathbf{r}^{ij} \cdot \mathbf{f}^{ij} \right) \\ &= \frac{N^{dof} k_B \tilde{T}}{3\Omega} + \frac{1}{6\Omega} \sum_{i \in \Omega} \sum_{j \neq i}^N \mathbf{r}^{ij} \cdot \mathbf{f}^{ij} \end{aligned} \quad (2.40)$$

Here \mathbf{I} is the identity matrix; Ω is the volume of the region of interest; $N^{dof} = 3N^\Omega - 6$ is the number of degree of freedom; N^Ω is the number of atoms in Ω ; N is the number of atoms within the cutoff of Ω ; k_B is the Boltzmann constant.

Following the requirement of principle of objectivity and using the definitions as in Eq.(2.32), Eq. (2.38), Eq.(2.39), and Eq.(2.40), all body forces $\{\Phi_0, \Phi_1, \Phi_2, \Phi_3, \dots\}$ in the constitutive equations are now objective:

$$\Phi_s^* = \mathbf{Q}\Phi_s, \quad s = 0,1,2,\dots \quad (2.41)$$

It is proved that in the governing equation, the difference between the apparent acceleration and the fictitious force-induced acceleration is objective (c.f. APPENDIX - II).

$$(\mathbf{a}^* - \mathbf{i}^*) = \mathbf{Q}(\mathbf{a} - \mathbf{i}) \quad (2.42)$$

By design, both the constitutive equation and governing equation satisfy the principle of objectivity, i.e. they are form-invariant under change of reference frame. Therefore, this set of equations of motion is valid for all situations within the scope of Newtonian mechanics. OIMD is capable of simulating motions of atoms objectively no matter what reference frame is used in the simulation.

2.4 Molecular Dynamics in Electromagnetic Field

2.4.1 Governing Equation

The governing equation of non-equilibrium molecular dynamics (NEMD) simulations in electromagnetic field can be expressed as

$$m^i \dot{\mathbf{v}}^i = \mathbf{f}^i + q^i (\mathbf{E}^{\text{ext}} + \mathbf{v}^i \times \mathbf{B}^{\text{ext}} / c) \quad i \in [1, 2, 3, \dots, N] \quad (2.43)$$

Where m^i , q^i , \mathbf{r}^i , and \mathbf{v}^i represent the mass, electric charge, position, and velocity of the i^{th} atom respectively. \mathbf{f}^i represents the body forces acting on atom i and N is the total number of atoms within the system. c represents the speed of the light whereas \mathbf{E}^{ext} and \mathbf{B}^{ext} represent the external electric and magnetic fields respectively.

2.4.2 Maxwell Equation at Atomic Scale

The third term on the right-hand side of Eq.(2.43) is the Lorentz force acting on a charged particle and is modeled using Maxwell's equation. In a vacuum, The Maxwell's equations are expressed as:

$$\begin{aligned} \nabla \cdot \mathbf{E} &= 0 \\ \nabla \cdot \mathbf{B} &= 0 \\ \nabla \times \mathbf{E} + \frac{1}{c} \frac{\partial \mathbf{B}}{\partial t} &= 0 \\ \nabla \times \mathbf{B} - \frac{1}{c} \frac{\partial \mathbf{E}}{\partial t} &= 0 \end{aligned} \quad (2.44)$$

Since the goal is to simulate the environmental effects on a material system, the external electromagnetic (EM) field is considered as part of the environment. It is noticed that in vacuum (the situation in air is very close to that in vacuum), there is no free charge, no current, and no distinction between \mathbf{E} and \mathbf{D} and between \mathbf{B} and \mathbf{H} .

In a simulation, one of the following three situations can be chosen:

1) There is no external EM field: $\mathbf{E}^{\text{ext}} = \mathbf{B}^{\text{ext}} = 0$

2) External EM field is constant in space and in time: $\mathbf{E}^{\text{ext}} = \mathbf{c}^1$ and $\mathbf{B}^{\text{ext}} = \mathbf{c}^2$

3) External EM field is specified as function of space and time: $\mathbf{E}^{\text{ext}} = \mathbf{E}(\mathbf{x},t)$ and $\mathbf{B}^{\text{ext}} = \mathbf{B}(\mathbf{x},t)$

However, it is emphasized that when the EM field is set up in the simulation, it has to satisfy the Maxwell's equations, otherwise the simulation result is not physical and cannot be validated by experiments.

2.4.3 Induced Electromagnetic Quantities

In the MD simulation with EM feature, one may calculate the induced EM quantities, such as polarization of a unit cell \mathbf{p} , voltage ϕ , electric field \mathbf{e} , and magnetic field \mathbf{b} as follows:

$$\mathbf{p} = \frac{1}{V_{\text{cell}}} \sum_{\alpha=1}^{N_a} q^{\alpha} \mathbf{r}^{\alpha} \quad (2.45)$$

$$\phi = \sum_{i=1}^N \frac{q^i}{|\mathbf{x} - \mathbf{r}^i|} \quad (2.46)$$

$$\mathbf{e} = -\sum_{i=1}^N q^i \nabla \left(\frac{1}{|\mathbf{x} - \mathbf{r}^i|} \right) \quad (2.47)$$

$$\mathbf{b} = c^{-1} \sum_{i=1}^N q^i \nabla \times \left(\frac{\dot{\mathbf{r}}^i}{|\mathbf{x} - \mathbf{r}^i|} \right) \quad (2.48)$$

Where, N_a is the number of atoms in a unit cell. It is noted that the above mentioned formulation is based on the non-relativistic assumption [74].

2.5 Numerical Procedure for MD Simulations

2.5.1 Simple Procedure of Classical MD

A number of important features of MD simulations can be illustrated through a simple program. The program is constructed as following:

- 1) Read in the parameters that specify the conditions of the run (e.g., initial temperature, number of particles, density, time step).
- 2) Initialize the system (i.e., select initial positions and velocities).
- 3) Compute the forces on all particles.

4) Integrate Newton's equation of motion. This step and the previous one make up the core of the simulation. They are repeated until the time evolution of the system has been computed for the desired length of time.

5) After completion of the central loop, compute and print the average ages of measured quantities, and stop.

To start the simulation, initial positions and velocities are assigned to all particles in the system. The particle positions should be chosen compatible with the structure. In any event, the particles should not be positioned at position that results in an appreciable overlap of the atomic or molecular cores. Often this is achieved by initially placing the particle on a cubic lattice.

What comes next is the most time-consuming part of almost all MD simulations: the calculation of the force acting on every particle. For example, for a model system with pairwise additive interaction, one has to consider the contribution to the force on particle i due to all its neighbors. For a system of N particles, it is needed to evaluate $N \times (N - 1) / 2$ pair distances. This implies that, if there are no tricks, the time needed for evaluation of the force scales as N^2 . There exists certain efficient techniques to speed up the evaluation of both short-range and long-range forces in such a way that the computing time scales as N , rather than N^2 .

Now that all forces between the particles have been computed, Newton's equations of motion are ready to be integrated. Algorithms such as Verlet algorithm [28-31] have been designed to do this.

2.5.2 Velocity Verlet Method

Velocity Verlet integration is a numerical method used to integrate Newton's equations of motion. The Velocity Verlet integrator provides a good numerical stability, as well as other important properties such as time-reversibility, at no significant additional computational cost over the simple Euler method [29]. The standard implementation scheme of this algorithm is

- 1) Calculate a half step velocity: $\mathbf{v}(t + \frac{1}{2}\Delta t) = \mathbf{v}(t) + \frac{1}{2}\mathbf{a}(t)\Delta t$.
- 2) Calculate the full timestep position: $\mathbf{r}(t + \Delta t) = \mathbf{r}(t) + \mathbf{v}(t + \frac{1}{2}\Delta t)\Delta t$.
- 3) Use the new positions to obtain the updated force $\mathbf{f}(t + \Delta t)$ and hence the acceleration $\mathbf{a}(t + \Delta t)$.
- 4) Calculate the full timestep velocity: $\mathbf{v}(t + \Delta t) = \mathbf{v}(t + \frac{1}{2}\Delta t) + \frac{1}{2}\mathbf{a}(t + \Delta t)\Delta t$

These steps update the information from $\mathbf{a}(t)$, $\mathbf{v}(t)$, and $\mathbf{r}(t)$ to $\mathbf{a}(t + \Delta t)$, $\mathbf{v}(t + \Delta t)$, and $\mathbf{r}(t + \Delta t)$, so the time marching can move forward.

2.5.3 Heun's Method

The scheme of the Velocity Verlet algorithm can be summarized as:

$$\begin{aligned}
 (1) \quad \mathbf{v}^{n+\frac{1}{2}} &= \mathbf{v}^n + \frac{1}{2} \mathbf{A}^n \Delta t \\
 (2) \quad \mathbf{x}^{n+1} &= \mathbf{x}^n + \mathbf{v}^{n+\frac{1}{2}} \Delta t \\
 (3) \quad \mathbf{a}^{n+1} &= \mathbf{A}(\mathbf{x}^{n+1}) = \mathbf{A}^{n+1} \\
 (4) \quad \mathbf{v}^{n+1} &= \mathbf{v}^{n+\frac{1}{2}} + \frac{1}{2} \mathbf{A}^{n+1} \Delta t
 \end{aligned} \tag{2.49}$$

It is noted that in this scheme, it is assumed that acceleration \mathbf{a}^{n+1} can be determined by atomic position \mathbf{x}^{n+1} only, as in step (3) of Eq.(2.49). However, sometimes acceleration \mathbf{a}^{n+1} can also depend on the simultaneous velocity \mathbf{v}^{n+1} , e.g. when damping force, Lorentz force, or fictitious force is present, this scheme may fail to precisely predict the trajectory of the atoms. Therefore, for numerical accuracy purpose, other integration methods may be needed, such as Heun's method [75]. Heun's method involves a two-stage calculation of acceleration. The implementation scheme consists of the following steps:

$$\begin{aligned}
(1) \quad \mathbf{a}^n &= \mathbf{A}(\mathbf{x}^n, \mathbf{v}^n, t^n) = \mathbf{A}^n \\
(2) \quad \mathbf{v}^* &= \mathbf{v}^n + \Delta t \mathbf{A}^n, \\
\mathbf{x}^{n+1} &= \mathbf{x}^* = \mathbf{x}^n + \Delta t \mathbf{v}^n + \frac{1}{2} \Delta t^2 \mathbf{A}^n, \\
t^{n+1} &= t^* = t^n + \Delta t \\
(3) \quad \mathbf{a}^* &= \mathbf{A}(\mathbf{x}^*, \mathbf{v}^*, t^*) = \mathbf{A}^* \\
(4) \quad \mathbf{v}^{n+1} &= \mathbf{v}^n + \frac{1}{2} \Delta t (\mathbf{A}^n + \mathbf{A}^*) \\
(5) \quad \mathbf{a}^{n+1} &= \mathbf{A}(\mathbf{x}^{n+1}, \mathbf{v}^{n+1}, t^{n+1}) = \mathbf{A}^{n+1}
\end{aligned} \tag{2.50}$$

It is seen that step (5) of Eq.(2.50) is identically step (1), so within one full timestep there are twice calculation of force, which is the most time consuming part in MD computation. Despite the computational cost, this procedure will provide more reliable numerical results.

2.5.4 Inverse Method for MD in EM Field

The governing equation of MD in EM field is:

$$m\dot{\mathbf{v}} = \mathbf{f} + q(\mathbf{E} + \mathbf{v} \times \mathbf{B} / c) \tag{2.51}$$

It is clear that in the presence of a magnetic field which acts on charged particles, the instantaneous acceleration/force of an atom depend on its instantaneous velocity. It seems that the Velocity Verlet scheme as shown in Eq. (2.49) fails to calculate \mathbf{a}^{n+1} . However, since the cross product $\mathbf{v} \times \mathbf{B}$ mixes \mathbf{v} and \mathbf{B} in a linear way, the integration scheme can be rewritten to solve \mathbf{v}^{n+1} explicitly. The following is the derived scheme:

$$\begin{aligned}
(1) \quad \mathbf{v}^{n+\frac{1}{2}} &= \mathbf{v}^n + \frac{1}{2} \mathbf{a}^n \Delta t \\
(2) \quad \mathbf{x}^{n+1} &= \mathbf{x}^n + \mathbf{v}^{n+\frac{1}{2}} \Delta t \\
(3) \quad \hat{\mathbf{f}}^{n+1} &= \hat{\mathbf{f}}(\mathbf{x}^{n+1}) = -\frac{\partial V}{\partial \mathbf{x}^{n+1}} \\
(4) \quad \mathbf{v}^{n+1} &= \left[\tilde{\mathbf{I}} + \frac{q\Delta t}{2mc} \tilde{\mathbf{W}} \right]^{-1} \cdot \left[\mathbf{v}^{n+\frac{1}{2}} + \frac{\Delta t}{2m} (\hat{\mathbf{f}}^{n+1} + q\mathbf{E}) \right] \\
(5) \quad \mathbf{f}^{n+1} &= \hat{\mathbf{f}}^{n+1} + \frac{q\mathbf{E}}{m} - \frac{q}{mc} \mathbf{B} \times \mathbf{v}^{n+1} \\
(6) \quad \mathbf{a}^{n+1} &= \mathbf{f}^{n+1} / m
\end{aligned} \tag{2.52}$$

where $\tilde{\mathbf{I}}$ is the identity matrix, $\tilde{\mathbf{W}}$ is an antisymmetric matrix such that $\mathbf{B} \times () = \tilde{\mathbf{W}}()$

In particular, $\tilde{\mathbf{W}}$ can be constructed as:

$$\tilde{\mathbf{W}} = \begin{bmatrix} 0 & -B_3 & B_2 \\ B_3 & 0 & -B_1 \\ -B_2 & B_1 & 0 \end{bmatrix} \tag{2.53}$$

This scheme is a modification to the integration scheme of Velocity Verlet method, when the velocity \mathbf{v}^{n+1} is required in the calculation of \mathbf{a}^{n+1} . Since the calculation of

$\left[\tilde{\mathbf{I}} + \frac{q\Delta t}{2mc} \tilde{\mathbf{W}} \right]^{-1}$ involves the inverse of a matrix, this method may be called *Inverse*

Method. Inverse Method has an advantage over original Velocity Verlet method because it is more accurate, and an advantage over Heun's method because it is faster.

2.6 Summary

Molecular dynamics simulation is ideally suited for the study of nanopolycrystalline materials. In this chapter, the basic idea and theory of classical MD and NEMD simulations are introduced. In addition to the existing method, the theory of Objectivity Incorporated Molecular Dynamics (OIMD) is proposed to extend the credibility and capability in simulating material systems in arbitrary reference frame or local systems with arbitrary motions. It is worthwhile to note that the concept of objectivity in OIMD is Euclidean objectivity, which is associated with the domain of classical mechanics. In contrast, when electromagnetic field is present, the motions of atoms are no longer only governed by classical mechanics. Therefore, simulating MD in EM field is not required to satisfy the principle of objectivity. Once equations of motions are obtained, numerical integration methods are employed to calculate the dynamic process of the atomistic system. While the original Velocity Verlet method can only handle position-based force calculation, Heun's method and Inverse Method are introduced in this research to calculate both position- and velocity- based force calculation. These integrators can be selected to use in MD simulations to accommodate different needs.

CHAPTER 3: MOLECULAR MECHANICS FORCE FIELDS

To study nanostructures composed of several hundred to several billion atoms or molecules, the most computationally efficient approach is the use of phenomenological interatomic potential, since the existing quantum mechanical techniques are able to deal with at most a few hundred atoms. The interatomic potential gives the starting point for the majority of simulation techniques, i.e., the calculation of energy. These phenomenological potentials are obtained by selecting a mathematical function and fitting its unknown parameters to various experimentally determined properties of the systems, such as lattice constant, energies, forces, stresses, phonons, dielectric constants and so on.

This chapter first reviews the most widely used interatomic potentials in current atomistic simulation studies. In particular, Coulomb potential for charged particles, the Buckingham potential for short range interaction, and the Lennard-Jones potential, are some of the most useful interatomic potentials in nanopolycrystalline materials simulation. Then, an efficient treatment of the calculation of Coulomb potential is addressed. To enable simulations of complex material system that consists of various kinds of crystals, this research established a database to contain interatomic potentials and their parameters. Further the combination rule for using different potential parameters of Buckingham potential is revisited and validated.

3.1 Empirical Interatomic Potentials

The most general form of potential energy in MD simulation can be expressed by:

$$V(\mathbf{r}^i, \mathbf{r}^j, \dots, \mathbf{r}^n) = \sum_{i=1}^n V^{(1)}(\mathbf{r}^i) + \frac{1}{2!} \sum_{i,j=1}^n V^{(2)}(\mathbf{r}^i, \mathbf{r}^j) + \frac{1}{3!} \sum_{i,j,k=1}^n V^{(3)}(\mathbf{r}^i, \mathbf{r}^j, \mathbf{r}^k) + \dots \quad (3.1)$$

where \mathbf{r}^n is the position vector of the n -th atom, and the function $V^{(m)}$ is called the m -body potential. The first term of equation represents the energy due to an external force field or boundary conditions, such as gravitational or electrostatic, into which the system is immersed; the second term shows pairwise interaction of the particles, the interaction of any pair of atoms depends only on their spacing and is not affected by the presence of a third atom; the third term gives the three-body potentials, etc. In theory, the m in $V^{(m)}$ can be as large as possible, but the computational expense will increase exponentially.

3.1.1 Coulomb Interaction

When considering ionic materials, such potentials usually comprise a Coulomb term for the long-range interactions along with a term to describe the short-range interactions. The Coulomb interaction is by far the dominant term, and it can represent up to 90% of the total energy. It is given by Coulomb's law

$$V(r_{ij}) = \frac{q_i q_j}{r_{ij}} \quad (3.2)$$

where $r_{ij} = |\mathbf{r}_i - \mathbf{r}_j|$ is the distance between atom i and atom j ; q_i and q_j are the charge of the i -th atom and the j -th atom.

One issue associated with the Coulomb term concerns the charges of ions. In most simulations, the charges of ions are fixed (i.e. independent of geometry) for simplicity, and their magnitude is determined by one of two methods: (i) fitted parametrically along with other interatomic potential parameters, and (ii) extracted from quantum mechanical information. In the later method, the choice would be to employ the Born effective charges that describe the response of the ions to an electric field.

3.1.1.1 Computational Methods for Coulomb Interaction

Coulomb interaction is computationally demanding because of the long-range r^{-1} decay, a variety of techniques have been developed to address the proper and practical handling of electrostatic interactions. For a specimen of finite size, the Coulomb potential and force can be calculated directly. For infinite 3-D periodic systems, the most widely employed approach is the Ewald method [76,77,28,31]. In Ewald summation method, to accelerate the evaluation, the Coulomb term is subjected to a Laplace transformation and then separated into two components, one of which is rapidly convergent in real space and a second which decays quickly in reciprocal space. Conceptually, this approach can be viewed as adding and subtracting a Gaussian charge distribution centered about each ion.

Recently, Wolf et al [78] devised a new method for Coulombic interactions, which may be referred as a *damped shifted force* model. Here the formulation and a simple routine for parameter selection is shown.

For Coulomb potential between i -th atom and j -th atom, instead of

$$V^{ij}(r) = \frac{q^i q^j}{r} \quad , \quad \mathbf{r}^{ij} \equiv \mathbf{r}^i - \mathbf{r}^j \quad , \quad r \equiv \|\mathbf{r}^i - \mathbf{r}^j\| \quad (3.3)$$

Wolf et al proposed the following formula

$$V^{ij}(r) = \frac{q^i q^j}{r} \operatorname{erfc}(\alpha r) + q^i q^j r \left\{ \frac{\operatorname{erfc}(\alpha R)}{R^2} + \frac{2\alpha \exp(-\alpha^2 R^2)}{\sqrt{\pi} R} \right\} + C \quad (3.4)$$

where α is a constant; R is a cutoff; and

$$C = -2q^i q^j \left\{ \frac{\operatorname{erfc}(\alpha R)}{R} + \frac{\alpha}{\sqrt{\pi}} \exp(-\alpha^2 R^2) \right\} \quad (3.5)$$

$$\begin{aligned} \operatorname{erfc}(\alpha r) &= 1 - \operatorname{erf}(\alpha r) \\ &= 1 - \frac{2}{\sqrt{\pi}} \int_0^{\alpha r} \exp(-\xi^2) d\xi \end{aligned} \quad (3.6)$$

It is seen that

$$\frac{d[\operatorname{erfc}(\alpha r)]}{dr} = -\frac{2\alpha}{\sqrt{\pi}} \exp(-\alpha^2 r^2) \quad (3.7)$$

Now it is straightforward to obtain

$$\begin{aligned}
V^{ij}(R) &= \frac{q^i q^j}{R} \operatorname{erfc}(\alpha R) + q^i q^j \left\{ \frac{\operatorname{erfc}(\alpha R)}{R} + \frac{2\alpha}{\sqrt{\pi}} \exp(-\alpha^2 R^2) \right\} + C \\
&= q^i q^j \left\{ \frac{2}{R} \operatorname{erfc}(\alpha R) + \frac{2\alpha}{\sqrt{\pi}} \exp(-\alpha^2 R^2) \right\} + C \\
&= 0
\end{aligned} \tag{3.8}$$

$$\begin{aligned}
\frac{dV^{ij}}{dr} &= -\frac{q^i q^j}{r^2} \operatorname{erfc}(\alpha r) - \frac{q^i q^j}{r} \frac{2\alpha}{\sqrt{\pi}} \exp(-\alpha^2 r^2) \\
&\quad + q^i q^j \left\{ \frac{\operatorname{erfc}(\alpha R)}{R^2} + \frac{2\alpha}{\sqrt{\pi}} \frac{\exp(-\alpha^2 R^2)}{R} \right\}
\end{aligned} \tag{3.9}$$

$$\left. \frac{dV^{ij}}{dr} \right|_{r=R} = 0 \tag{3.10}$$

It is noticed that the interatomic force and the stiffness can be derived as follows:

$$\mathbf{f}^i = -\mathbf{f}^j = -\frac{\partial V}{\partial \mathbf{r}^i} = -\frac{1}{r} \frac{dV}{dr} \mathbf{r}^{ij} \equiv -K \mathbf{r}^{ij} \tag{3.11}$$

$$\begin{aligned}
\mathbf{s}^{ii} &\equiv -\frac{\partial \mathbf{f}^i}{\partial \mathbf{r}^i} = \mathbf{s}^{jj} = -\mathbf{s}^{jj} = -\mathbf{s}^{jj} = \frac{\partial}{\partial \mathbf{r}^i} \left\{ \frac{1}{r} \frac{dV^{ij}}{dr} \mathbf{r}^{ij} \right\} \\
&= \frac{1}{r} \frac{d}{dr} \left\{ \frac{1}{r} \frac{dV^{ij}}{dr} \right\} \mathbf{r}^{ij} \otimes \mathbf{r}^{ij} + \frac{1}{r} \frac{dV^{ij}}{dr} \mathbf{I} \\
&\equiv H \mathbf{r}^{ij} \otimes \mathbf{r}^{ij} + K \mathbf{I}
\end{aligned} \tag{3.12}$$

Define

$$\begin{aligned}
W_1 &\equiv \frac{2\alpha}{\sqrt{\pi}} e^{-\alpha^2 R^2} \\
W_2 &\equiv \frac{2\alpha}{\sqrt{\pi}} \frac{e^{-\alpha^2 R^2}}{R} \\
W_3 &\equiv \frac{\operatorname{erfc}(\alpha R)}{R} \\
W_4 &\equiv \frac{\operatorname{erfc}(\alpha R)}{R^2}
\end{aligned} \tag{3.13}$$

It is straightforward to obtain

$$V^{ij} = q^i q^j \left\{ \frac{\operatorname{erfc}(\alpha r)}{r} + r[W_2 + W_4] - W_1 - 2W_3 \right\} \tag{3.14}$$

$$\frac{dV^{ij}}{dr} = q^i q^j \left\{ -\frac{\operatorname{erfc}(\alpha r)}{r^2} - \frac{2\alpha}{\sqrt{\pi}} \frac{e^{-\alpha^2 r^2}}{r} + W_2 + W_4 \right\} \tag{3.15}$$

$$K \equiv \frac{1}{r} \frac{dV^{ij}}{dr} = q^i q^j \left\{ -\frac{\operatorname{erfc}(\alpha r)}{r^3} - \frac{2\alpha}{\sqrt{\pi}} \frac{e^{-\alpha^2 r^2}}{r^2} + \frac{1}{r} [W_2 + W_4] \right\} \tag{3.16}$$

$$\frac{dK}{dr} = q^i q^j \left\{ 3 \frac{\operatorname{erfc}(\alpha r)}{r^4} + \frac{2\alpha}{\sqrt{\pi}} e^{-\alpha^2 r^2} \left[\frac{3}{r^3} + \frac{2\alpha^2}{r} \right] - \frac{1}{r^2} [W_2 + W_4] \right\} \tag{3.17}$$

$$H \equiv \frac{1}{r} \frac{dK}{dr} = q^i q^j \left\{ 3 \frac{\operatorname{erfc}(\alpha r)}{r^5} + \frac{2\alpha}{\sqrt{\pi}} e^{-\alpha^2 r^2} \left[\frac{3}{r^4} + \frac{2\alpha^2}{r^2} \right] - \frac{1}{r^3} [W_2 + W_4] \right\} \tag{3.18}$$

There are two parameters in Wolf's formula: α and R , where α accounts for damping and R accounts for cutoff radius. To determine a proper range of these two parameters so

that they can work effectively and efficiently, it is useful to look at their physical meanings. That is, α needs to be small enough to keep the accumulated potential (and force) close to the original Coulomb interaction, and R needs to be big enough to accommodate the convergence condition that imposed by α while small enough to reduce the computational cost, respectively.

The evaluation of the potential energy of an MgO specimen demonstrates the roles of α and R in Wolf's representation of Coulomb interaction.

Figure 3-1 essentially shows that if the value of α is given, the potential energy will converge as the cutoff radius goes big. The "knee" point of the curve tells that the corresponding value of R is sufficiently large for convergence purpose such that a bigger value is unnecessary. Different values of α (different curves in the figure) will result in different values of R for the "knee" point. Therefore, α and R are correlated, and R can be properly determined once α is set.

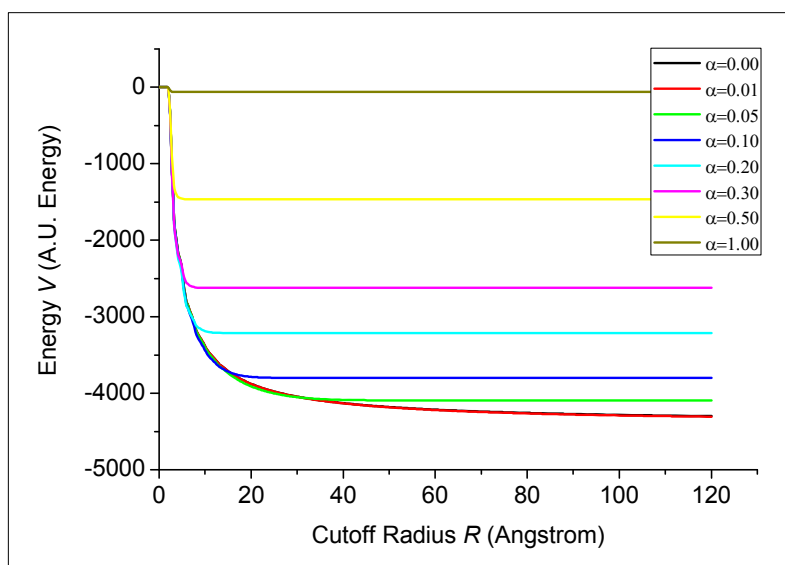


Figure 3-1: Potential energy vs. R (cutoff). Different lines represent different values of α (R in units of \AA , and α in units of \AA^{-1})

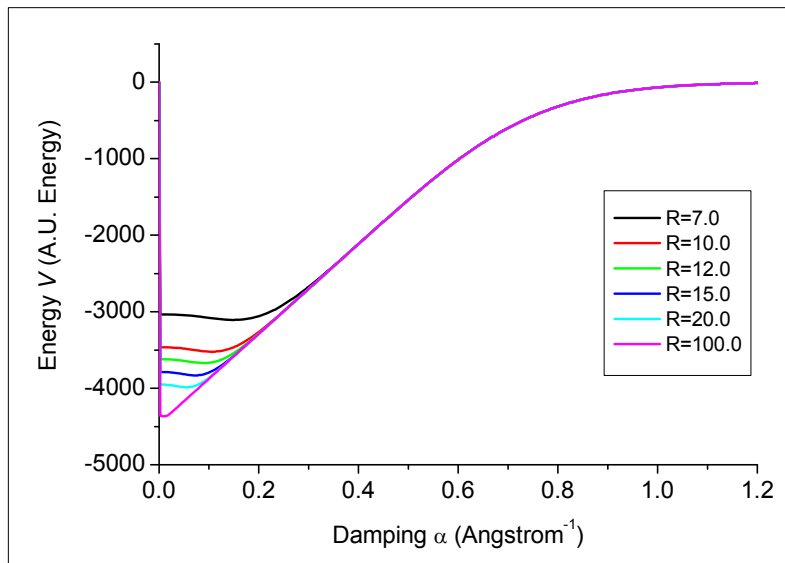


Figure 3-2: Potential energy vs. α (damping). Different lines represent different values of R (R in units of \AA , and α in units of \AA^{-1})

Figure 3-2 takes α as the horizontal axis and a set of R is evaluated, thus several curves are obtained. The left portions of the curves show that the bigger the cutoff radius R the lower potential energy the system will reach. The extreme case is that when $R \rightarrow \infty$ and $\alpha \rightarrow \infty$ the potential energy reaches the lowest value, which is the exact value of the electrostatic potential in the shifted force model. The right portions of the curves show that all curves come together like "one strand" and the energy level is high, which indicates that the highly damped system is non-physical. Therefore, a proper value of α should be

selected near the left side. Also note that there is also a "knee" point for each curve where it joins the "one strand". To the right of the "knee" point, the increasing of cutoff R will do no change of potential energy, which is similar to the result from Figure 3-1. An example "knee" point may be $\alpha = 0.3100 \text{ \AA}^{-1}$ with $R = 7.0 \text{ \AA}$.

From the results by Figure 3-1 and Figure 3-2, the correlation between α and R are known. Now the parameter selection routine can be established as following:

- 1) manually and empirically determine the value of R so that the estimated computational cost of the simulation program is acceptable with the computer resource.

- 2) with the R value obtained above, use the study as in Figure 3-2, and find the "knee" point. The value of α is thus determined.

- 3) with the α value obtained above, use the study as in Figure 3-1 to justify that the cutoff R satisfies the convergence requirement.

With this routine, the parameters for MgO material system is found that $\alpha = 0.18 \text{ \AA}^{-1}$ and $R = 12.0 \text{ \AA}$.

3.1.2 Two-Body Potentials

Two-body potentials are very common in interatomic potentials. They represent the interaction between two atoms when they are bonded, or two ions when they are in the immediate coordination shells. For the ionic case, a repulsive potential is usually adequate, with the most common choices being either a positive term which varies inversely with distance, or an exponential form. These lead to the Lennard-Jones [79] and Buckingham [80] potentials, respectively, when combined with the attractive r^{-6} term.

1) Lennard-Jones potential:

$$V(r_{ij}) = 4\varepsilon \left[\left(\frac{\sigma}{r_{ij}} \right)^{12} - \left(\frac{\sigma}{r_{ij}} \right)^6 \right] \quad (3.19)$$

2) Coulomb-Buckingham potential:

$$V(r_{ij}) = \frac{q_i q_j}{r_{ij}} + A_{ij} \exp\left(-\frac{r_{ij}}{\rho_{ij}}\right) - \frac{C_{ij}}{r_{ij}^6} \quad (3.20)$$

where ε is the depth of the potential well, σ is the distance at which the interatomic potential is zero, r_{ij} is the distance between the i -th atom and j -th atom, q_i and q_j are the charges of the i -th and j -th atom, A_{ij} , ρ_{ij} , and C_{ij} are all potential parameters of the pair of the i -th and j -th atom.

The Buckingham potential is easier to justify from a theoretical perspective since the repulsion between overlapping electron densities. Due to the Pauli principle, it assumes an exponential form at reasonable distances. However, the Lennard-Jones potential, where the exponent is typically 9-12, is more robust since the repulsion term increases faster with decreasing distance than the attractive dispersion term.

For covalently bonded atoms, the Coulomb force is often subtracted, and the interaction is described with either a harmonic potential or the Morse potential [81]. The result is a potential where the parameters have physical significance. For instance, in the case of the Morse potential, the parameters become the dissociation energy of the diatomic species.

The following is a list of other two-body potential functions that are presently widely used [82]

3) Harmonic

$$V(r_{ij}) = \frac{1}{2} k_{ij} (r_{ij} - r_0)^2 \quad (3.21)$$

4) Morse

$$V(r_{ij}) = D_{ij} \{ [1 - \exp(-k_{ij}(r_{ij} - r_0))]^2 - 1 \} \quad (3.22)$$

5) Four-range Buckingham

$$V(r_{ij}) = \begin{cases} A_{ij} \exp\left(-\frac{r_{ij}}{\rho_{ij}}\right) & (r_{ij} \leq r_1) \\ a_{ij0} + a_{ij1}r_{ij} + a_{ij2}r_{ij}^2 + a_{ij3}r_{ij}^3 + a_{ij4}r_{ij}^4 + a_{ij5}r_{ij}^5 & (r_1 < r_{ij} \leq r_2) \\ b_{ij0} + b_{ij1}r_{ij} + b_{ij2}r_{ij}^2 + b_{ij3}r_{ij}^3 & (r_2 < r_{ij} \leq r_3) \\ -\frac{C_{ij}}{r_{ij}^6} & (r_{ij} > r_3) \end{cases} \quad (3.23)$$

6) Lennard-Jones Buffered

$$V(r_{ij}) = \frac{A_{ij}}{(r_{ij} + r_0)^m} - \frac{B_{ij}}{(r_{ij} + r_0)^n} \quad (3.24)$$

7) General/Del Re

$$V(r_{ij}) = \frac{A_{ij} \exp\left(-\frac{r_{ij}}{\rho_{ij}}\right)}{r_{ij}^m} - \frac{C_{ij}}{r_{ij}^n} \quad (3.25)$$

8) Rydberg

$$V(r_{ij}) = -A_{ij} \left(1 + B_{ij} \left(\frac{r_{ij}}{r_0} - 1\right)\right) \exp\left(-B_{ij} \left(\frac{r_{ij}}{r_0} - 1\right)\right) \quad (3.26)$$

9) Fermi-Dirac

$$V(r_{ij}) = \frac{A_{ij}}{1 + \exp(B_{ij}(r_{ij} - r_0))} \quad (3.27)$$

10) Inverse Gaussian

$$V(r_{ij}) = A_{ij} \exp(-B_{ij}(r_{ij} - r_0)^2) \quad (3.28)$$

11) Polynomial

$$V(r_{ij}) = c_{ij0} + c_{ij1}r_{ij} + c_{ij2}r_{ij}^2 + c_{ij3}r_{ij}^3 + c_{ij4}r_{ij}^4 + c_{ij5}r_{ij}^5 \quad (3.29)$$

12) Covalent exponential

$$V(r_{ij}) = -D_{ij} \exp\left(-\frac{a_{ij}(r_{ij} - r_0)^2}{2r_{ij}}\right) \quad (3.30)$$

$A_{ij}, B_{ij}, C_{ij}, D_{ij}, k_{ij}, a_{ijk} (k = 0 \sim 5), b_{ijk} (k = 0 \sim 5), c_{ijk} (k = 0 \sim 5)$, and ρ_{ij} are potential parameters of the pair of the i -th atom and the j -th atom, m and n are integers depending on the users' choices, r_{ij} and r_0 are the distance between two atoms and the reference distance, respectively, and r_{cutoff} is the cutoff distance for short-range interactions.

3.1.3 Many Body Potentials

Some important interactions for particular systems cannot be described by simply two-body force fields. Many-body potentials have been commonly used for metallic system, silicon, carbon and hydrocarbons, large molecules, etc. Below, a few higher-order interaction potentials are described.

1) The Embedded Atom Method

The embedded atom model (EAM) [83] is a successful approach for the description of a metallic system. Its foundation lies within the density functional theory, and it is based on the tenet that the energy is a function of the electron density. Simply, the EAM embeds a positively-charged ion into a linear superposition of spherically averaged atomic electron densities. Thus, instead of integrating the density across all space, the energy is expressed as a function of the density ρ_i at the nucleus i , summed over all atoms

$$V_{EAM} = \sum_{i=1}^N F(\rho_i) \quad (3.31)$$

and $\rho_i = \sum_{j \neq i}^N f(r_{ij})$, $f(r_{ij})$ is the contribution to the electron density from atom j at the

location of atom i .

In the original work of Sutton and Chen [84], which developed and extended the ideas of Finnis and Sinclair [85], a square root was used as the density functional, while the density

itself was represented as an inverse power of the interatomic distance. Eq.(3.31) encapsulates the idea that the interaction between any given pair of atoms is dependent on the number of other atoms within the coordination sphere.

2) Tersoff Potential

The Tersoff potential [86,87] is a three-body potential functional which explicitly includes an angular contribution of the force. The potential is widely used at present in various applications for silicon, carbon, germanium etc. The interatomic potential is taken to have the form

$$E = \sum_i E_i = \frac{1}{2} \sum_{i \neq j} V_{ij} \quad (3.32)$$

$$V_{ij} = f_c(r_{ij})[f_R(r_{ij}) + b_{ij}f_A(r_{ij})] \quad (3.33)$$

Here E is the total energy of the system, which is decomposed for convenience into a size energy E_i and a bond energy V_{ij} . The indices i and j run over the atoms of the system, and r_{ij} is the distance from atom to atom. b_{ij} represents a measure of the bond order, and is assumed to be a monotonically decreasing function of the coordination of atom i and j . The function f_R represents a repulsive pair potential, and f_A represents an attractive pair potential associated with bonding. The extra term f_c is merely a smooth cutoff function, to

limit the range of the potential, since for many applications short-ranged functions permit a tremendous reduction in computational effort.

Here the functions f_R , f_A and f_c are simply taken as

$$f_R(r_{ij}) = A_{ij} \exp(-\lambda_{ij} r_{ij}) \quad (3.34)$$

$$f_A(r_{ij}) = -B_{ij} \exp(-\mu_{ij} r_{ij}) \quad (3.35)$$

$$f_c(r_{ij}) = \begin{cases} 1, & r_{ij} < R_{ij} \\ \frac{1}{2} + \frac{1}{2} \cos[\pi(r_{ij} - R_{ij}) / (S_{ij} - R_{ij})], & R_{ij} < r_{ij} < S_{ij} \\ 0, & r_{ij} > S_{ij} \end{cases} \quad (3.36)$$

Where

$$\begin{aligned} b_{ij} &= \chi_{ij} (1 + \beta_i^n \xi_{ij}^{n_i})^{-1/2n_i} \\ \xi_{ij} &= \sum_{k \neq i, j} f_c(r_{ik}) \omega_{ik} g(\theta_{ijk}) \\ g(\theta_{ijk}) &= 1 + c_i^2 / d_i^2 - c_i^2 / [d_i^2 + (h_i - \cos \theta_{ijk})^2] \\ \omega_{ij} &= 1, \quad \chi_{ij} = 1, \\ A_{ij} &= (A_i A_j)^{1/2}, \quad B_{ij} = (B_i B_j)^{1/2}, \quad \lambda_{ij} = (\lambda_i + \lambda_j) / 2, \quad \mu_{ij} = (\mu_i + \mu_j) / 2, \\ R_{ij} &= (R_i R_j)^{1/2}, \quad S_{ij} = (S_i S_j)^{1/2} \end{aligned} \quad (3.37)$$

Here i , j and k labels the atoms of the system, θ_{ijk} is the bond angle between bond ij and ik . Single subscripted parameters, such as A_i , B_i , S_i , R_i , λ_i , n_i and μ_i , are material constants depending on the type of atom (C, Si or Ge). The energy is modeled as a sum of

pair-like interactions, where, however, the coefficient of the attractive term in the pair-like potential depends on the local environment, giving a many-body potential.

3) Stillinger-Weber Potential

Stillinger-Weber potential [88] is one of the first attempts to model a semiconductor. It is based on a two-body as well as a three-body term expressed as follows:

$$E = \sum_i \sum_{j>i} \phi_2(r_{ij}) + \sum_i \sum_{j \neq i} \sum_{k>j} \phi_3(r_{ij}, r_{ik}, \theta_{ijk})$$

$$\phi_2(r_{ij}) = A_{ij} \epsilon_{ij} \left[B_{ij} \left(\frac{\sigma_{ij}}{r_{ij}} \right)^{p_{ij}} - \left(\frac{\sigma_{ij}}{r_{ij}} \right)^{q_{ij}} \right] \exp \left(\frac{\sigma_{ij}}{r_{ij} - a_{ij} \sigma_{ij}} \right) \quad (3.38)$$

$$\phi_3(r_{ij}, r_{ik}, \theta_{ijk}) = \lambda_{ijk} \epsilon_{ijk} (\cos \theta_{ijk} - \cos \theta_{0ijk})^2 \exp \left(\frac{\gamma_{ij} \sigma_{ij}}{r_{ij} - a_{ij} \sigma_{ij}} \right) \exp \left(\frac{\gamma_{ik} \sigma_{ik}}{r_{ik} - a_{ik} \sigma_{ik}} \right)$$

In Eq.(3.38), θ_{ijk} is the angle formed between the ij bond and the ik bond. In particular,

$p_{ij} = 4$, $q_{ij} = 4$ and $\cos \theta_{0ijk} = -1/3$. Thus the potential can be rewritten as:

$$E = \sum_i \sum_{j>i} \phi_2(r_{ij}) + \sum_i \sum_{j \neq i} \sum_{k>j} \phi_3(r_{ij}, r_{ik}, \theta_{ijk})$$

$$\phi_2(r_{ij}) = A \epsilon \left[\frac{B \sigma^4}{r_{ij}^4} - 1 \right] \exp \left(\frac{\sigma}{r_{ij} - a \sigma} \right) \quad (3.39)$$

$$\phi_3(r_{ij}, r_{ik}, \theta_{ijk}) = \lambda \epsilon \left(\cos \theta_{ijk} + \frac{1}{3} \right)^2 \exp \left(\frac{\gamma \sigma}{r_{ij} - a \sigma} \right) \exp \left(\frac{\gamma \sigma}{r_{ik} - a \sigma} \right)$$

This potential gives a fairly realistic description of crystalline silicon. The potential parameters for carbon and germanium are also available in literature. Since Stillinger-

Weber potential is capable of modeling structural and dynamical properties with a very high precision, it is widely used in research and hence incorporated in our program.

3.2 Parameters for Empirical Interatomic Potentials

3.2.1 Parametrization Methods and Data Source

The reliability and hence the usefulness of atomistic modeling techniques is inherently limited by the availability of interatomic potentials of sufficient quality. The practical approach to derive empirical potentials for a given system may be fitting the form of the chosen potential model to experimental data typically measured from a simple binary or ternary system containing the interaction of interest. Such data includes the crystal structure, relative permittivities and elastic constants [89-91]. While much of the potential fitting work has been focused on one specific type of single crystalline solid, the routine application of such models to problems in solid-state chemistry involving complex materials further demands transferability of potentials between the systems for which they are derived and the system of interest [92-94].

Following this methodology, various groups of researchers have obtained their sets of potential parameters, each of which supports one specific structure group of crystals. For example, Levy et al [95] did the potential fitting study on perovskite with the structure $A^{2+}B^{4+}O_3^{2-}$, thus the parameters in that paper is suitable for the ions in this group of crystals. The philosophy is that within the same structure group of crystals, the anions and

cations shall behave the same in constructing the crystal structure, thus their potential functions shall be the same in another (but same structured) crystals. That is, for example, the Ti in PbTiO_3 should be the same Ti in BaTiO_3 , given that PbTiO_3 and BaTiO_3 are of same crystal structure. The consequence is that for each set of the parameters, the common anion interaction, oxygen-oxygen, shares the same value, while this parameter value may be different from another set in another publication. The potential fitting results for group of crystals are listed in Table 3-1 to Table 3-5: Lewis et al [93], Collins et al [96], Bush et al [92], Grimes et al [97,95,98].

Table 3-1: Buckingham potential parameter, Lewis et al (1985)

| Interaction type | A/eV | $\rho/\text{\AA}$ | $C/eV \text{\AA}^6$ |
|--------------------|--------|-------------------|---------------------|
| $Mg^{2+} - O^{2-}$ | 1428.5 | 0.2945 | 0.0 |
| $Ca^{2+} - O^{2-}$ | 1090.4 | 0.3437 | 0.0 |
| $Sr^{2+} - O^{2-}$ | 959.1 | 0.3721 | 0.0 |
| $Ba^{2+} - O^{2-}$ | 905.7 | 0.3976 | 0.0 |
| $Mn^{2+} - O^{2-}$ | 1007.4 | 0.3262 | 0.0 |
| $Fe^{2+} - O^{2-}$ | 1207.6 | 0.3084 | 0.0 |
| $Co^{2+} - O^{2-}$ | 1491.7 | 0.2951 | 0.0 |
| $Ni^{2+} - O^{2-}$ | 1582.5 | 0.2882 | 0.0 |
| $O^{2-} - O^{2-}$ | 22764 | 0.149 | 27.879 |

Table 3-2: Buckingham potential parameter, Collins et al (1992)

| Interaction type | A/eV | $\rho/\text{\AA}$ | $C/eV \text{\AA}^6$ |
|------------------|--------|-------------------|---------------------|
|------------------|--------|-------------------|---------------------|

| | | | |
|----------------------------|---------|--------|-------|
| $O^{2-} - O^{2-}$ | 22764.0 | 0.149 | 27.88 |
| $Si^{4+} - O^{2-}$ | 1283.9 | 0.3205 | 10.6 |
| $Si^{4+} - O^{1.426-} (H)$ | 999.9 | 0.3012 | 0 |
| $Al^{3+} - O^{2-}$ | 146.03 | 0.2991 | 0 |
| $K^+ - O^{2-}$ | 65269.7 | 0.2130 | 0 |
| $Mg^{2+} - O^{2-}$ | 1275.2 | 0.3012 | 0 |
| $Ni^{2+} - O^{2-}$ | 683.5 | 0.3332 | 0 |
| $Mg^{2+} - O^{2-}$ | 821.6 | 0.3242 | 0 |
| $Co^{2+} - O^{2-}$ | 696.3 | 0.3362 | 0 |
| $Fe^{2+} - O^{2-}$ | 694.1 | 0.3399 | 0 |
| $Zn^{2+} - O^{2-}$ | 499.6 | 0.3595 | 0 |
| $Mn^{2+} - O^{2-}$ | 715.8 | 0.3464 | 0 |
| $Cd^{2+} - O^{2-}$ | 868.3 | 0.3500 | 0 |

Table 3-3: Buckingham potential parameter, Bush et al (1994)

| Interaction type | A/eV | $\rho/\text{\AA}$ | $C/eV \text{\AA}^6$ |
|--------------------|----------|-------------------|---------------------|
| $Li^+ - O^{2-}$ | 426.480 | 0.3000 | 0.0 |
| $Na^+ - O^{2-}$ | 1271.504 | 0.3000 | 0.0 |
| $K^+ - O^{2-}$ | 3587.750 | 0.3000 | 0.0 |
| $Mg^{2+} - O^{2-}$ | 2457.243 | 0.2610 | 0.0 |
| $Ca^{2+} - O^{2-}$ | 2272.741 | 0.2986 | 0.0 |
| $Sr^{2+} - O^{2-}$ | 1956.702 | 0.3252 | 0.0 |
| $Ba^{2+} - O^{2-}$ | 4818.416 | 0.3067 | 0.0 |
| $Fe^{3+} - O^{2-}$ | 3219.335 | 0.2641 | 0.0 |
| $Ti^{4+} - O^{2-}$ | 2088.107 | 0.2888 | 0.0 |
| $Al^{3+} - O^{2-}$ | 2409.505 | 0.2649 | 0.0 |

| | | | |
|--------------------|-----------|--------|-------|
| $Ga^{3+} - O^{2-}$ | 2339.776 | 0.2742 | 0.0 |
| $Y^{3+} - O^{2-}$ | 1519.279 | 0.3291 | 0.0 |
| $La^{3+} - O^{2-}$ | 5436.827 | 0.2939 | 0.0 |
| $Pr^{3+} - O^{2-}$ | 13431.118 | 0.2557 | 0.0 |
| $Nd^{3+} - O^{2-}$ | 13084.217 | 0.2550 | 0.0 |
| $Gd^{3+} - O^{2-}$ | 866.339 | 0.3770 | 0.0 |
| $Eu^{3+} - O^{2-}$ | 847.868 | 0.3791 | 0.0 |
| $Tb^{3+} - O^{2-}$ | 845.137 | 0.3715 | 0.0 |
| $Yb^{3+} - O^{2-}$ | -991029 | 0.3515 | 0.0 |
| $O^{2-} - O^{2-}$ | 25.41 | 0.6937 | 32.32 |

Table 3-4: Buckingham potential parameter, Perovskite $A^{3+}B^{3+}O_3$ –
Grimes (2004)

| Interaction type | A/eV | $\rho/\text{\AA}$ | $C/eV \text{\AA}^6$ |
|--------------------|---------|-------------------|---------------------|
| $O^{2-} - O^{2-}$ | 9547.96 | 0.2192 | 32.0 |
| $Al^{3+} - O^{2-}$ | 1365.79 | 0.30096 | 2.538 |
| $Ce^{3+} - O^{2-}$ | 2034.18 | 0.34380 | 15.86 |
| $Cr^{3+} - O^{2-}$ | 1452.25 | 0.309 18 | 4.472 |
| $Dy^{3+} - O^{2-}$ | 1767.64 | 0.337 70 | 10.94 |
| $Er^{3+} - O^{2-}$ | 1678.21 | 0.337 81 | 10.81 |
| $Eu^{3+} - O^{2-}$ | 1886.71 | 0.339 75 | 11.997 |
| $Fe^{3+} - O^{2-}$ | 1478.98 | 0.313 06 | 6.960 |
| $Ga^{3+} - O^{2-}$ | 1456.72 | 0.309 88 | 4.616 |
| $Gd^{3+} - O^{2-}$ | 1868.75 | 0.338 80 | 11.62 |
| $Ho^{3+} - O^{2-}$ | 1726.29 | 0.337 76 | 10.72 |
| $In^{3+} - O^{2-}$ | 1595.65 | 0.329 60 | 7.402 |

| | | | |
|--------------------|---------|----------|-------|
| $La^{3+} - O^{2-}$ | 2051.32 | 0.345 85 | 15.51 |
| $Lu^{3+} - O^{2-}$ | 1561.36 | 0.338 54 | 10.01 |
| $Nd^{3+} - O^{2-}$ | 1979.11 | 0.341 48 | 13.07 |
| $Pr^{3+} - O^{2-}$ | 2025.54 | 0.342 70 | 13.83 |
| $Sc^{3+} - O^{2-}$ | 1587.95 | 0.321 90 | 8.143 |
| $Sm^{3+} - O^{2-}$ | 1944.44 | 0.340 80 | 12.49 |
| $Tb^{3+} - O^{2-}$ | 1818.00 | 0.338 45 | 14.33 |
| $Y^{3+} - O^{2-}$ | 1721.23 | 0.338 21 | 10.29 |
| $Yb^{3+} - O^{2-}$ | 1616.68 | 0.337 98 | 13.34 |

Table 3-5: Buckingham potential parameter, Pyrochlore - Grimes
(2002)

| Interaction type | A/eV | $\rho/\text{\AA}$ | $C/eV \text{\AA}^6$ |
|--------------------|-----------|-------------------|---------------------|
| $O^{2-} - O^{2-}$ | 35 686.18 | 0.2010 | 32.00 |
| $Lu^{3+} - O^{2-}$ | 2 062.99 | 0.3086 | 16.87 |
| $Yb^{3+} - O^{2-}$ | 2 251.26 | 0.3052 | 16.57 |
| $Er^{3+} - O^{2-}$ | 2 115.00 | 0.3111 | 17.55 |
| $Y^{3+} - O^{2-}$ | 2 442.60 | 0.3054 | 17.51 |
| $Gd^{3+} - O^{2-}$ | 2 214.40 | 0.3154 | 19.90 |
| $Eu^{3+} - O^{2-}$ | 2 468.00 | 0.3114 | 20.59 |
| $Sm^{3+} - O^{2-}$ | 2 074.70 | 0.3215 | 21.49 |
| $Nd^{3+} - O^{2-}$ | 2 148.14 | 0.3227 | 22.59 |
| $Pr^{3+} - O^{2-}$ | 2 313.21 | 0.3212 | 23.94 |
| $La^{3+} - O^{2-}$ | 2 266.26 | 0.3276 | 23.25 |
| $Ti^{4+} - O^{2-}$ | 1 859.40 | 0.2959 | 0.00 |
| $Ru^{4+} - O^{2-}$ | 1 889.34 | 0.2974 | 0.00 |

| | | | |
|--------------------|----------|--------|-------|
| $Mo^{4+} - O^{2-}$ | 1 899.18 | 0.3016 | 0.00 |
| $Sn^{4+} - O^{2-}$ | 1 168.41 | 0.3417 | 13.66 |
| $Zr^{4+} - O^{2-}$ | 1 402.57 | 0.3312 | 5.10 |
| $Pb^{4+} - O^{2-}$ | 1 401.36 | 0.3433 | 19.50 |

Note that there are also other researches that each is focused on just one crystal. This kind of potential parameters may be best fitted to all the properties of the targeting crystal, or at least the properties the paper was investigating into and fitting upon. Table 3-6 - Table 3-10 show the Buckingham potential parameters for $PbTiO_3$, $BaTiO_3$, $BiScO_3$, $KNbO_3$, and $KTaO_3$, respectively (Exner et al [99]; Sepiarsky et al [100]; Tinte [101])

Table 3-6: Buckingham potential parameters for $PbTiO_3$

| Interaction type | A/eV | $\rho/\text{\AA}$ | $C/eV \text{\AA}^6$ |
|--------------------|----------|-------------------|---------------------|
| $Pb^{2+} - O^{2-}$ | 613.4160 | 0.387 | 0.0 |
| $Ti^{4+} - O^{2-}$ | 270.950 | 0.588 | 0.0 |
| $O^{2-} - O^{2-}$ | 9547.96 | 0.2192 | 32.32 |

Table 3-7: Buckingham potential parameters for $BaTiO_3$

| Interaction type | A/eV | $\rho/\text{\AA}$ | $C/eV \text{\AA}^6$ |
|--------------------|---------|-------------------|---------------------|
| $Ba^{2+} - O^{2-}$ | 1061.30 | 0.374 | 0.0 |
| $Ti^{4+} - O^{2-}$ | 3769.93 | 0.259 | 0.0 |

| | | | |
|-------------------|---------|-------|-------|
| $O^{2-} - O^{2-}$ | 4740.00 | 0.269 | 160.0 |
|-------------------|---------|-------|-------|

Table 3-8: Buckingham potential parameters for BiScO₃

| Interaction type | A/eV | $\rho/\text{\AA}$ | $C/eV \text{\AA}^6$ |
|------------------------------|----------|-------------------|---------------------|
| $Bi^{2.5253+} - O^{1.7268-}$ | 358.587 | 0.4258 | 0.0 |
| $Sc^{2.6550+} - O^{1.7268-}$ | 503.411 | 0.4075 | 0.0 |
| $O^{1.7268-} - O^{1.7268-}$ | 4758.190 | 0.2811 | 310.005 |

Table 3-9: Buckingham potential parameters for KNbO₃

| Interaction type | A/eV | $\rho/\text{\AA}$ | $C/eV \text{\AA}^6$ |
|--------------------|----------|-------------------|---------------------|
| $K^{1+} - O^{2-}$ | 124189.4 | 0.3516 | 0.0 |
| $Nb^{5+} - O^{2-}$ | 1131.3 | 0.4972 | 0.0 |
| $O^{2-} - O^{2-}$ | 3576.9 | 0.3516 | 833.5 |

Table 3-10: Buckingham potential parameters for KTaO₃

| Interaction type | A/eV | $\rho/\text{\AA}$ | $C/eV \text{\AA}^6$ |
|--------------------|----------|-------------------|---------------------|
| $K^+ - O^{2-}$ | 523.156 | 0.34356 | 0.0 |
| $Ta^{5+} - O^{2-}$ | 1315.572 | 0.36905 | 0.0 |
| $O^{2-} - O^{2-}$ | 22764.3 | 0.149 | 27.627 |

3.2.2 Combining Scheme

Now that a database of interatomic potential parameters has been established, the question comes how to use these different sets of potential parameters simultaneously when one is about to solve a complex material system with many different types of crystals in the specimen. This problem can be solved by the following assumptions and techniques:

(i) The cation – cation interactions are considered to be purely coulombic. Therefore, the potential function is easily determined once the charges on the ions are known.

(ii) The cation – anion interactions, which are of the Born-Mayer form, opt to use the parameters developed for the specific crystal structure that appears in the simulation case. For example, the parameters for $\text{Mg}^{2+} - \text{O}^{2-}$ in rocksalt structure MgO and $\text{Ba}^{2+} - \text{O}^{2-}$ in rocksalt structure BaO should be found from the potential parameter set by Lewis [93]; while the parameters for $\text{Ba}^{2+} - \text{O}^{2-}$ in perovskite structure BaTiO_3 need to be from Bush et al [92].

(iii) The anion – anion interactions, that is $\text{O}^{2-} - \text{O}^{2-}$, are considered to follow the same approach as in (ii) to get the parameters to describe the oxygen-oxygen relation within the same type of structure (thus from the same data source). For the oxygen-oxygen interaction between different types of structure (thus from different data source), the oxygen ions are considered as different species, therefore, a combination rule shall be applied to bridge these species.

The above treatments (i)-(iii) solve the problem of using different data sources so that a large complex system with various kinds of chemical compound can be studied. These treatments are considered as the "protocols" that link different data sources of potential parameter, as illustrated in Figure 3-3. This is the key to the modeling and simulation of polycrystalline materials with multiple kinds of elements and multiple types of crystals.

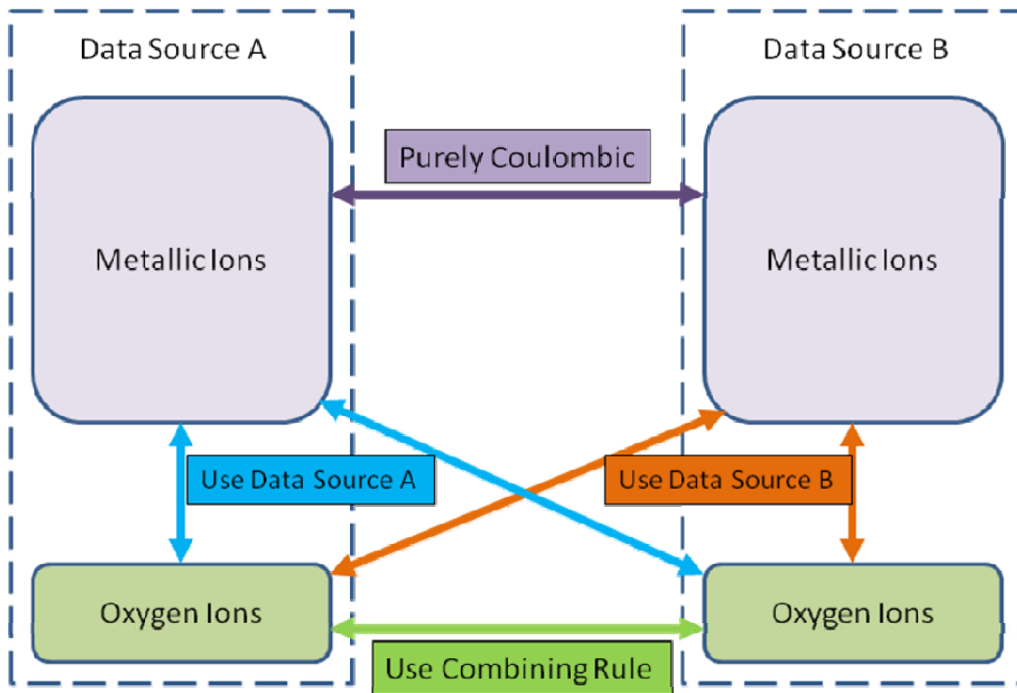


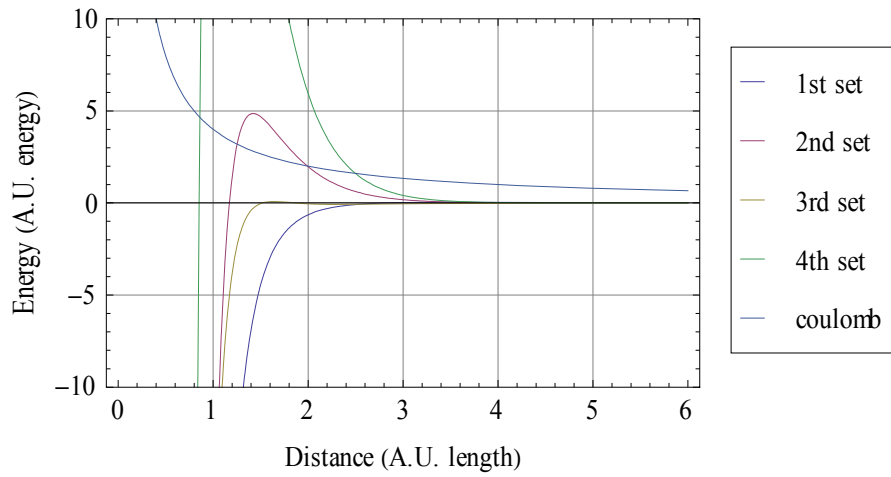
Figure 3-3: Protocols that link different data sources of potential parameters.

Now the combination rule mentioned in (iii) is to be elaborated. For example, four sets of parameters of $O^{2-} - O^{2-}$ interaction from four different data sources are to be evaluated, as listed in Table 3-11.

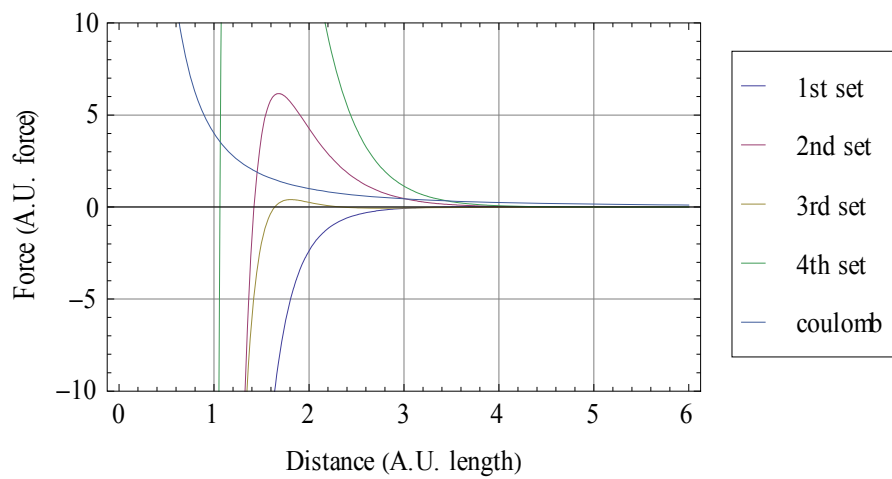
Table 3-11: $O^{2-} - O^{2-}$ parameters from four sources

| Number | Interaction Type | A/eV | $\rho/\text{\AA}$ | $C/eV\text{\AA}^6$ | Source |
|--------|-------------------|----------|-------------------|--------------------|--------|
| 1 | $O^{2-} - O^{2-}$ | 25.41 | 0.6937 | 32.32 | Bush |
| 2 | $O^{2-} - O^{2-}$ | 9547.96 | 0.2192 | 32.0 | Levy |
| 3 | $O^{2-} - O^{2-}$ | 22764 | 0.149 | 27.879 | Lewis |
| 4 | $O^{2-} - O^{2-}$ | 35686.18 | 0.2010 | 32.0 | Grimes |

From the plot of the potential energy profile and force profile, as shown in Figure 3-4, it is seen that there is much difference among these different sets of data.



(a) Potential energy



(b) Force

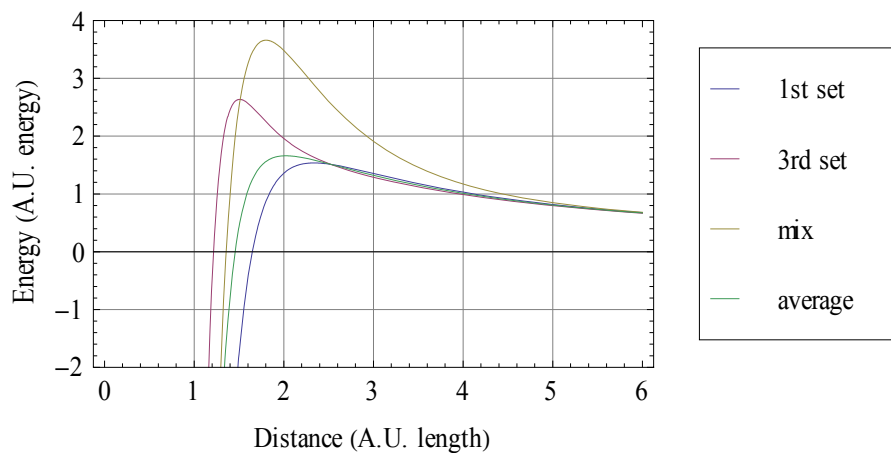
Figure 3-4: Potential energy and force profiles of $O^{2-} - O^{2-}$ with the parameters from Table 3-11

Therefore, when it comes to use any two of them, a combination rule is needed such that the mixed potential should be a fair interpolation of these two potentials. A good

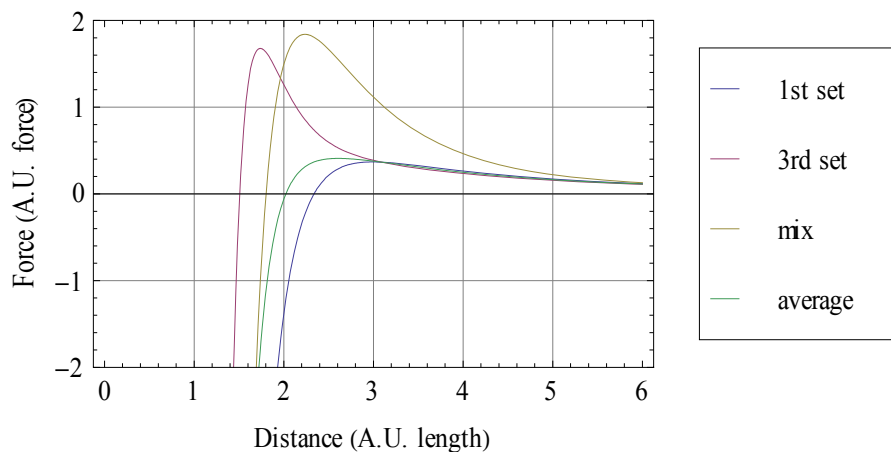
interpolation requires that the interpolated values of potential and force matches the averaging value of the two original potentials. In the literature, it is common to calculate the mixed parameters using the combination rule proposed by Mirskaya [102,103]:

$$\left. \begin{aligned} A_{ij} &= (A_{ii} \cdot A_{jj})^{1/2} \\ \rho_{ij} &= \frac{1}{2}(\rho_{ii} + \rho_{jj}) \\ C_{ij} &= (C_{ii} \cdot C_{jj})^{1/2} \end{aligned} \right\} \quad (3.40)$$

Here the index i and j indicate the potential parameters between the i -th species and j -th species of atom/ion. It is found, however, that this simple rule may not always yield the promising mixed potential parameter for two species. For example, for the 1st set and 3rd set, if the above rule is applied, the mixed potential, as Figure 3-5, will seem to be out of the bound of the original two, rather than being the average.



(a) Potential energy



(b) Force

Figure 3-5: Potential energy and force profiles of 1st set, 3rd set of $O^{2-} - O^{2-}$ and their interpolation by common combination rule (Mirskaya)

Since the dataset is a definite collection, a case-by-case potential evaluation is made for every pair combination among the four sets of parameters. Here 3 types of averaging methods are introduced and thus used for the interpolation of the parameters A , ρ and C .

(i) Arithmetic Mean (AM):

$$AM = \frac{1}{2}(X_1 + X_2) \quad (3.41)$$

(ii) Geometric Mean (GM):

$$GM = \sqrt{X_1 \cdot X_2} \quad (3.42)$$

(iii) Harmonic Mean (HM):

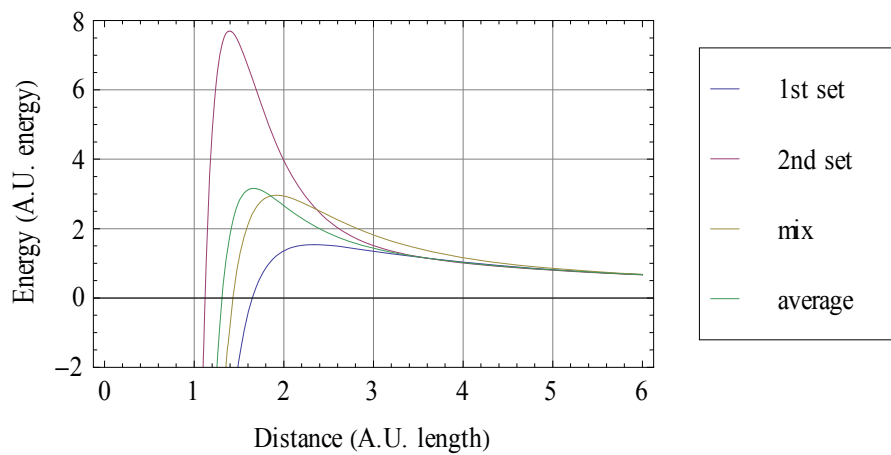
$$HM = \frac{2}{\frac{1}{X_1} + \frac{1}{X_2}} \quad (3.43)$$

Through evaluating the mixed potential profiles with different averaging methods, the optimal selection is obtained and thus summarized in Table 3-12:

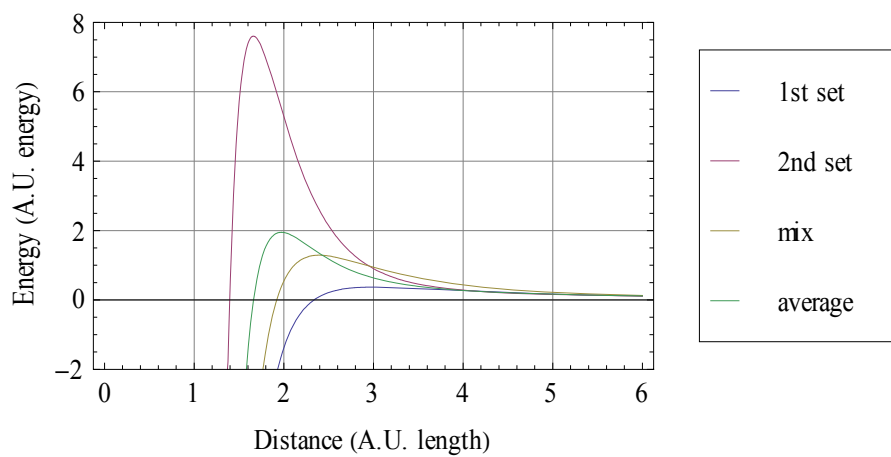
Table 3-12: The combination rule of mixing $O^{2-} - O^{2-}$ parameters from the data sets in Table 3-11

| | A/eV | $\rho/\text{\AA}$ | $C/eV\text{\AA}^6$ | A/eV | $\rho/\text{\AA}$ | $C/eV\text{\AA}^6$ | A/eV | $\rho/\text{\AA}$ | $C/eV\text{\AA}^6$ | A/eV | $\rho/\text{\AA}$ | $C/eV\text{\AA}^6$ | | | | | | | | | | | | | | | |
|---|--------|-------------------|--------------------|--------|-------------------|--------------------|--------|-------------------|--------------------|--------|-------------------|--------------------|----|----|----|--|--|--|--|--|--|--|--|--|----|----|----|
| | 1 | | | 2 | | | 3 | | | 4 | | | | | | | | | | | | | | | | | |
| 1 | | | | | | | | | | | | | | | | | | | | | | | | | | | |
| 2 | | | | | | | | | | | | | GM | AM | GM | | | | | | | | | | | | |
| 3 | | | | | | | | | | | | | GM | HM | GM | | | | | | | | | | HM | AM | GM |
| 4 | | | | | | | | | | | | | GM | AM | GM | | | | | | | | | | AM | HM | GM |

With this combination rule, as given in Table 3-12, the mixed potentials and forces are achieved, as shown in Figure 3-6 to Figure 3-11.

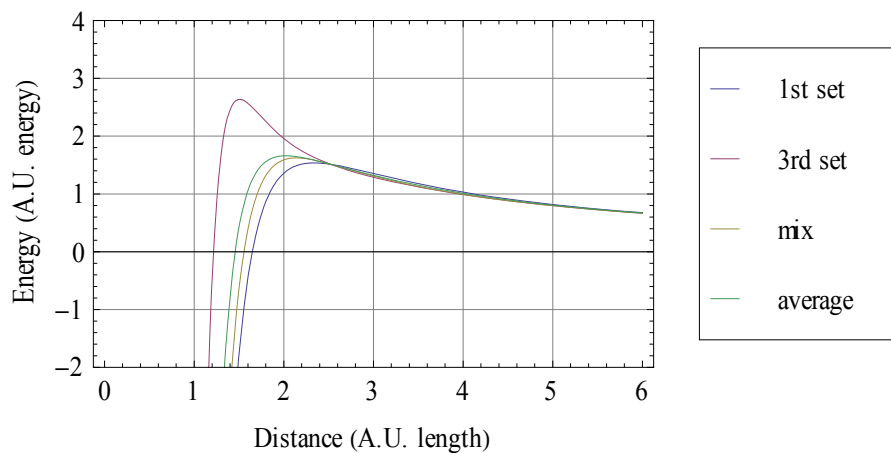


(a) Potential energy

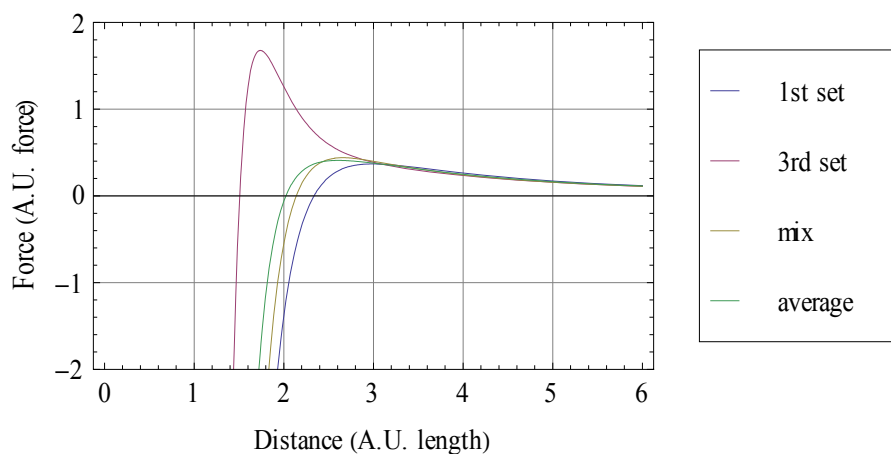


(b) Force

Figure 3-6: Potential energy and force profiles of 1st set, 2nd set of O^{2-} – O^{2-} and their optimal interpolation

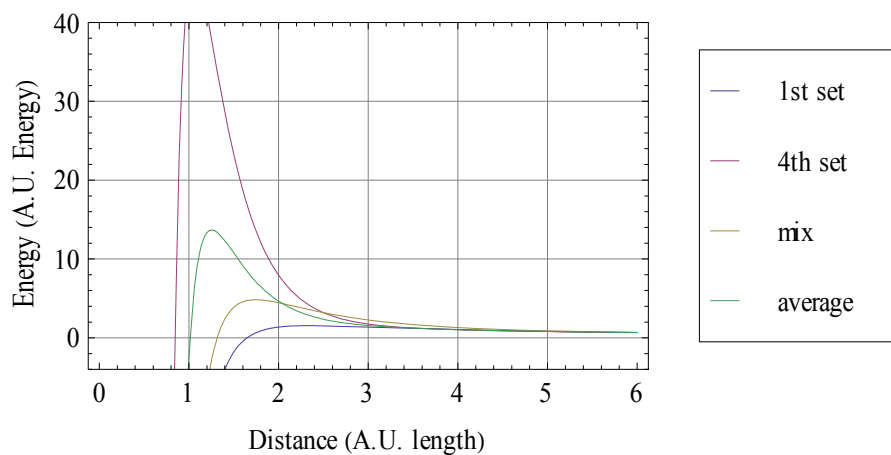


(a) Potential energy

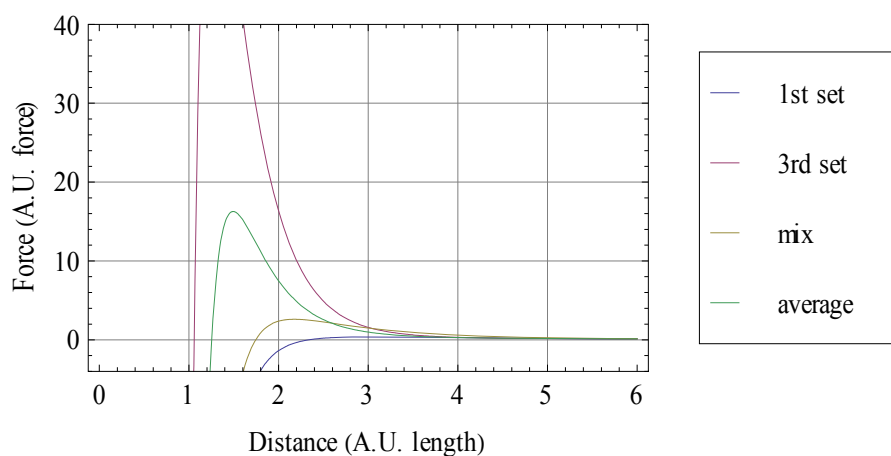


(b) Force

Figure 3-7: Potential energy and force profiles of 1st set, 3rd set of O^{2-} – O^{2-} and their optimal interpolation

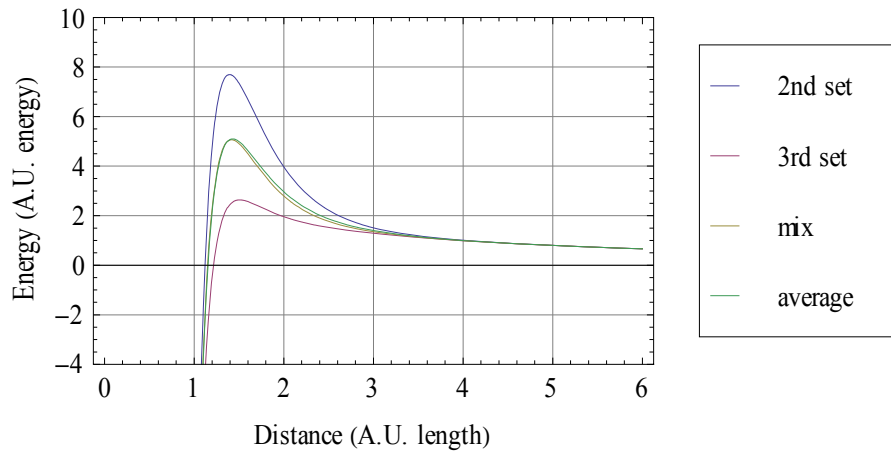


(a) Potential energy

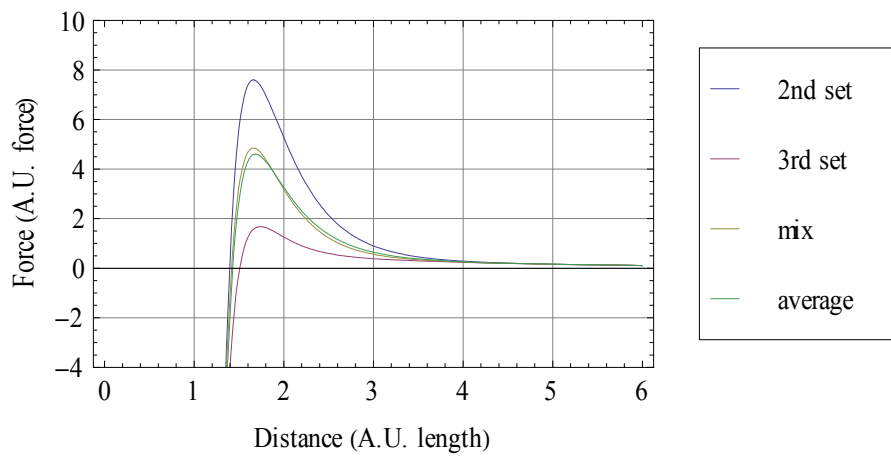


(b) Force

Figure 3-8: Potential energy and force profiles of 1st set, 4th set of O^{2-} – O^{2-} and their optimal interpolation

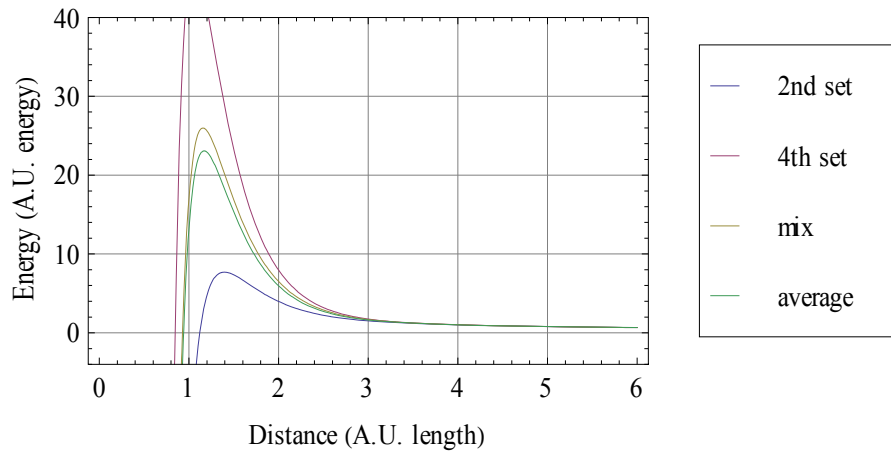


(a) Potential energy

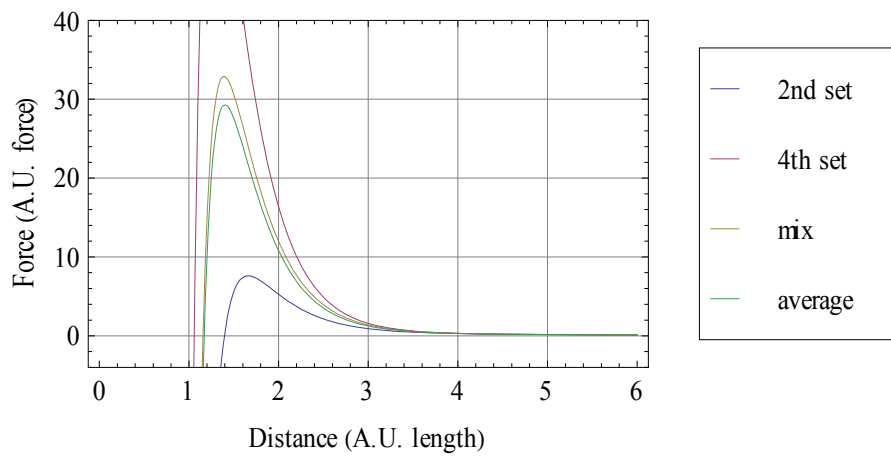


(b) Force

Figure 3-9: Potential energy and force profiles of 2nd set, 3rd set of O^{2-} – O^{2-} and their optimal interpolation



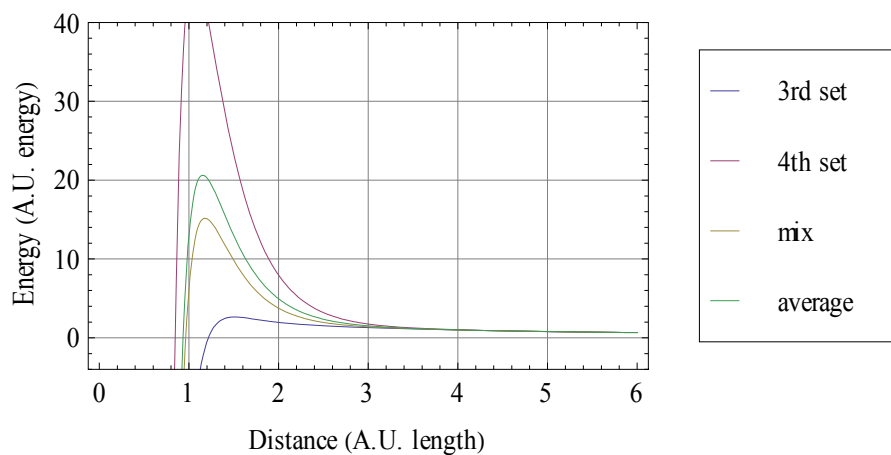
(a) Potential energy



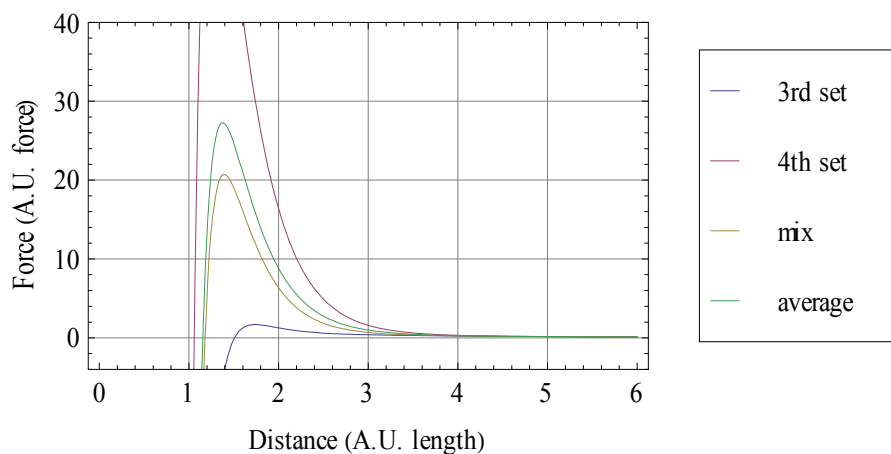
(b) Force

Figure 3-10: Potential energy and force profiles of 2nd set, 4th set of O^{2-}

– O^{2-} and their optimal interpolation



(a) Potential energy



(b) Force

Figure 3-11: Potential energy and force profiles of 3rd set, 4th set of O²⁻ – O²⁻ and their optimal interpolation

In the above 6 pair combinations, in most of the cases the mixed potential matches the average value very well while in others cases the mixed potential is close to the average

value. It can be concluded that all these cases provide a reasonable mixed potential. It is expected that this combination scheme will provide an energy/force profile that smoothly connects oxygen atoms/ions as described by different parameter sets, meanwhile the merits of each parameter set will be best preserved. Therefore the overall properties of single crystals and polycrystals can be best calculated.

3.2.3 Remedy to Avoid Buckingham Catastrophe

In the original Coulomb-Buckingham potential, there is a potential barrier existed to prevent the collision of two oxygen atoms at a critical distance. This means if the interatomic distance is less than the critical distance, the interatomic force becomes attractive instead of repulsive. It is seen that when the relative distance of two atoms gets smaller, the r^{-6} term dominates and approach to negative infinity. This attraction will cause the paired atom to move even closer and thus induces instability. This violates the physics and it is referred as Buckingham Catastrophe [104]. Chen and Lee investigated how the Buckingham Catastrophe affects the multiscale modeling of fracture and pointed out that adding the remedy term r^{-12} will correct the wrong physics and provides a reasonable interatomic potential [105-107].

Equation (3.44) gives the full representation of the modified Coulomb-Buckingham potential after the r^{-12} term is added. The coefficient of the remedy D_{ij} shares the same numerical value as C_{ij} in the units of eV and angstrom.

$$V(r_{ij}) = \frac{q_i q_j}{r_{ij}} + A_{ij} \exp\left(-\frac{r_{ij}}{\rho_{ij}}\right) - \frac{C_{ij}}{r_{ij}^6} + \frac{D_{ij}}{r_{ij}^{12}} \quad (3.44)$$

3.3 Summary

The heart of atomistic simulations is the interatomic potential. In classical simulations the atoms are most often represented by point-like centers which interact through two, three or many-body interaction potentials. In this chapter, a list of different types of interatomic potentials is introduced, which are adequate to solve a vast variety of materials. Then, an interatomic potential parameter database is established for the Coulomb-Buckingham potential. Combination techniques have been developed to relate different parameter sets so that potential parameters from different data source can be used simultaneously and their own merits can be best preserved. The parameter sets, as given in Table 3-1 to Table 3-10, cover the elements marked red in the periodic table as shown in Table 3-13. It means that this research is capable of simulating nanopolycrystalline materials that consist of a variety of chemical elements. Lastly, a remedy of a higher order term is recommended to be included in Buckingham potential in order to avoid Buckingham catastrophe, which is unphysical.

Table 3-13: Periodic table (red colored elements are covered in the potential parameter database)

| | | | | | | | | | | | | | | | | | | | |
|---|----|-----|------|-----|----|-----|------|-------|-------|-------|----|-----|----|-----|----|----|----|-------|----|
| | IA | | | | | | | | | | | | | | | | | VIIIB | |
| 1 | H | IIA | | | | | | | | | | | | | | | | | He |
| 2 | Li | Be | | | | | | | | | | | B | C | N | O | F | Ne | |
| 3 | Na | Mg | IIIA | IVA | VA | VIA | VIIA | [---- | VIIIA | ----] | IB | IIB | Al | Si | P | S | Cl | Ar | |
| 4 | K | Ca | Sc | Ti | V | Cr | Mn | Fe | Co | Ni | Cu | Zn | Ga | Ge | As | Se | Br | Kr | |
| 5 | Rb | Sr | Y | Zr | Nb | Mo | Tc | Ru | Rh | Pd | Ag | Cd | In | Sn | Sb | Te | I | Xe | |
| 6 | Cs | Ba | * | Hf | Ta | W | Re | Os | Ir | Pt | Au | Hg | Tl | Pb | Bi | Po | At | Rn | |
| 7 | Fr | Ra | ** | Rf | Db | Sg | Bh | Hs | Mt | Uun | | | | Uuq | | | | | |
| | | | * | La | Ce | Pr | Nd | Pm | Sm | Eu | Gd | Tb | Dy | Ho | Er | Tm | Yb | Lu | |
| | | | ** | Ac | Th | Pa | U | Np | Pu | Am | Cm | Bk | Cf | Es | Fm | Md | No | Lr | |

CHAPTER 4: NANOPOLYCRYSTALLINE MATERIAL SYSTEM

The properties of a material are influenced profoundly by its microstructure. For nanopolycrystalline materials, the material characteristics are strongly influenced by their definitive (generic) structural peculiarities which are nanoscopic size of grains and high volume fraction of the interfacial phase. Besides these definitive structural peculiarities, there are structural peculiarities that can be different in different nanopolycrystalline materials with the same mean grain size and are sensitive to material characteristics. These non-generic structural peculiarities of nanopolycrystalline materials include typical grain shape, grain-size distribution, grain phase, and inter-phase boundaries, etc. Therefore, if one is to generate atomistic models, which are sufficiently realistic to calculate properties or simulate processes with sufficient accuracy to be of benefit to experiment, a strategy for introducing such microstructure into a model is required.

This chapter starts with the energy minimization technique to find realistic crystal structures in computer simulation. Then, it presents a general strategy for constructing full atomistic models of nanopolycrystalline materials with grains of arbitrary and controllable grain type/orientation/distribution, and grain boundaries of amorphous phase/tight connection.

4.1 Crystal Structures

In mineralogy and crystallography, a crystal structure is a unique arrangement of atoms or molecules in a crystalline liquid or solid. A crystal structure describes a highly ordered structure, occurring due to the intrinsic nature of molecules to form symmetric patterns. A crystal structure can be thought of as an infinitely repeating array of 3D 'boxes', known as unit cells. The unit cell is calculated from the simplest possible representation of molecules, known as the asymmetric unit. The asymmetric unit is translated to the unit cell through symmetry operations, and the resultant crystal lattice is constructed through repetition of the unit cell infinitely in 3-dimensions. Patterns are located upon the points of a lattice, which is an array of points repeating periodically in three dimensions. The lengths of the edges of a unit cell and the angles between them are called the lattice parameters. The symmetry properties of the crystal are embodied in its space group.

In this research, several typical crystal structures are investigated and thus introduced here.

4.1.1 Rocksalt

In the type of rocksalt, each of the two atom types forms a separate face-centered cubic lattice, with the two lattices interpenetrating so as to form a 3D checkerboard pattern [108]. Examples of compounds with this structure include sodium chloride (NaCl) itself, along with almost all other alkali halides, and “many divalent metal oxides, sulfides, selenides,

and tellurides” [109]. More generally, this structure is more likely to be formed if the cation is slightly smaller than the anion (a cation/anion radius ratio of 0.414 to 0.732).

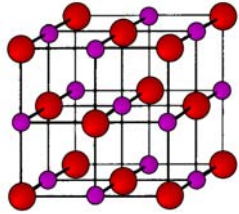
| Illustration | Atom position in unit cell | Base vector |
|---|---|--|
|  | $Mg: (0, 0, 0) \quad O: (\frac{1}{2}, 0, 0)$ $Mg: (\frac{1}{2}, \frac{1}{2}, 0) \quad O: (0, \frac{1}{2}, 0)$ $Mg: (\frac{1}{2}, 0, \frac{1}{2}) \quad O: (0, 0, \frac{1}{2})$ $Mg: (0, \frac{1}{2}, \frac{1}{2}) \quad O: (\frac{1}{2}, \frac{1}{2}, \frac{1}{2})$ | $\mathbf{V}^1 = (1, 0, 0)$ $\mathbf{V}^2 = (0, 1, 0)$ $\mathbf{V}^3 = (0, 0, 1)$ |

Figure 4-1: Structure of rocksalt (e.g. MgO)

4.1.2 Perovskite

The perovskite structure is adopted by many oxides that have the chemical formula ABO_3 [110,111]. In the idealized cubic unit cell of such a compound, type 'A' atom sits at cube corner positions $(0, 0, 0)$, type 'B' atom sits at body center position $(\frac{1}{2}, \frac{1}{2}, \frac{1}{2})$ and oxygen atoms sit at face centered positions $(\frac{1}{2}, \frac{1}{2}, 0)$.

Perovskite materials exhibit many interesting and intriguing properties from both the theoretical and the application point of view. Colossal magnetoresistance, ferroelectricity, superconductivity, charge ordering, spin dependent transport, high thermopower and the interplay of structural, magnetic and transport properties are commonly observed features in this family. These compounds are used as sensors and catalyst electrodes in certain types of fuel cells and are candidates for memory devices and spintronics applications.

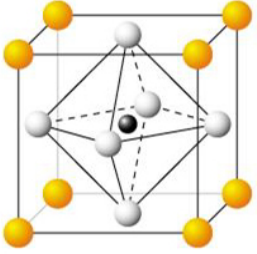
| Illustration | Atom position in unit cell | Base vector |
|--|--|--|
|  | $A: (0, 0, 0)$ $B: \left(\frac{1}{2}, \frac{1}{2}, \frac{1}{2}\right)$ $O: \left(\frac{1}{2}, \frac{1}{2}, 0\right), \left(\frac{1}{2}, 0, \frac{1}{2}\right), \left(0, \frac{1}{2}, \frac{1}{2}\right)$ | $\mathbf{V}^1 = (1, 0, 0)$ $\mathbf{V}^2 = (0, 1, 0)$ $\mathbf{V}^3 = (0, 0, 1)$ |

Figure 4-2: Structure of perovskite (ABO_3)

4.1.3 Wurtzite

The wurtzite crystal structure, named after the mineral wurtzite, is a crystal structure for various binary compounds [112,110]. It is an example of a hexagonal crystal system. The

chemical prototype is conventionally given as ZnS, although mineral wurtzite is a multi-component alloy compound.

Among the compounds that can take the wurtzite structure are wurtzite itself, AgI, ZnO, CdS, CdSe, α -SiC, GaN, AlN, BN and other semiconductors. In most of these compounds, wurtzite is not the favored form of the bulk crystal, but the structure can be favored in some nanocrystalline forms of the material.

The wurtzite structure is non-centrosymmetric (i.e., lacks inversion symmetry). Due to this, wurtzite crystals can (and generally do) have properties such as piezoelectricity and pyroelectricity, which centrosymmetric crystals lack.

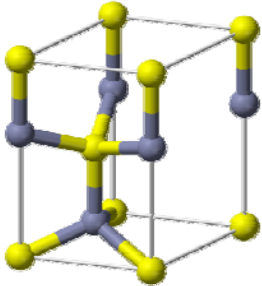
| Illustration | Atom position in unit cell | Base vector |
|---|--|--|
|  | $S: (0, 0, 0)$ $S: (0, \frac{\sqrt{3}}{3}a, \frac{1}{2}b)$ $Zn: (0, 0, c)$ $Zn: (0, \frac{\sqrt{3}}{3}a, c - \frac{1}{2}b)$ | $\mathbf{V}^1 = (a, 0, 0)$ $\mathbf{V}^2 = (-\frac{1}{2}a, \frac{\sqrt{3}}{2}a, 0)$ $\mathbf{V}^3 = (0, 0, b)$ |

Figure 4-3: Structure of perovskite (ABO_3)

4.1.4 Pyrochlore

The Pyrochlore crystal structure describes materials of the type $A_2B_2O_6$ and $A_2B_2O_7$, where the A and B species are generally rare-earth or transition metal species [113,114]; e.g. $Y_2Ti_2O_7$. The pyrochlore structure is a super structure derivative of the simple fluorite structure. These systems are particularly susceptible to geometrical frustration and novel magnetic effects.

The pyrochlore structure shows varied physical properties ranging from electronic insulators (e.g. $La_2Zr_2O_7$), ionic conductors ($Gd_{1.9}Ca_{0.1}Ti_2O_{6.9}$), metallic conductivity ($Bi_2Ru_2O_{7-y}$), mixed ionic and electronic conductivity, spin ice systems ($Dy_2Ti_2O_7$), spin glass systems ($Y_2Mo_2O_7$), and superconducting material ($Cd_2Re_2O_7$).

4.2 Structural Optimization of Crystals

Structural optimization to find the minimum energy structure at zero temperature is a method to find the static properties of crystals. It also provides a way to compare the computation results and experimental results.

For a given lattice structure, the internal energy is the summation of all interatomic potentials within this system,

$$V^{total} = V^{total}(\mathbf{r}_1, \mathbf{r}_2, \mathbf{r}_3, \dots, \mathbf{r}_N) = \sum_{i=1}^N V_i(\mathbf{r}_i) \quad (4.1)$$

where, $V_i(\mathbf{r}_i)$ represents the energy associated with the i -th atom located at \mathbf{r}_i , and i sums over the total number of atoms in the system.

Usually, the lattice structure is to be determined for the bulk materials, so the infinite regular aligned specimen is considered. In that sense, the energy of one unit cell V^{unit} is calculated instead of V^{total} . And V^{unit} can be expressed as the function of three lattice constants, a , b and c , three lattice angles, α , β and γ , and $l-1$ atomic position vectors,

$$V^{unit} = V^{unit}(a, b, c, \alpha, \beta, \gamma, \mathbf{r}_1, \mathbf{r}_2, \mathbf{r}_3, \dots, \mathbf{r}_{l-1}) = \sum_{i=1}^l V_i \quad (4.2)$$

where l is the number of atoms within one unit cell. Then the equilibrium and optimized structure requires that

$$\left(\frac{\partial V^{unit}}{\partial I_i} \right)_{i=1,2,\dots,3l+3} = 0 \quad (4.3)$$

where I_i represents all possible geometric components associated with the lattice $(a, b, c, \alpha, \beta, \gamma, \mathbf{r}_1, \mathbf{r}_2, \mathbf{r}_3, \dots, \mathbf{r}_{l-1})$. They will be the design variables in the structural optimizations. In the case of lattice structure under certain symmetry, the number of design variables may be reduced. Naturally, Eq.(4.3) further implies that the forces acting on each atom and the stress of the system should be zero automatically when the minimum energy is achieved.

The computation results in this research demonstrate that the energy minimized structure indeed has zero forces and zero stresses. It is noted that the minimized energy may not be the global minimum, because there would be different symmetry constraints or external strains applied to the system for the structural optimization. The global minimum energy is only associated with the lattice structure in the existing lowest symmetry, namely the ground state of one crystal. In that sense, it provides a reasonable way to explore the different phases for multiphase materials and the ground state of such materials. Certain symmetry requirements are defined as the optimization constraints according to the general geometry of crystal structures.

Table 4-1 shows the structural optimization results and experimental results for several crystals, including wurtzite, zincblende, rocksalt, and perovskite. It is noted that three phases of ZnO (wurtzite, zincblende, and rocksalt) are captured via structural optimization, which represents three local minimum energies. It is seen that the computation results are in great agreement with the experimental data as found from Springer Material Science Online Database [115].

Table 4-1: Structural Optimization Results and Experimental Results
for Several Crystals

| | Optimization Result | Experimental Result |
|---------------------------------|--|---|
| ZnO (Wurtzite) | $a = b = 3.24 \text{ \AA}, c = 5.08 \text{ \AA}$ | $a = b = 3.25 \text{ \AA}, c = 5.2 \text{ \AA}$ |
| ZnO (Zincblende) | $a = b = c = 4.51 \text{ \AA}$ | $a = b = c = 4.37 \sim 4.47 \text{ \AA}$ |
| ZnO (Rocksalt) | $a = b = c = 4.28 \text{ \AA}$ | $a = b = c = 4.06 \sim 4.32 \text{ \AA}$ |
| PbTiO ₃ (Perovskite) | $a = b = c = 3.81 \text{ \AA}$ | $a = b = c = 3.97 \text{ \AA}$ |
| BaTiO ₃ (Perovskite) | $a = b = c = 3.99 \text{ \AA}$ | $a = b = c = 4.00 \text{ \AA}$ |
| KNbO ₃ (Perovskite) | $a = b = c = 4.00 \text{ \AA}$ | $a = b = c = 4.02 \text{ \AA}$ |
| KTaO ₃ (Perovskite) | $a = b = c = 3.95 \text{ \AA}$ | $a = b = c = 3.99 \text{ \AA}$ |
| MgO (Rocksalt) | $a = b = c = 4.21 \text{ \AA}$ | $a = b = c = 4.21 \text{ \AA}$ |
| CaO (Rocksalt) | $a = b = c = 4.73 \text{ \AA}$ | $a = b = c = 4.81 \text{ \AA}$ |
| BaO (Rocksalt) | $a = b = c = 5.49 \text{ \AA}$ | $a = b = c = 5.54 \text{ \AA}$ |

4.3 Geometric Modeling of Nanopolycrystals

This research attempts to generate nanopolycrystalline "samples" with a structure reasonably similar to the structures observed experimentally. There are two parts in general:

grain and grain boundaries. For instance, the grains can be produced using a Voronoi construction: a set of grain centers are chosen randomly, and the part of space closer to a given center than to any other center is filled with atoms in a randomly rotated orientation. In the grain boundaries thus generated, it is possible that two atoms from two different grains get too close to each other, in such cases one of the atoms is removed to prevent unphysically large energies and forces as the simulation is started. Or, a gap can be produced between grains and can be filled with amorphous phase atoms. To obtain more relaxed grain boundaries, the constructed system is usually treated with an annealing process, followed by an energy minimization. This procedure is important to allow unfavorable local atomic configurations to relax.

A similar generation procedure has been reported by Chen [116], by D'Agostino and Van Swygenhoven [117], and by Van Swygenhoven and Caro [118,119]. A different approach was proposed by Phillpot, Wolf and Gleiter [120,121]: a nanocrystalline metal is generated by a computer simulation where a liquid is solidified in the presence of crystal nuclei, i.e. small spheres of atoms held fixed in crystalline positions. The system was then quenched, and the liquid crystallized around the seeds, thus creating a nanocrystalline metal. In the reported simulations, the positions and orientations of the seeds were deterministically chosen to produce eight grains of equal size and with known grain boundaries, but the method can naturally be modified to allow randomly placed and oriented seeds.

4.3.1 Generating Crystalline Grains

Two algorithms are adopted in this research to generate the geometric structure for polycrystalline material models. The first algorithm follows the Voronoi construction, which partitions the space to a configuration known as Voronoi tessellation. The second algorithm resembles the grain nucleation process, in which the domain of each grain is claimed through the process of wrapping atoms around each seed (grain point).

4.3.1.1 Voronoi Method

Voronoi tessellation is a way to divide the space into a number of regions [122]. A set of points (called seeds) are specified beforehand and for each seed there will be a corresponding region consisting of all points closer to that seed than to any other. These regions are called Voronoi cells. Figure 4-4 gives an example of the seeds and Voronoi cells in a 2D diagram.

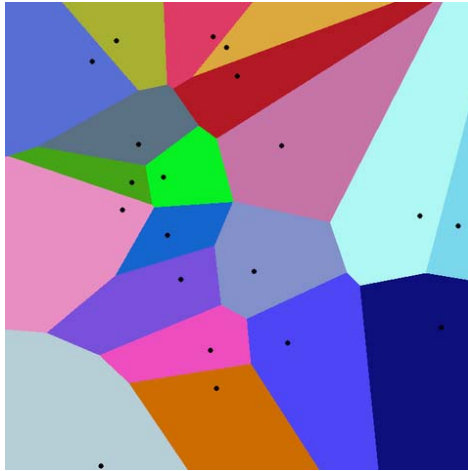


Figure 4-4: A 2D Voronoi diagram with 20 seeds and associated cells

In the generation of grains, the positions of the seeds can be determined by random number generators. For each seed, the corresponding Voronoi cell consists of all points closer to that seed than to any other. Then, each Voronoi cell is assigned with a crystallite, within which atoms are repeatedly arranged, as illustrated in Figure 4-5. Figure 4-6 shows a nanopolycrystalline cubic block of 1.6 million atoms, with the size $480 \times 480 \times 480$ A.U. length³, as obtained by this method.

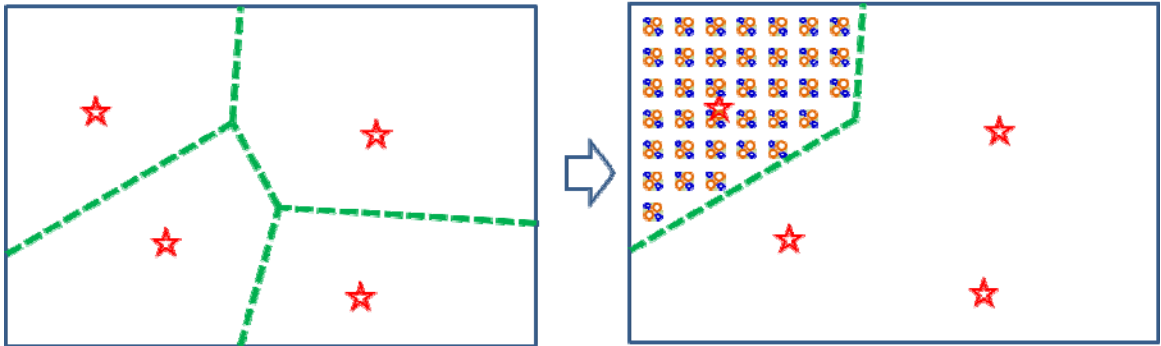


Figure 4-5: The schematic arrangement of atoms by Voronoi method (Left picture shows the grain partition, right picture shows the filling of the first grain)

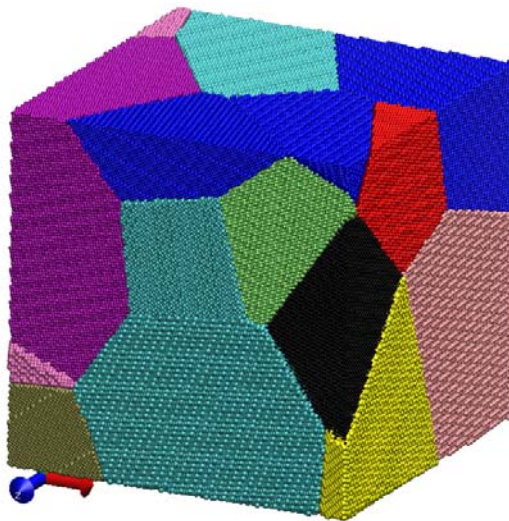


Figure 4-6: Nano-polycrystalline block of 1.6 million atoms generated using Voronoi method

4.3.1.2 Grain Nucleation Method

Grain nucleation is a phenomenal feature in polycrystalline materials such as metals and most ceramics. The natural process of grain nucleation and growth involves localized budding and increasing in size in a grain. This research tries to mimic the natural process of grain nucleation to determine the arrangement of polycrystals.

In the grain nucleation method, like Voronoi method, the positions of a set of seeds are determined by random number generators. For each seed, a specific crystallite, with random selection of species and random orientation, is assigned. Then atoms are placed to wrap around the seed, i.e. layer by layer outwards from the seeds. But for each grain, not all atoms are placed around the seed at one shot. In contrast, only one layer of atoms are placed around a seed each time, and then another layer of atoms are placed around the next seed, rather than the first seed. As this process goes on, whenever it is found that the atom to be placed is too close to an existing atom, this atom is skipped. This iteration is performed until the whole space is filled up. Figure 4-7 illustrates this construction.

Figure 4-8 shows a nanopolycrystalline cubic block of 0.33 million atoms, with size $300*300*300$ A.U. length³, as obtained by this method.

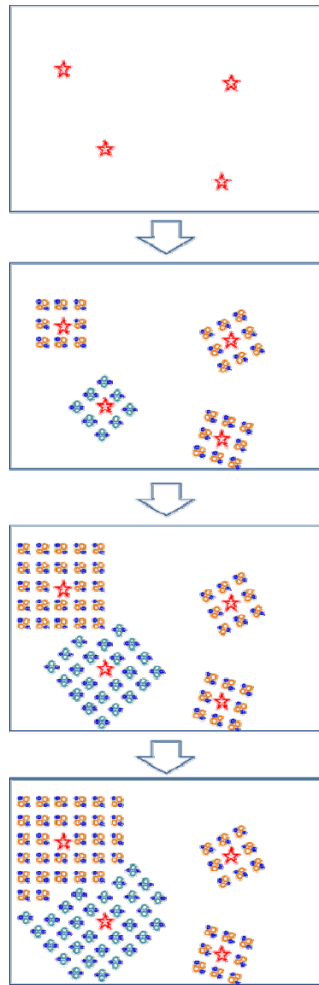


Figure 4-7: The schematic arrangement of atoms by grain nucleation method

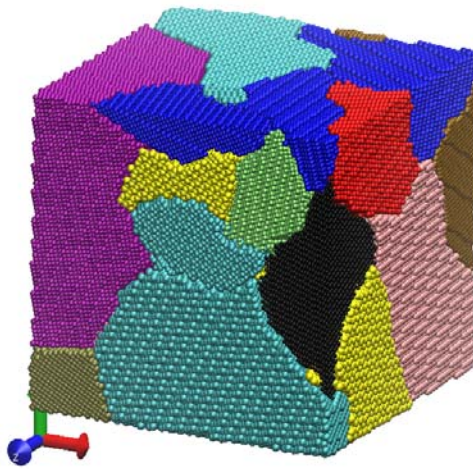


Figure 4-8: Nanopolycrystalline block of 0.33 million atoms generated using grain nucleation method

4.3.2 Grain Orientation and Euler Angles

As aforementioned, crystalline orientation is an important structural peculiarity and thus should be incorporated into the structural modeling. In this research, Euler angles are adopted to set the crystalline orientations of the grains. The Euler angles are three angles introduced by Leonhard Euler to describe the orientation of a rigid body [123]. To describe such an orientation in 3-dimensional Euclidean space three parameters are required. Euler angles are also used to describe the orientation of a frame of reference relative to another.

Euler angles represent a sequence of three elemental rotations. A common way to achieve the an orientation is composed by three steps: (1) a first rotation about z by an angle ϕ ,

(2) a second rotation about N (the intermediate x , or the line of nodes) by an angle θ , and (3) a last rotation again about Z (the intermediate z) by an angle ψ . These three steps and three Euler angles are shown in Figure 4-9. The transformation matrix \mathbf{A} can be obtained as the triple product of three separate rotations \mathbf{B} , \mathbf{C} , \mathbf{D} :

$$\mathbf{A} = \mathbf{BCD} \quad (4.4)$$

where each rotation has a relatively simple matrix form.

The \mathbf{D} transformation is a rotation about z axis, hence has a matrix of the form:

$$\mathbf{D} = \begin{bmatrix} \cos \phi & \sin \phi & 0 \\ -\sin \phi & \cos \phi & 0 \\ 0 & 0 & 1 \end{bmatrix} \quad (4.5)$$

The \mathbf{C} transformation corresponds to a rotation about N , which is the line of nodes, with the matrix:

$$\mathbf{C} = \begin{bmatrix} 1 & 0 & 0 \\ 0 & \cos \theta & \sin \theta \\ 0 & -\sin \theta & \cos \theta \end{bmatrix} \quad (4.6)$$

and finally \mathbf{B} is a rotation about Z and therefore has the same form as \mathbf{D} :

$$\mathbf{B} = \begin{bmatrix} \cos \psi & \sin \psi & 0 \\ -\sin \psi & \cos \psi & 0 \\ 0 & 0 & 1 \end{bmatrix} \quad (4.7)$$

The product matrix $\mathbf{A} = \mathbf{BCD}$ then follows as

$$\mathbf{A} = \begin{bmatrix} \cos \psi \cos \phi - \cos \theta \sin \phi \sin \psi & \cos \psi \sin \phi + \cos \theta \cos \phi \sin \psi & \sin \psi \sin \theta \\ -\sin \psi \cos \phi - \cos \theta \sin \phi \cos \psi & -\sin \psi \sin \theta + \cos \theta \cos \phi \cos \psi & \cos \psi \sin \theta \\ \sin \theta \sin \phi & -\sin \theta \cos \phi & \cos \theta \end{bmatrix} \quad (4.8)$$

After obtaining the transformation matrix \mathbf{A} , the transformation of a vector \mathbf{x} in 3-dimensional space can be obtained:

$$\mathbf{x}' = \mathbf{Ax} \quad (4.9)$$

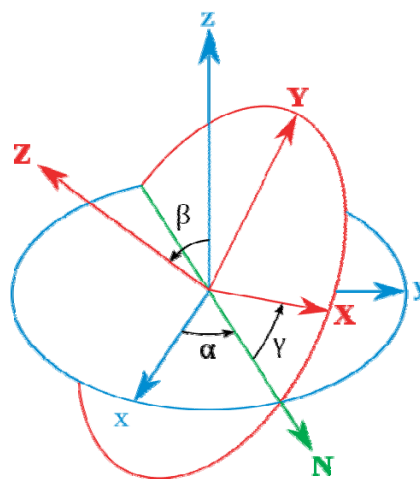


Figure 4-9: Proper Euler angles representing rotations about z, N, and Z axes. The xyz (original) system is shown in blue, the XYZ (rotated) system is shown in red. The line of nodes (N) is shown in green.

It is seen that the transformation matrix is determined by three angles ϕ, ψ, θ . To generate an arbitrary orientation of a grain, random number generators are used to produce a set of values for ϕ, ψ, θ and calculate the corresponding transformation matrix. Finally, the three primitive translation vectors of the crystallites can be transformed according to which atoms can be placed.

4.3.3 Generating Amorphous Grain Boundaries

Simulated amorphous structures can be prepared computationally in the same way as real glasses are produced. Models of crystalline systems are melted and the melts turn into a disordered amorphous phase. The biggest challenge here is in the time scale: compared to the melting and more particularly the quench occurring in nature, current computational capabilities can only achieve the process with several orders of magnitude greater than the rates achieved experimentally. As a consequence, simulated amorphous structures may have very high fictive residue stress. Therefore, a long time relaxation treatment is mandated to achieve a low stress level specimen, which is still a challenge in MD simulations of nanopolycrystalline solids.

4.3.4 Combining Grains and Grain Boundaries

In the aforementioned approach in generating grains, a controllable space or gap can be produced between any two grains. Grains and grain boundaries can be combined simply by Boolean operation, which includes union, intersection and difference. The Boolean operation performs the union of grains and gain boundaries, followed by subtracting their intersection.

4.4 Characterization of Nanopolycrystals

4.4.1 Characterizing Indices

Following the idea of OIMD, a characterizing index needs to be objective to be qualified to present the real-time characteristics of an atom or the region during the simulation. The following is a list of objectivity-proved characterizing indices:

- 1) Potential energy
- 2) Force (interatomic force)
- 3) Centrosymmetric parameter
- 4) Coordinate number

5) Von-Mises stress

6) Temperature

7) Displacement

8) Polarization

4.4.2 Examples

The generated nanostructure can be visualized in different MD analysis and visualization software, such as VMD and AtomEye. Quantities of interest can be displayed via isometric view, orthographic view, section view, etc. Ensemble properties as well as distribution of individual atom properties can provide insightful information about the simulation. Figure 4-10 shows a series of section views of the polycrystal of a block of 15 grains. Figure 4-11 shows its isometric view. Figure 4-12 shows several instantaneous physical quantities in the polycrystals.

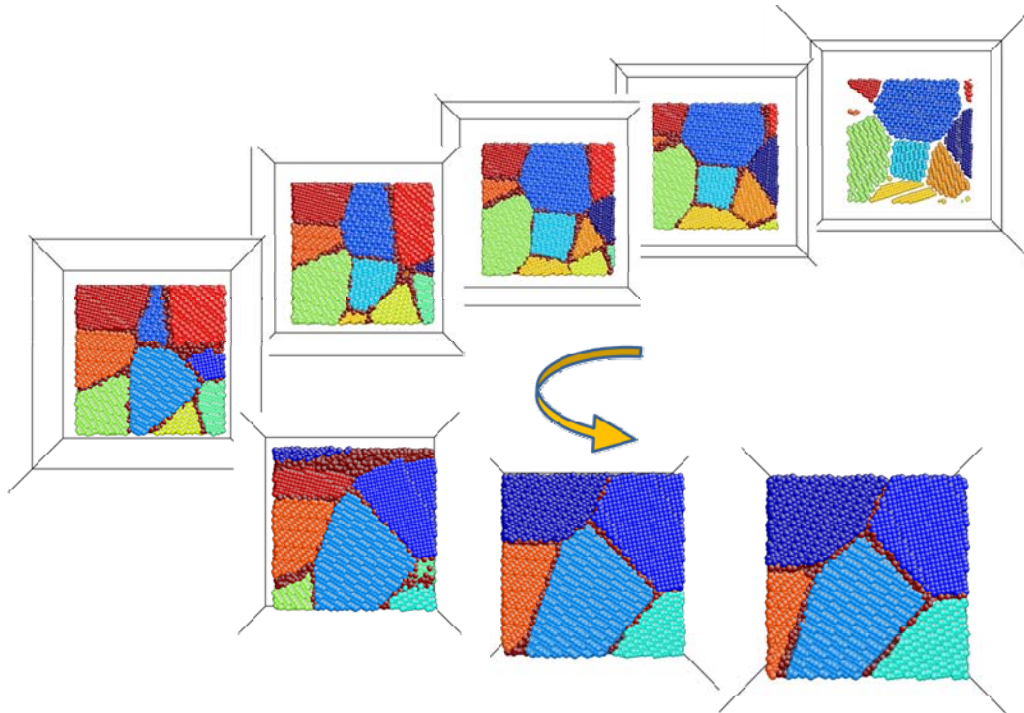


Figure 4-10: A series of section view from back to front of a block of polycrystal

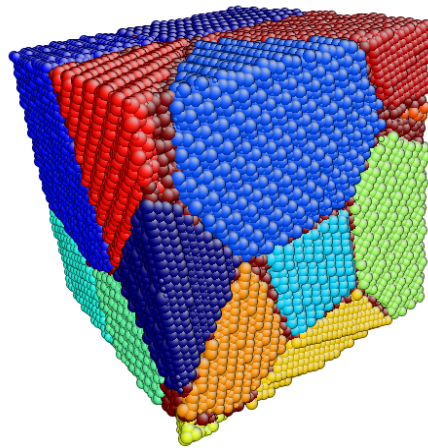
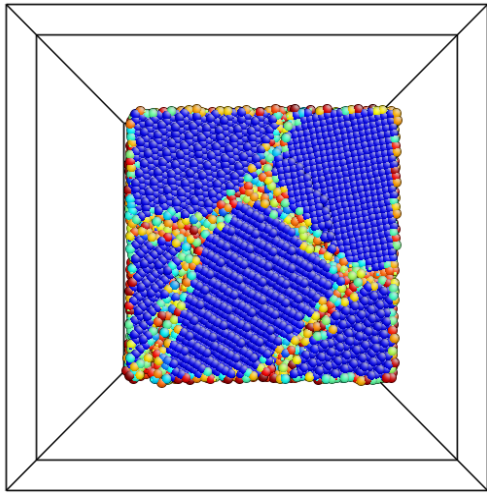
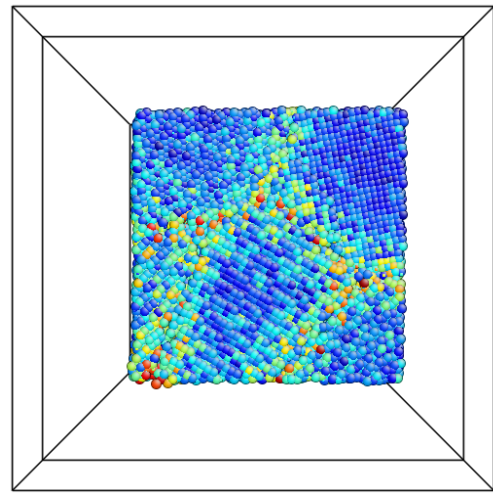


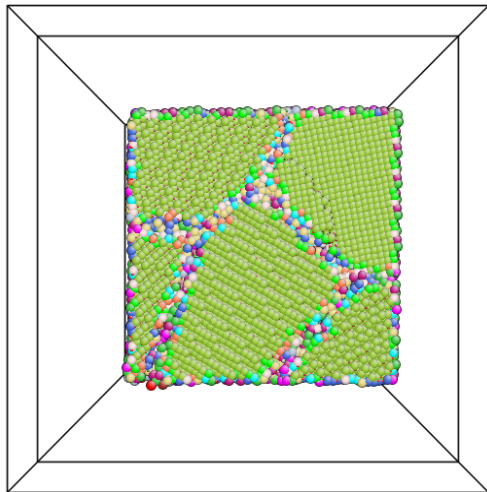
Figure 4-11: Configuration of a 15 grain polycrystal



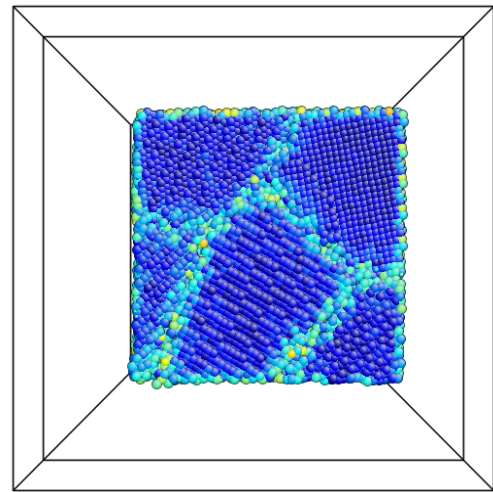
(a)



(b)



(c)



(d)

Figure 4-12: (a) Centrosymmetric parameter (b) Resultant force (c) Coordination number (d) Von Mises stress (based on Virial stress)

4.5 Summary

This chapter presents the framework to generate realistic while controllable nanopolycrystalline material models. Through the energy minimization based structural optimization study, realistic crystal structures are reproduced, which are in agreement with experimental results. This serves as the starting point of the configuration modeling of nanopolycrystalline solids. Then, two schemes are used to generate the geometric model of grains. Between the Voronoi method and the grain nucleation method, the grain nucleation method may give a model more closely to the naturally occurring multi-grain nanostructure, compared to Voronoi method, which can only produce convex polygon grains. To control the orientations of grains, Euler angles are used. As for grain boundaries, amorphous phase atoms are firstly obtained via amorphization process, and then filled to the gap between grains. Once the models are built, visualization tools and characterization indices can be employed to evaluate the sample nanopolycrystals.

CHAPTER 5: SIMULATED BEHAVIORS OF NANOPOLYCRYSTALS

In the previous chapters, a complete framework has been established to model and simulate nanopolycrystalline solids. In this chapter, the task is to demonstrate that the devised method is capable of solving different problems for the supposed material systems. In particular, applications to study the mechanical property, thermal property, electrical property and magnetic property of nanopolycrystalline materials are to be demonstrated. A computer program, called POLY (c.f. APPENDIX - III), has been developed for the purpose of computational simulation.

5.1 Mechanical Behaviors

5.1.1 Simple Tests on Single Nanocrystalline Solids

Before starting to simulate the mechanical behaviors of complex nanopolycrystalline solids, simple tests on single nanocrystalline solids are performed. Here the term “simple tests” refers to simple tension, simple compression and simple shear, which are considered as basic mechanical tests for engineering materials.

In this study, a single crystalline MgO specimen, consisting of 8232 atoms, is subjected to tension loading, compressive loading or shear loading, with the displacement specified boundary conditions being applied at the two ends of the specimen, as illustrated in Figure 5-1. The displacement controlled loading is applied according to Figure 5-2, which is divided into three stages: (i) a relaxation stage in which damping is used to damp out all the kinetic energy of the system, (ii) a loading stage in which the displacement is linearly increasing with time, and (iii) a holding stage in which the displacement is kept as a constant.

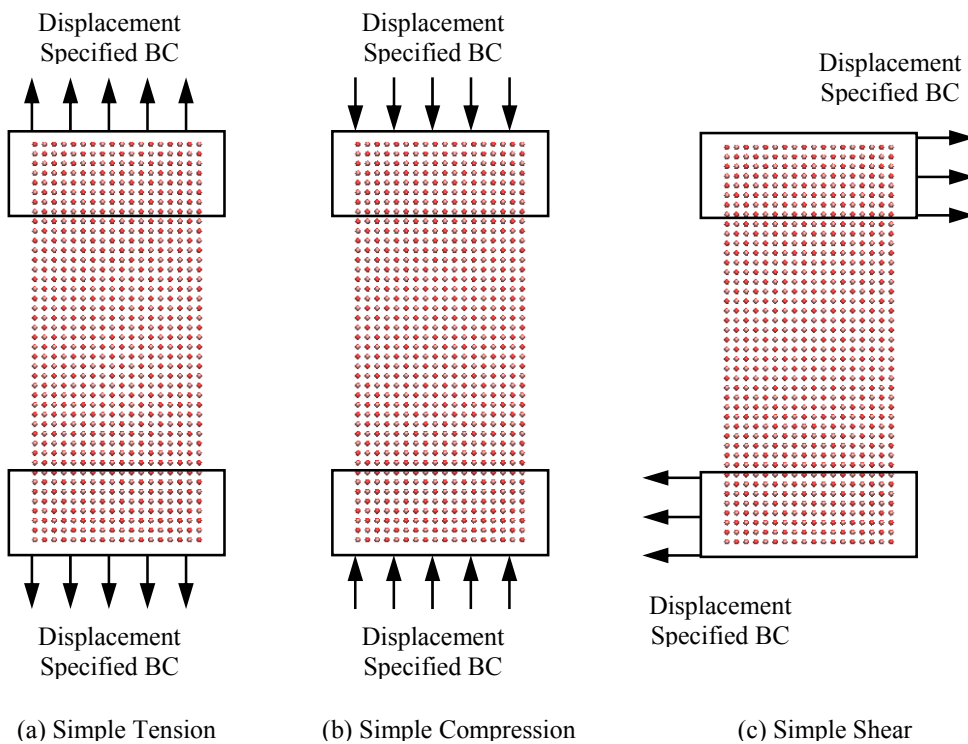


Figure 5-1: Schematic drawing of the specimen with three types of mechanical loadings.

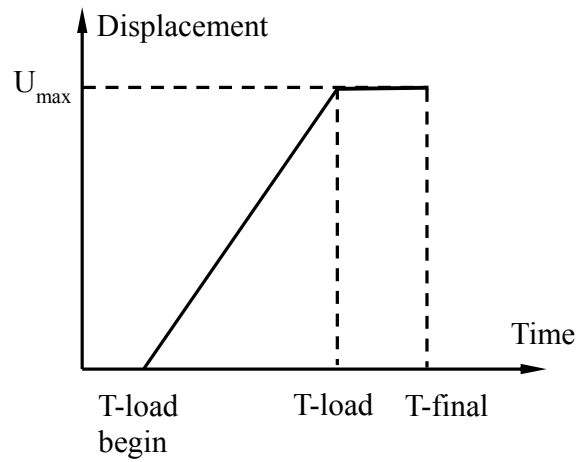


Figure 5-2: The loading history of the displacement specified boundary condition

In each simulation there are 160,000 time steps in total with $\Delta t = 30$ (a.u.). A maximum strain of 28% is applied to evaluate the material response, which covers from the linear response region to failure. The simulation results are presented and discussed below.

5.1.1.1 Simple Tension

For the simple tension test, Figure 5-3 shows the structural evolution during the linearly increasing loading stage and during the constant loading (holding) stage. The first snapshot shows that initial dislocations were developed around the middle plane of the specimen. The development of dislocation plane results in a noticeable crystal lattice transformation from an fcc structure to a hexagonal structure. This transformation leads to crystal structure relaxation/reconfiguration, which spreads throughout the whole specimen except the boundaries, as shown in the second snapshot in Figure 5-3. The dislocation necking was developed as the strain keeping increasing and finally the specimen fractured into two parts.

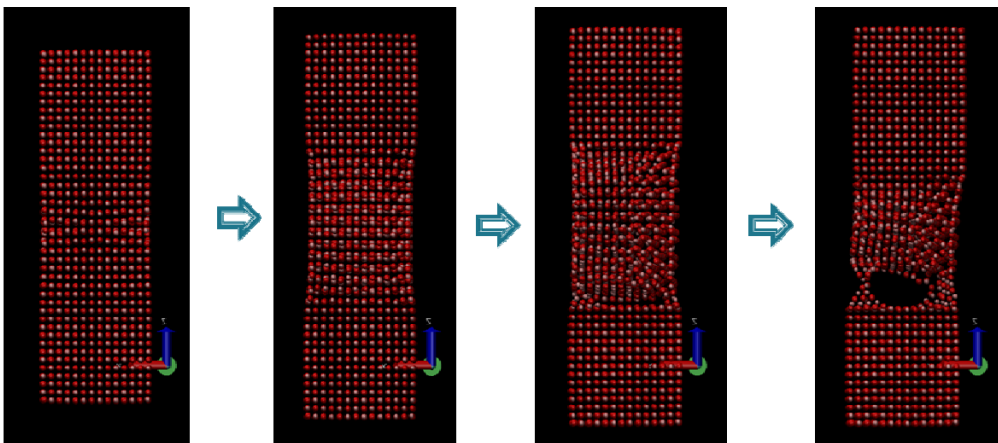


Figure 5-3: Structural evolution of MgO specimen under tensile loading.

The resultant forces acting on the two boundaries are recorded. Figure 5-4 shows the history of force (z-component, which is along the loading direction). With the information of the loading history, Figure 5-4 can be converted to a force-displacement relation, and further a stress-strain relation. The calculated value of young's modulus from the linear portion of the stress-strain curve is about 370 GPa, which is in good agreement with the experimental data, 270 ~ 330 GPa [124,125].

As aforementioned, stress at atomic level can also be evaluated via virial stress, which is often linked to macroscopic "Cauchy stress" or "engineering stress". Here, the virial stress is averaged over the center part of the specimen, as displayed in Figure 5-5. The comparison between Figure 5-4 and Figure 5-5 shows that the profiles of the force and the virial stress are very close to each other. In particular, the stress increases linearly with time at the loading stage to reach the maximum tensile stress. After reaching this critical stress, the stress drops, which corresponds to the fact that the material loses its stability and it yields. The recorded virial stress shows a great agreement with the engineering stress (force over area) in terms of the shape of the curve. The value of young's modulus calculated by virial stress is about 70 GPa. This value is close to the range of the experimental result but is much lower than the result obtained by engineering stress. Therefore, further quantitative study is needed to validate the equivalence of virial stress and engineering.

Ultimate strengths obtained by the engineering stress approach and the virial stress approach are 18.5 GPa and 3.6 GPa, respectively, both of which are much higher than the

experimental data of the bulk MgO: 166.7 MPa [124,125], but they are in agreement with the reported MD simulation results: 7.0 ~ 13.0 GPa [126].

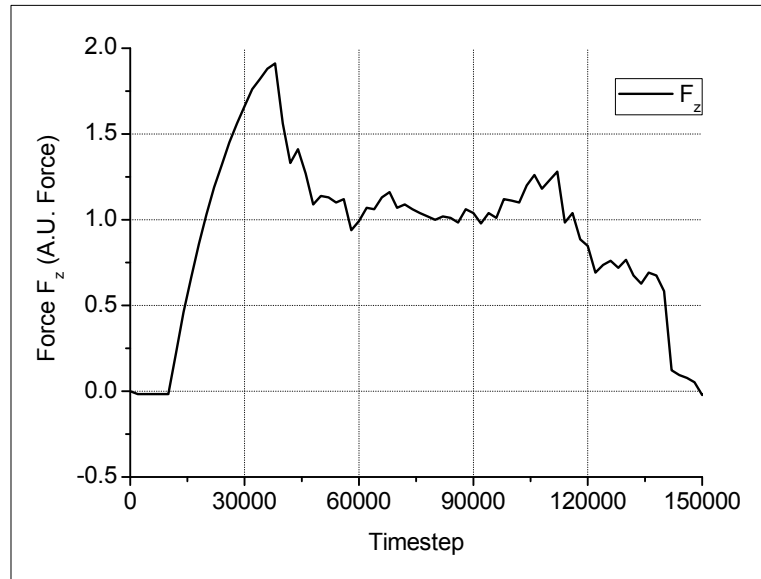


Figure 5-4: History of the boundary force of the MgO specimen under tensile loading

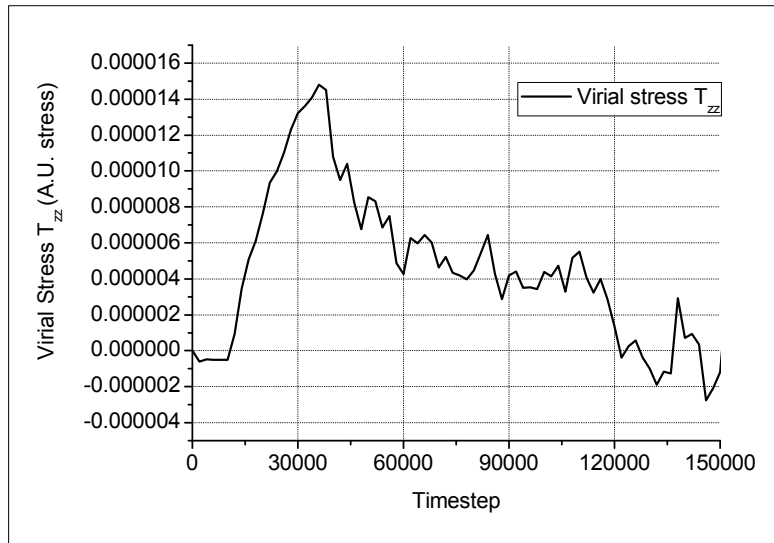


Figure 5-5: History of T_{33} component of the virial stress, averaged over the center part of the MgO specimen under tensile loading.

5.1.1.2 Simple Compression

For simple compression test, Figure 5-6 shows the structural evolution during the linearly increasing loading stage and during the constant loading (holding) stage; Figure 5-7 shows the history of the force (z-component, which is along the loading direction); Figure 5-8 shows the calculated virial stress averaged over the center part of the specimen. It is seen that the stress increases (compressive stress is negative, “increase” refers to its magnitude) with the time at the loading stage to reach the maximum compressive stress. Then

dislocations were initiated and the stress drops. With continuous compressive loading, the stress climbs again and drops again, till the end of the simulation.

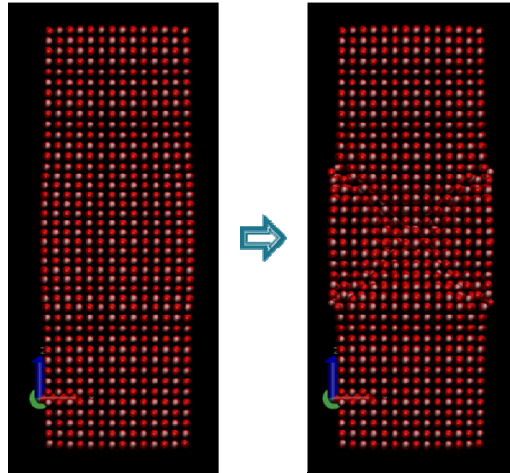


Figure 5-6: Structural evolution of MgO specimen under compressive loading

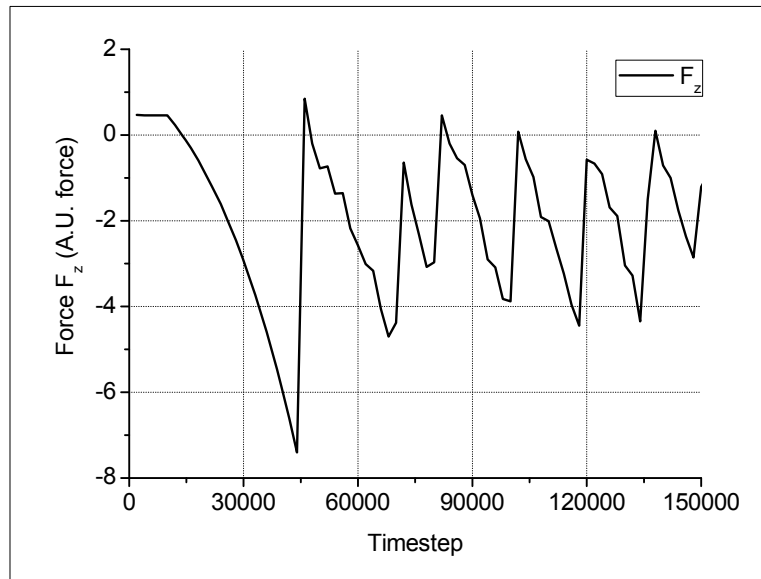


Figure 5-7: History of the boundary force of the MgO specimen under compressive loading

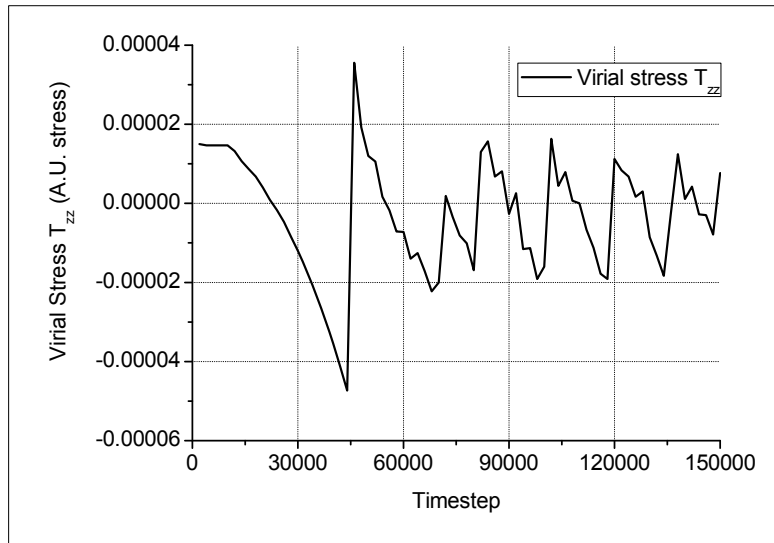


Figure 5-8: History of T_{33} component of the virial stress, averaged over the center part of the MgO specimen under compressive loading.

Like the previous study of simple tension test, it is observed that there is a great agreement between the engineering stress and the virial stress in terms of the shape of the stress-strain curve. The maximum compressive strengths obtained by the engineering stress approach and the virial stress approach are 72 GPa and 11.3 GPa, respectively. These results are much higher than the experimental result of the bulk MgO: 1666.6 MPa [124,125]. It is noticed that the calculated maximum compressive stress is larger than the maximum tensile

stress as found in the simple tension simulation. Therefore they are consistent with the previous cases thus considered as reasonable.

5.1.1.3 Simple Shear

For simple shear test, Figure 5-9 shows the structural evolution during the linearly increasing loading stage and during the constant loading (holding) stage. It is seen that dislocations initiate near the boundaries as well as in the diagonal plane across the specimen.

This time, to calculate the shear stress, the boundary force along x-direction, which is along the loading direction, is recorded, as shown in Figure 5-10; the T_{13} component of the virial stress is displayed in Figure 5-11. Again, it is observed that there is a great agreement between the engineering stress and the virial stress in terms of the shape of the stress-strain curve. It is seen that in both figures the shear stress (represented by force and T_{13} virial stress, respectively) rises with the time at the loading stage to reach the maximum shear stress, then collapses. Shear modulus is obtained: 159 GPa by engineering stress approach and 33 GPa by virial stress approach. The reported experimental data for bulk MgO is 92 ~ 122 GPa. Therefore, the simulation result is on the same order of magnitude as the experimental results thus considered reasonable.

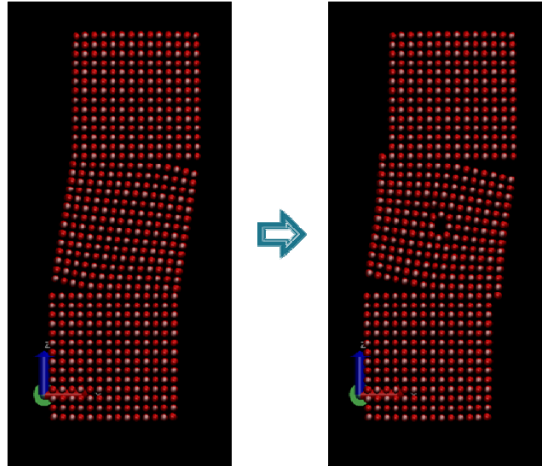


Figure 5-9: Structural evolution of MgO specimen under shear loading.

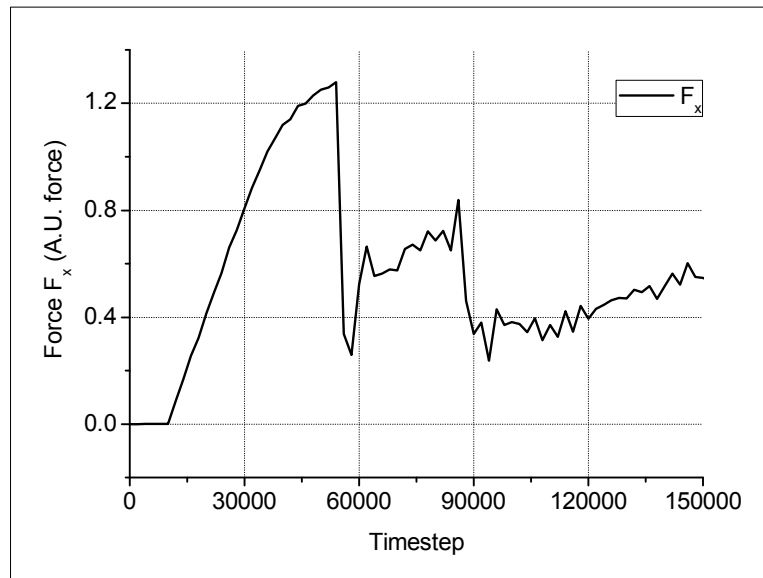


Figure 5-10: History of the boundary force of the MgO specimen under shear loading.

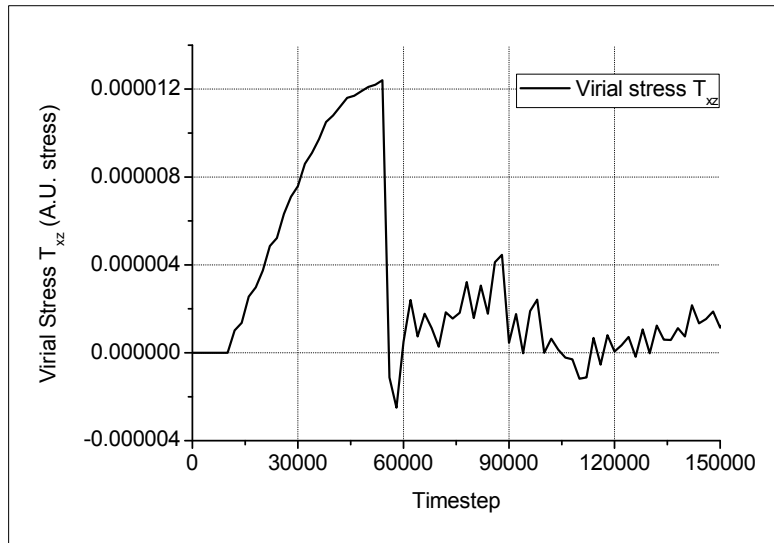


Figure 5-11: History of T_{13} component of the virial stress, averaged over the center part of the MgO specimen under shear loading.

5.1.2 Mechanical Loading on Nanopolycrystals

The material response of nanopolycrystals under mechanical loading is simulated in this study. The specimen is prepared as a slab of nanopolycrystalline, which consists of 44520 atoms. In the specimen there are 10 grains of MgO or CaO and grain boundaries of mixed MgO-CaO. A notch is made on the edge of the middle plane to test the material response. The specimen, as shown in Figure 5-15, has been through initial damped relaxation process to reach its equilibrium.

This specimen is subjected to displacement specified boundary conditions being applied at the two ends of the specimen. Like previous cases, the displacement controlled loading consists of three stages: (i) a relaxation stage in which damping is used to damp out all the kinetic energy of the system, (ii) a loading stage in which the displacement is linearly increasing with time, and (iii) a holding stage in which the displacement is kept as a constant.

There are 80,000 time steps in total with $\Delta t = 40$ (a.u.) . The maximum strain is 50%.

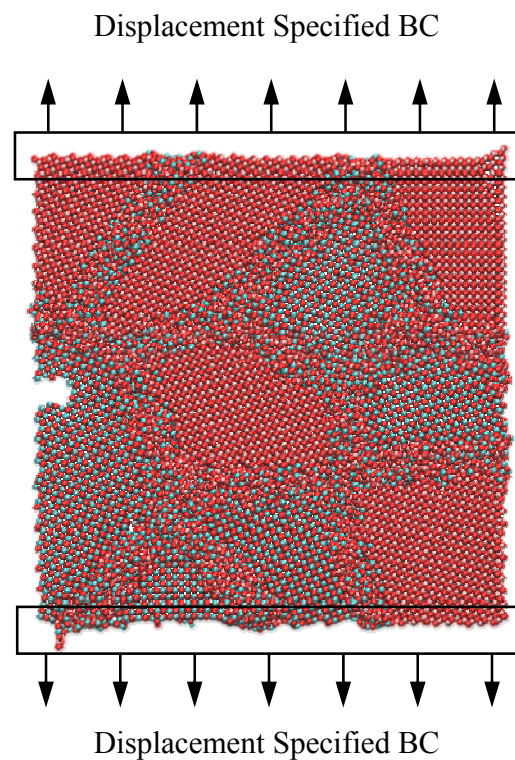


Figure 5-12: A nanopolycrystalline specimen, consisting of 10 grains, and the displacement specified boundary condition.

This setting is the same to a typical mode-I fracture mechanics problem. If the material is homogeneous and elastic, the tensile loading on the two sides of the specimen is expected to initiate a crack at the notch and the crack will propagate through the middle plane, in a direction perpendicular to the direction of the loading.

Figure 5-13 shows the structural evolution of the specimen. It turns out that no sharp crack is produced during the process. Rather, the material still fails in a way similar to tension test. In particular, the failure initiates from the region of amorphous grain boundaries and stays mostly within the grain boundaries, until the whole specimen is torn apart. This may be possibly explained by the highly concentrated stress in the grain boundaries. On the one hand, the grain boundary contains highly disordered atoms, which are far away from perfect crystal structure environment, so it is very likely that these atoms will suffer high stress. On the other hand, amorphous phase grain boundaries are obtained through amorphization process and residue stress is commonly seen in the resulting structure. An extremely long time of relaxation is necessary to reduce the residue stress to a very low level but it is computationally expensive. It is possible that the residue stress that comes from the structure model itself plays an important role in influencing the material response.

This interesting result provides an example about the unique properties of nanopolycrystalline solids.

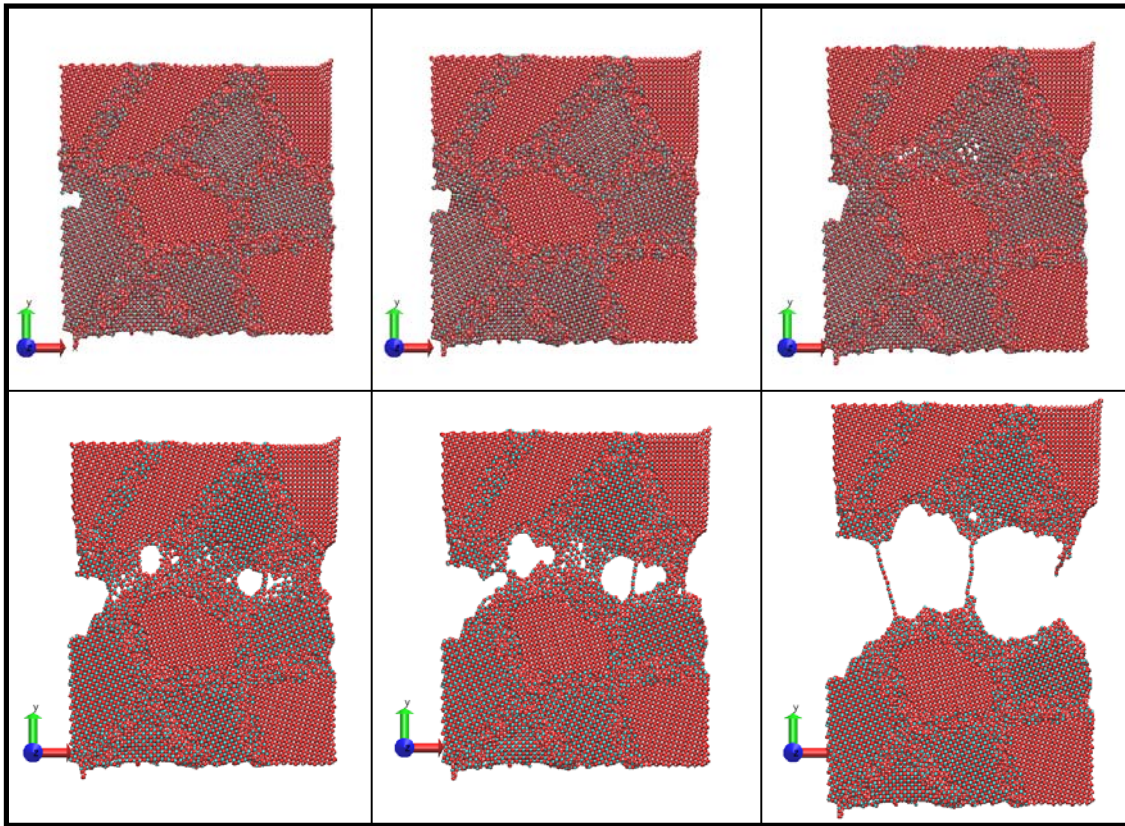


Figure 5-13: Structural evolution of nanopolycrystalline specimen
under mechanical loading

5.2 Thermal Behaviors

5.2.1 Thermal Behaviors with Uniform Heat Bath

In this study, the thermal behaviors of nanopolycrystalline materials with the effect of a uniform heat bath are investigated. Heat bath means temperature control, which is realized by upgraded Nose-Hoover thermostat algorithm.

5.2.1.1 Relaxation to Near Absolute Zero Temperature

After obtaining the nanopolycrystalline model as demonstrated in CHAPTER 4, the first treatment to the specimen is relaxation, which aims to reduce the highly concentrated stress at the imperfection sites. Figure 5-14 shows the specimen that are prepared for the thermal analysis, which consists of 15 grains, including MgO grains and CaO grains. There are 48928 atoms in total in the nanopolycrystal with a dimension of $160 \times 160 \times 160$ A.U. length³ and the mean grain size is 65 A.U. length. Figure 5-15 shows the specimen that have passed the relaxation process. Now the specimen is ready for thermal loadings.

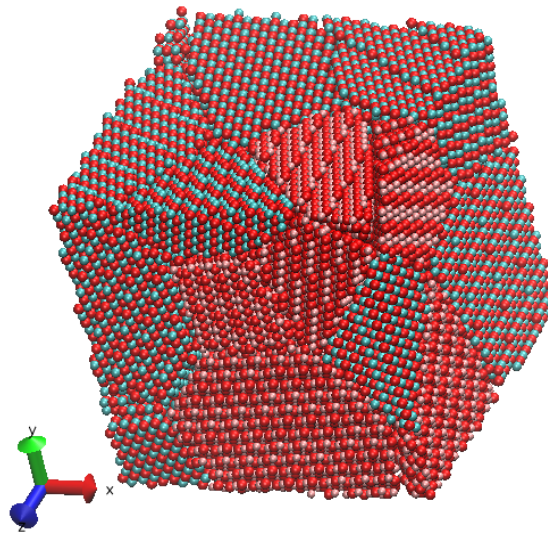


Figure 5-14: A nanopolycrystalline specimen of 15 grains (MgO + CaO). This figure shows the initial configuration (before relaxation).

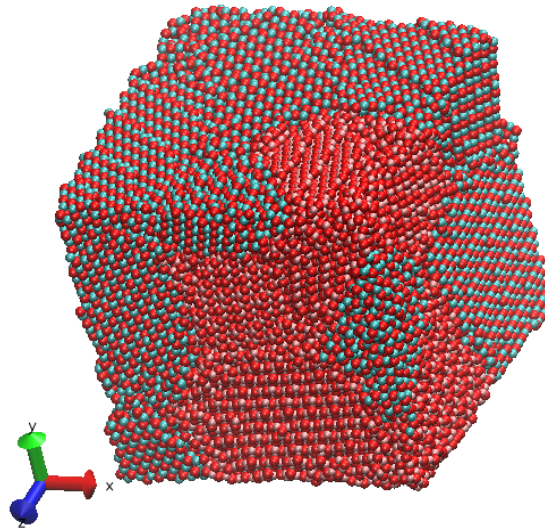


Figure 5-15: A nanopolycrystalline specimen of 15 grains (MgO + CaO). This figure shows the relaxed configuration (after damped relaxation). $T \approx 0$ K.

5.2.1.2 Heating

Based on the specimen prepared by the relaxation process, temperature loading is added via upgraded Nose-Hoover thermostat. The temperature control is applied in a similar way as the aforementioned mechanical loading, which is divided into three stages: (i) a flat stage in which the specimen is controlled at a constant low temperature, (ii) a heating stage in which the target temperature is linearly increasing with time, and (iii) a flat stage in which the specimen is kept at a constant high temperature.

In this initial heating process, the target temperature ends at 2,000 K. Figure 5-16 shows the temperature history that the specimen experiences. Figure 5-17 shows the specimen configuration by the end of the heating process. It is seen that, although the atoms vibrate fiercely, it can still be recognized that there are different grains, each of which maintains a crystalline internal structure. This result indicates that the nanopolycrystalline specimen is thermally stable at 2,000 K.

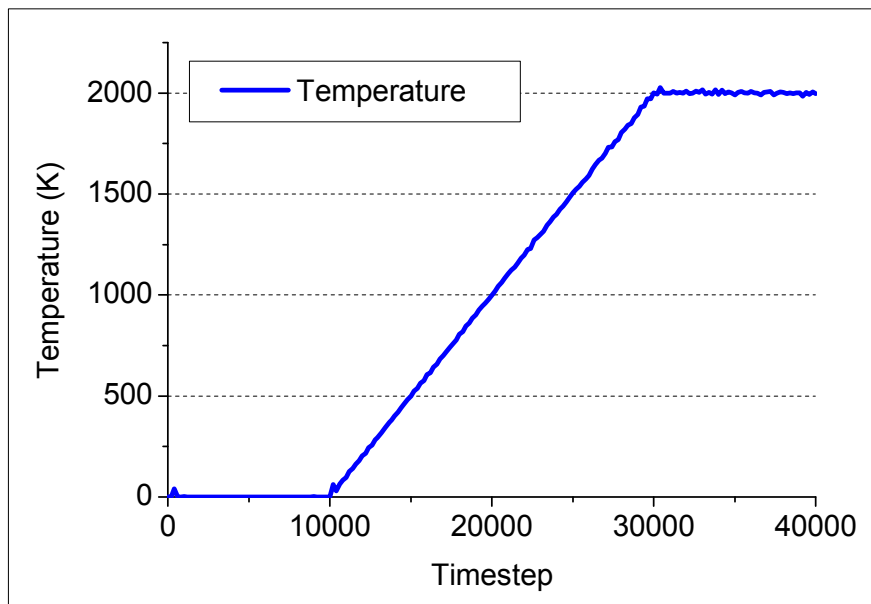


Figure 5-16: Temperature history of the nanopolycrystalline specimen during the heating process.

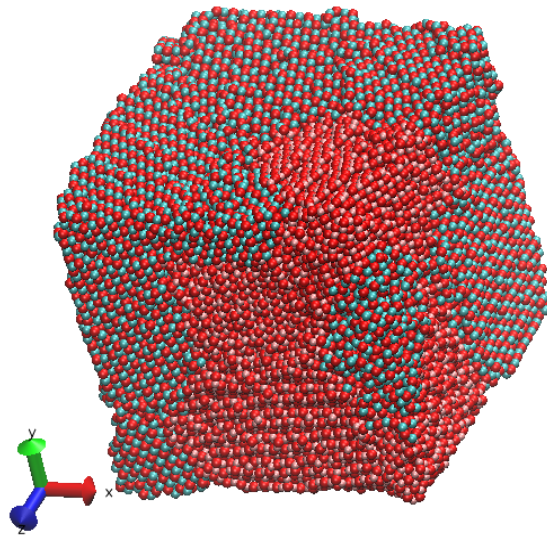


Figure 5-17: A nanopolycrystalline specimen of 15 grains (MgO + CaO). This figure shows the configuration when it is heated up to $T = 2,000$ K.

5.2.1.3 Melting

In this study, the specimen obtained in the last section is continued to be heated up from 2,000 K to 4,000 K and now the melting phenomenon is observed. The temperature history of the specimen is recorded as in Figure 5-18. When the temperature is about 3,000 K, the specimen can hardly hold its crystalline internal structure in each grain, as it is observed in Figure 5-19. Just a few hundred time steps after reaching 3,000 K, the specimen turns into amorphous phase and crystalline structure is no longer observed. Figure 5-20 shows the

chaotic state of the melted specimen at 4,000 K. The bulk configuration of the melted specimen loses its original cubic shape and is now in liquid state. Therefore, the simulation result records the melting point of the MgO-CaO mixed nanopolycrystalline specimen is about 3,000 K.

By looking up the material properties of Magnesium oxide and Calcium oxide [127], it is found that the melting point of bulk MgO is 3,125 K (2,852°C, 5,166°F), and the melting point of bulk CaO is 2,886 K (2613 °C, 4735 °F). It has been known in the scientific community that the melting temperature of a bulk material is not dependent on its size. However as the dimensions of a material decrease towards the atomic scale, the melting temperature scales with the material dimensions, which is referred as *melting-point depression* [128-130]. The decrease in melting temperature can be on the order of tens to hundreds of degrees for metals with nanometer dimensions. Therefore, it is anticipated that such a phenomenon may be observed on nanopolycrystalline materials. In this simulation, the recorded melting point of MgO-CaO nanopolycrystal is about 3,000 K, which is at about the same order of the reported melting points of the two substrates. The melting-point depression phenomenon is not apparently observed. Since the characteristics of the melting process depend on a variety of parameters such as size and shape of the particles, concentration of impurities, and presence of substrates, further study can be proposed to investigate into this intriguing process.

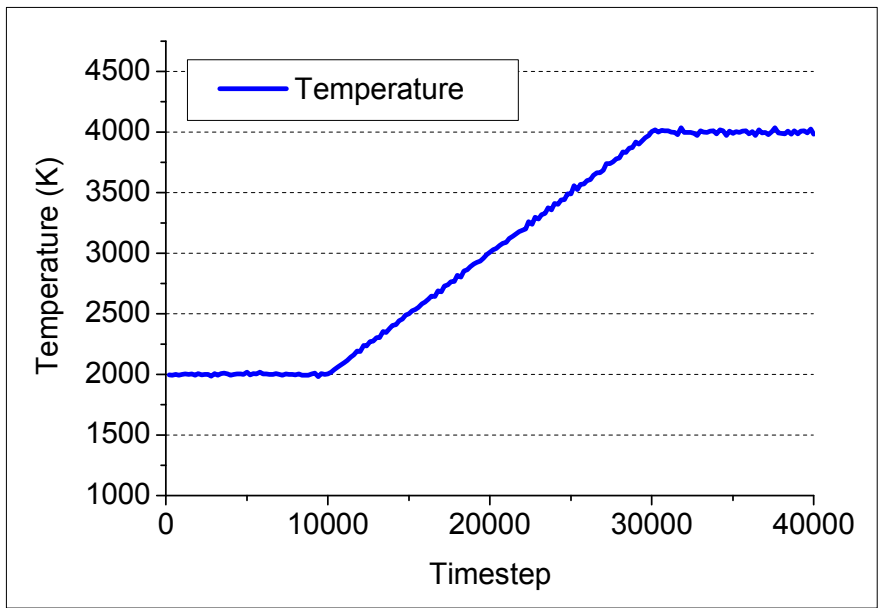


Figure 5-18: Temperature history of the nanopolycrystalline specimen during the continued heating process.

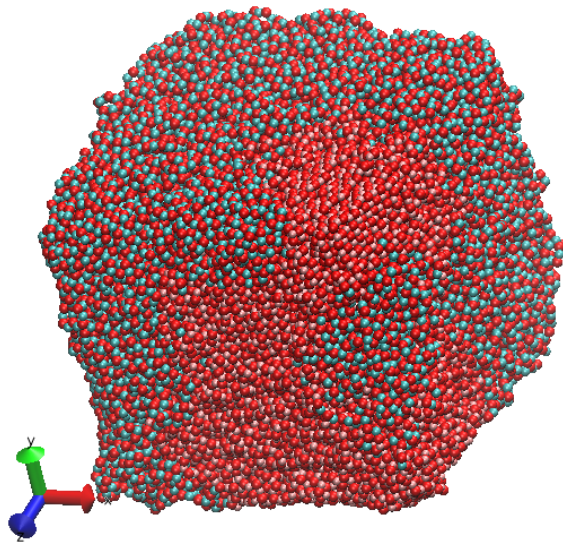


Figure 5-19: A nanopolycrystalline specimen of 15 grains (MgO + CaO). This figure shows the configuration at $T = 3,000$ K, which is a few moment before melting.

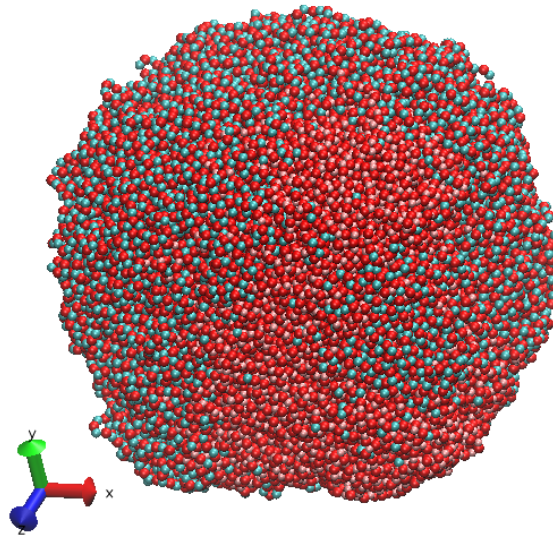


Figure 5-20: A nanopolycrystalline specimen (MgO + CaO). This figure shows the melted configuration at $T = 4,000$ K.

5.2.1.4 Cooling and Grain Growth

Cooling process is an interesting and important topic since it usually restores order. In this study, the cooling process is performed on a slab of nanopolycrystals with 6 grains, which take 2-dimensional Voronoi tessellation for its grains geometry. This model is chosen for the purpose of its simplicity in demonstration.

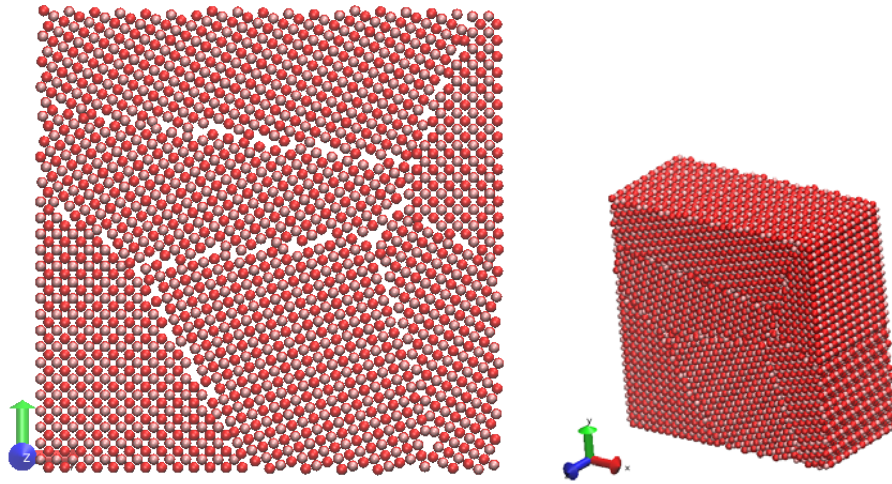


Figure 5-21: A slab of nanopolycrystals, with grains of 2-D Voronoi pattern. This figure shows the initial configuration.

This specimen is firstly heated up to 2,000 K, then cooled back to zero temperature, followed by long time relaxation. The configuration at 2,000 K is shown in Figure 5-22 and the final configuration after cooling and relaxation is shown in Figure 5-23.

It is seen that at a high temperature, while not melting, several grains start to deform and even merge together. After the cooling and relaxation process, the kinetic energy has been damped out and the structure reaches a stable state at a local energy minimum. It is observed that the original 6-grain nanopolycrystals is now 3-grain. This simulation successfully replicates the phenomenon of grain growth, which was also reported in many other researchers (Xiao et al, 2006).

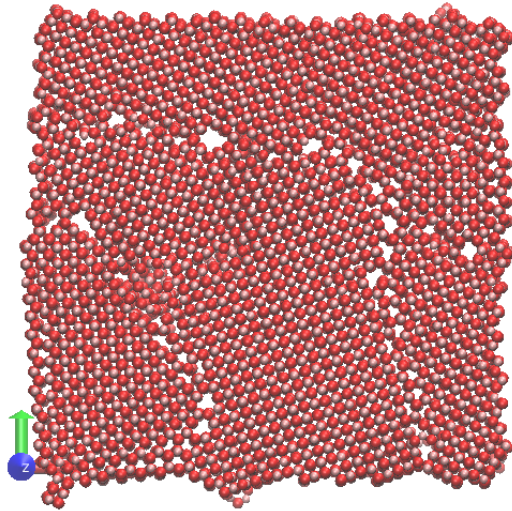


Figure 5-22: A slab of nanopolycrystals, with grains of 2-D Voronoi pattern. This figure shows the configuration at $T = 2,000$ K.

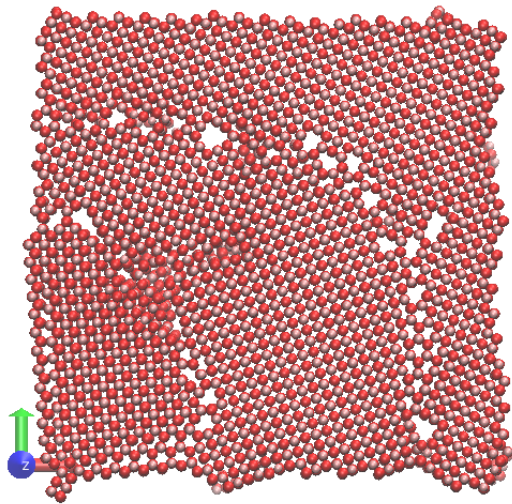


Figure 5-23: A slab of nanopolycrystals, with grains of 2-D Voronoi pattern. This figure shows the final configuration after cooling process.

5.2.2 Heat Conduction

In this study, heat conduction is demonstrated on polycrystalline materials. Compared to the uniform heat bath, heat conduction simulation involves distributed heat sources or heat sinks, which can also be implemented by upgraded Nose-Hoover thermostat. Figure 5-24 shows the configuration of the nanopolycrystalline slab, which consists of grains of MgO and CaO and grain boundaries of mixed MgO-CaO. The specimen is divided into 16 groups.

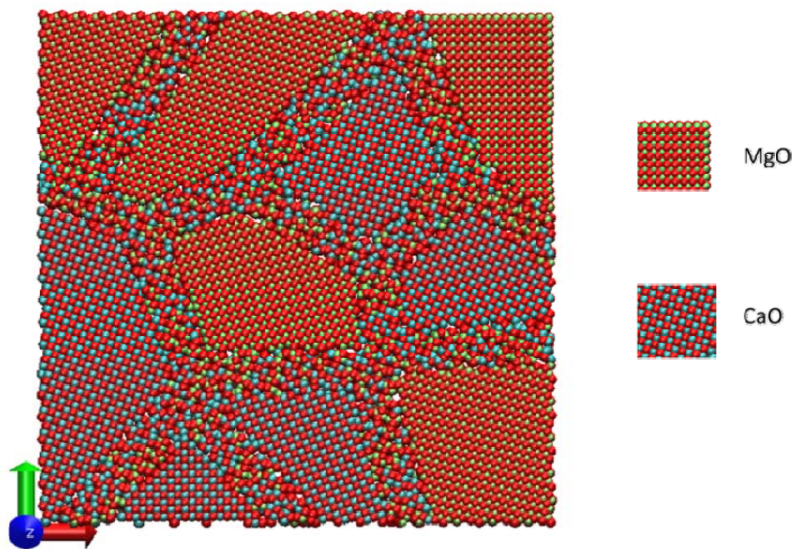


Figure 5-24: A slab of nanopolycrystalline specimen consisting of MgO and CaO.

1) Heat Conduction Case 1

In the first case of heat conduction, the thermostat controls temperature at the left side (groups 1 – 4) and right side (groups 13 – 16), as shown in Figure 5-25.

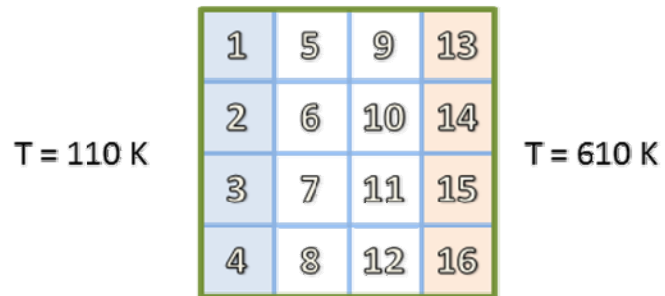


Figure 5-25: Schematics of distributed temperatures control – heat conduction case-1

After a long time simulation, a temperature gradient is produced between the left and right side, as shown in Figure 5-26. The temperature history of all 16 groups is shown in Figure 5-27.

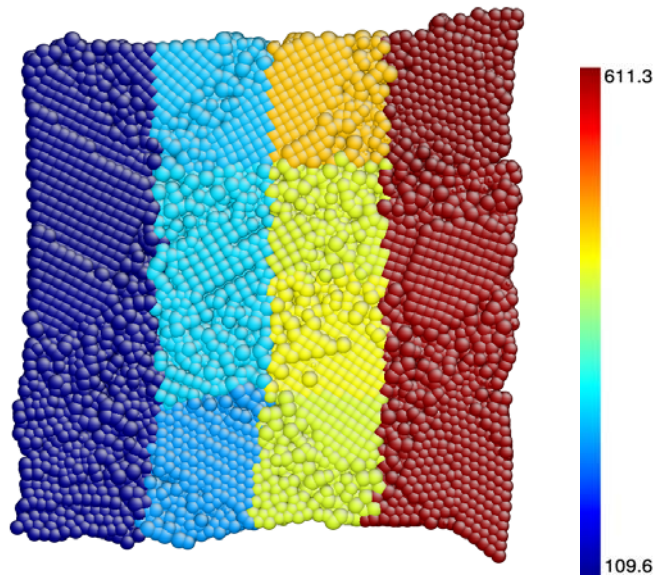


Figure 5-26: Temperature distribution after a long time simulation –
Heat conduction case-1

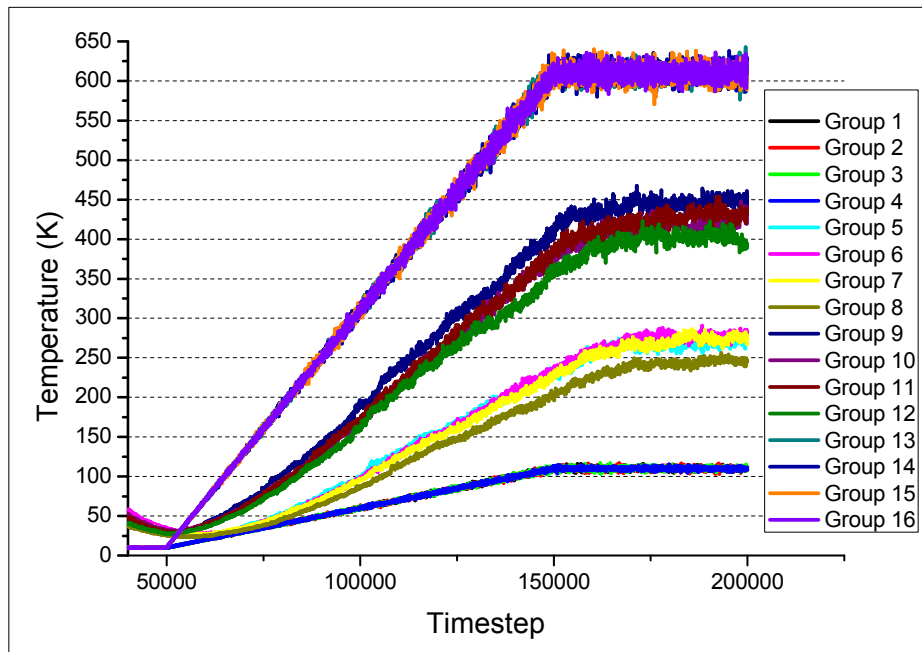


Figure 5-27: Temperature history by groups – Heat conduction case-1

2) Heat Conduction Case 2

In the second case of heat conduction, the thermostat controls temperature at the upper left corner (groups 1) and lower right corner (groups 16), as shown in Figure 5-28.

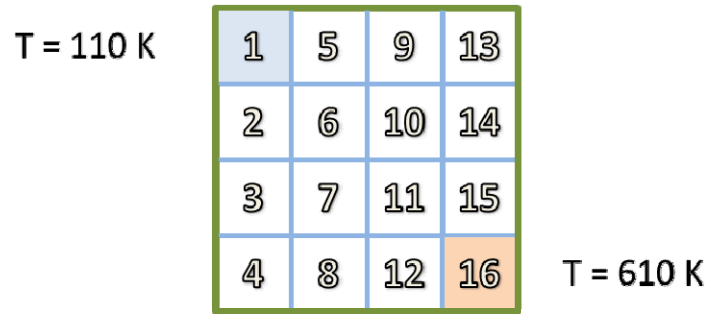


Figure 5-28: Schematics of distributed temperature control – heat conduction case-2

After a long time simulation, a temperature gradient is produced between the upper left corner and lower right corner, as shown in Figure 5-29.

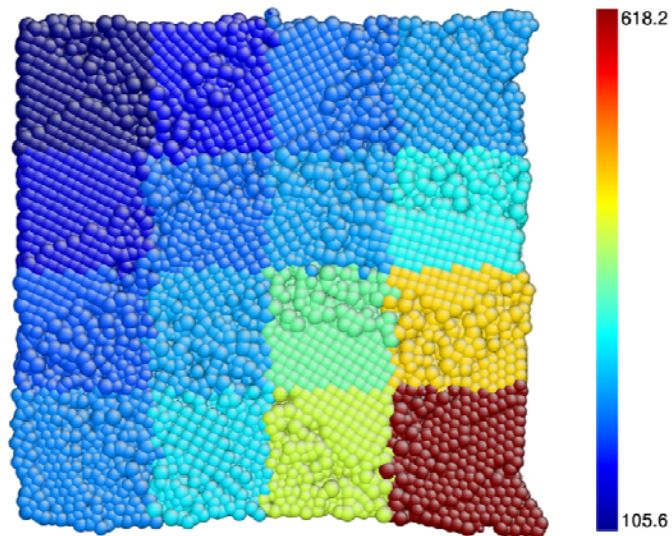


Figure 5-29: Temperature distribution after a long time simulation – Heat conduction case-2

Both case 1 and case 2 demonstrate that a clear monotonic temperature gradient is produced with the distributed temperature control, in which two ends of the specimen are controlled at low and high temperature, respectively. This result is consistent with Fourier's law. It is also noted that the temperature gradient is not uniform throughout the specimen, which means the thermal conductivity varies across the space and reflects the inhomogeneity of nanopolycrystals.

Although this simulation studies a hypothetical problem of heat conduction, which is artificial because it is physically unlikely to have such a large temperature difference between regions just a few nanometers away, it has a significant meaning in theory and technique that local temperature control can now be realized in NEMD. Furthermore, the observed physical process is consistent with key physical laws phenomenologically. Therefore, future quantitative analysis of the material properties of nanopolycrystalline solids can be performed and a deeper understanding may be obtained.

5.3 Electromagnetic Behaviors

Electromagnetic properties are of important value for many nanopolycrystalline materials, thus the EM field should be incorporated in the MD simulations. In this section, it is to demonstrate the validity of the MD theory with the aforementioned numerical schemes as introduced in CHAPTER 2. The investigations into the material responses under specific EM fields with specific applications are left to future research study.

5.3.1 Electric Effects

The effect of an external electrical field on the atomistic material system can be added to the MD simulation through the term $q\mathbf{E}$.

Some particular nanocrystalline solids have unique electrical properties and are of growing importance for a variety of recent and potential applications. These applications include piezoelectric transducers and actuators, non-volatile ferroelectric memories, dielectrics for microelectronics and wireless communication, pyroelectric arrays, and non-linear optical applications

For instance, a ferroelectric material exhibits a spontaneous polarization in a direction that can be switched by the application of an external electric field or stress. This phenomenon is a manifestation of the strong coupling between mechanical strain and electric field. One of the earliest technological applications of ferroelectric materials was in the area of electromechanical transducers, of which the physical basis is the piezoelectric effect. The piezoelectric coefficients characterize the linear change in polarization in the presence of an external stress, or equivalently, a change in shape under the application of an external electric field. In microelectromechanical systems applications, the piezoelectric/electrostrictive nature of ferroelectrics is utilized in the design of highly accurate microscopic sensors and actuators.

5.3.2 Magnetic Effects

5.3.2.1 Response to Magnetic Field at Zero Temperature

In the MD equations of motion with EM field, it is clear that the magnetic effect acts on the velocity of the atom through the cross product $\mathbf{v} \times \mathbf{B}$. At zero temperature, all atoms stand still and have no velocity. Thus it is straightforward to conclude that there is no effect by magnetic field when the temperature is at absolute zero. This is confirmed in our simulations.

5.3.2.2 Response to Magnetic Field at Non-Zero Temperature

At any non-zero temperature, atoms do move and are influenced by the magnetic field. In this work, it is worthwhile to discuss time integration methods that affect the validity and accuracy of simulations.

1) Using Velocity Verlet method

The Velocity Verlet method as given in Eq. (2.49) does not include \mathbf{v}^{n+1} in calculating \mathbf{a}^{n+1} . It is to be discussed here, if one prefers to use Velocity Verlet method and calculate \mathbf{a}^{n+1} based on \mathbf{x}^{n+1} and $\mathbf{v}^{n+\frac{1}{2}}$, one may observe some unphysical phenomena. These results may not be unique to nanopolycrystalline solids, but can also be seen in any MD simulation with the presence of EM field.

Two cases with different magnetic fields are studied here:

a) Case 1: $\mathbf{B} = (1, 0, 0)$

b) Case 2: $\mathbf{B} = (1, 1, 1)$

The histories of linear momentum and angular momentum of the material with $\mathbf{B} = (1, 0, 0)$ are shown in Figure 5-30 and Figure 5-31.

The histories of linear momentum and angular momentum of the material with $\mathbf{B} = (1, 1, 1)$ are shown in Figure 5-32 and Figure 5-33.

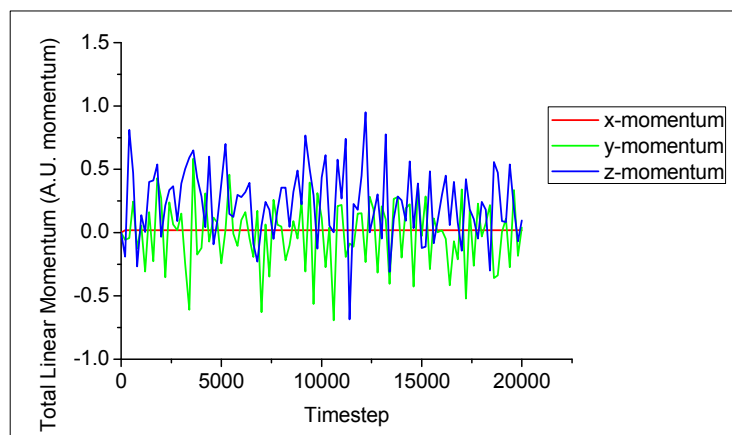


Figure 5-30: History of linear momentum of a material body under the effect of a magnetic field $\mathbf{B} = (1, 0, 0)$

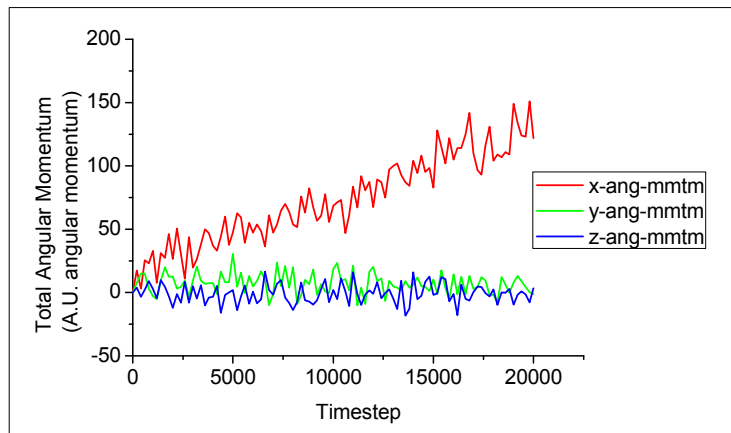


Figure 5-31: History of angular momentum of a material body under the effect of a magnetic field $\mathbf{B} = (1, 0, 0)$

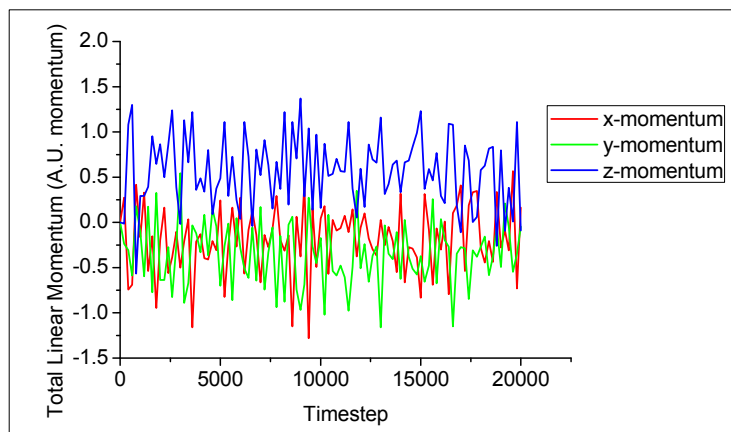


Figure 5-32: History of linear momentum of a material body under the effect of a magnetic field $\mathbf{B} = (1, 1, 1)$

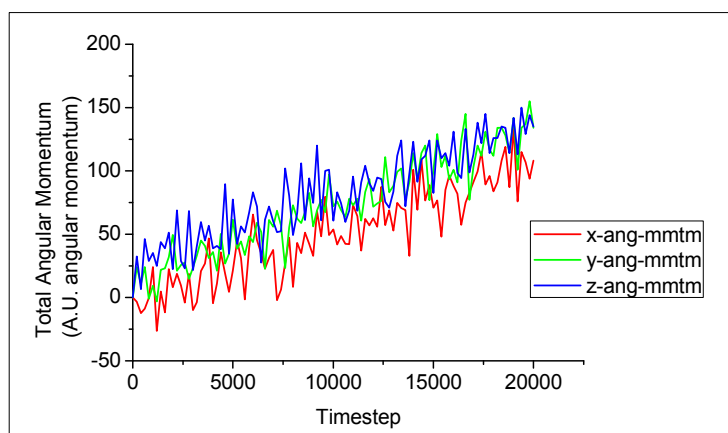


Figure 5-33: History of angular momentum of a material body under the effect of a magnetic field $\mathbf{B} = (1, 1, 1)$.

It is observed that the linear momentum in both case maintain at a stable level. In particular, when $\mathbf{B} = (1, 0, 0)$, no force is produced along the x-direction by the magnetic field, thus the linear momentum is preserved. On the contrary, the angular momentum in these two cases shows an interesting behavior. The x-component of angular velocity in case 1, and all three components of angular velocity in cases 2 are increasing along with time. The physical interpretation is that the material is accelerating spinning! More particularly, the acceleration of spinning occurs in the direction of the applied magnetic field.

This is due to the improper use of Velocity Verlet method in conducting MD with magnetic field. When \mathbf{a}^{n+1} is calculated by \mathbf{r}^{n+1} and $\mathbf{v}^{n+\frac{1}{2}}$, such that $\mathbf{a}^{n+1} = \mathbf{a}^{n+1}(\mathbf{r}^{n+1}, \mathbf{v}^{n+\frac{1}{2}})$, the half step error in \mathbf{v} is accumulated every time the magnetic force is calculated by the cross

product $\mathbf{v} \times \mathbf{B}$. This leads to the unphysical phenomenon that the material body is constantly accelerated to align with the \mathbf{B} field.

2) Using inversed method

Figure 5-34 and Figure 5-35 show the linear momentum and angular momentum of the material body with a magnetic field of $\mathbf{B} = (1, 1, 1)$, as obtained by inversed method. The result demonstrates that the linear momentum and angular momentum maintain at a stable level and do not drift away. This is compared to the unphysical results as previously obtained. It is concluded that the time integration method is of importance in studying the magnetic field response of atomistic material system.

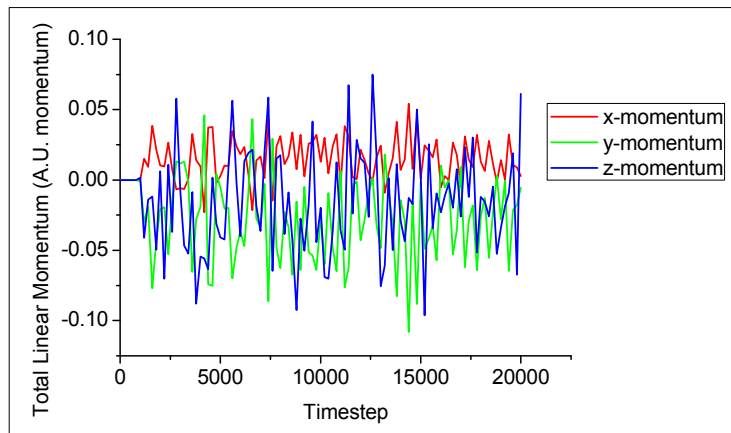


Figure 5-34: History of linear momentum of a material body under the effect of a magnetic field $\mathbf{B} = (1, 1, 1)$, as obtained by inversed method.

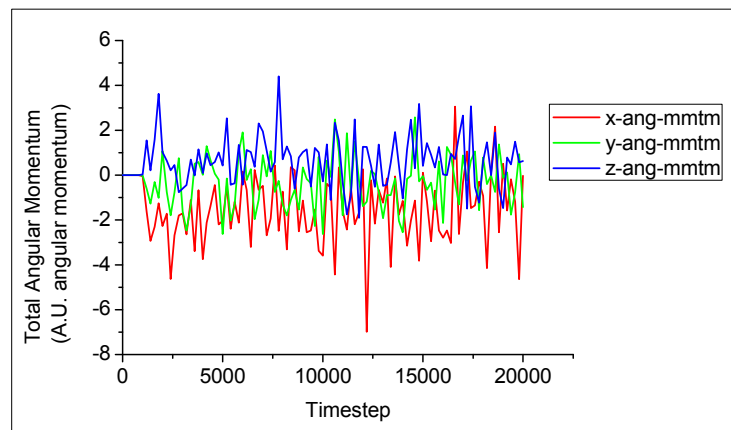


Figure 5-35: History of angular momentum of a material body under the effect of a magnetic field $\mathbf{B} = (1, 1, 1)$, as obtained by inversed method.

5.4 Summary

In this chapter, several kinds of material behaviors of nanopolycrystalline materials, such as mechanical, thermal, electrical and magnetic behaviors are studied via simulation. To begin with, mechanical properties of single nanocrystalline solids are obtained through simple tension, simple compression and simple shear tests. Then the material response of a nanopolycrystalline specimen under mechanical loading is analyzed. For thermal analysis, heating and cooling process are realized on nanopolycrystals via upgraded Nose-Hoover thermostat, during which melting and grain growth phenomena are observed, respectively. Besides the uniform heat bath analysis, two demonstrations of heat conduction simulations are achieved by local temperature control. The result of heat conduction unveils the inhomogeneity feature of nanopolycrystals. Lastly, to study the EM-field induced motions of atomistic material systems, electrical field and magnetic field are included in the MD simulation. Testing cases show that time integration method need careful attention when a magnetic field is present.

CHAPTER 6: CONCLUSION AND FUTURE WORK

6.1 Conclusion

In this research, a systematic approach for atomistic modeling and simulation of nanopolycrystalline solids has been constructed. Many challenges, as mentioned in the introduction chapter, have been addressed. The merits and advancement of this research lie in its theory, techniques and applications.

6.1.1 Non-equilibrium molecular dynamics

This research starts the physical model and mathematical representation with molecular dynamics (MD), which is proved to be a capable and credible tool to study the nano-structured materials.

In addition to the latest theories and techniques of non-equilibrium molecular dynamics (NEMD) simulations, this research proposes the theory of Objectivity Incorporated Molecular Dynamics (OIMD), in which both governing equation and constitutive equations satisfy principle of objectivity, i.e. they are form-invariant under change of reference frame. The theory of OIMD provides an MD solution for all kinds of reference frames (inertial or non-inertial). As a consequence of following the principle objectivity, an observation in any reference frame is sufficient to capture the essence of one physical process (which may also

be observed in many other reference frames). OIMD is considered as a new theoretical foundation for the investigation of multi-physics phenomena at atomic scale.

To investigate a broad range of properties of nanopolycrystalline solids, this research considers the effects by external electrical and magnetic field. Therefore, the governing equation is supplemented with EM field body force. Maxwell's equations at atomic scale and induced EM quantities are presented.

6.1.2 Numerical scheme

The equations of motions in classical MD simulations can be integrated through Velocity Verlet methods, which is simple, fast and most commonly used.

Since there are multi-physics body forces and fictitious force that are dependent on the instantaneous velocities of atoms, the original scheme of Velocity Verlet are not ready to integrate the equations of motion. This research introduces two methods to resolve the velocity-dependency issue. The first method, called Heun's method, involves twice calculations of force in each time step and the accuracy is improved. This scheme is in general suitable to calculate velocity-dependent force, no matter whether velocity is involved in a linear or a non-linear way. The main drawback of Heun's method is also obvious that the computational cost is high since the extra time of calculation of force in each time step. The second method, called inversed method, can be used when the velocity

acts in a linear way in the force calculation. For example, velocity enters the cross product with the magnetic field to give the Lorentz force when there exists an external magnetic field. Inversed method takes the advantage of the linearity of the velocity-force relation in the Lorentz force term, and provides an explicit scheme to update the velocity and force at the next time step. It can be shown that this method is almost as fast as Velocity Verlet method while it is more stable and accurate. It is noted that while all these numerical integration methods are used in this research, the selection of a particular method depends on the simulation settings and the requirement of accuracy or computational time.

6.1.3 Interatomic potential database

Most of the reported MD research on nanopolycrystalline materials is focused on monatomic materials systems (mostly metallic), such as nickel or copper. A few researches involve more than one kind of atom, such as a certain species of metal oxides or metal alloy. No general scheme was reported to simulate a heterogeneous nanopolycrystalline material system with different types of atom and chemicals.

In order to deal with a broad spectrum of materials with a variety of physical properties, this research has established a database of interatomic potentials and their potential parameters. Since most of the potential parameters were developed separately, a protocol to link different database is devised so that the potential parameters from different data sources can be used simultaneously, in the meantime the advantages of each separate set of

potential parameters can be mostly preserved. Combination rule, as commonly adopted to mix different potential parameters, is considered as the key to link different potential parameters from different sources thus is revisited and validated. The investigation demonstrates that the potential parameters obtained by the combination rule are able to provide a smooth interaction between atoms.

The database established by this research covers many elements in the periodic table. It means that in principle a variety of materials that consist of these chemical elements can be studied with this framework.

6.1.4 Structure optimization and prediction of multiple phases of crystallites

The previous research of MD study of nanopolycrystalline materials mainly focuses on a certain type of crystal structure, while little discussion is given to the different possible structures of a crystallite.

This research performs structure optimization study based on the mathematical formula and parameters of interatomic potential and potential parameters. The optimization results predict reasonable unit cell information which is in great agreement with the experimental results. Moreover, the optimization results also show that one chemical formula of crystal can have more than one form of stable (or meta-stable) structures, which is called

polymorphism phenomenon. Therefore, multi-phase grains can now be realized in the modeling and simulation of nanopolycrystalline materials.

6.1.5 Multi-grain nanopolycrystalline material system

The main task of the model construction process is to create nanopolycrystalline models with grains and grain boundaries, where the grains consist of different kinds of crystallites and are arranged in arbitrary orientations, and grain boundaries consist of amorphous phase atoms.

To construct the gains system, two in-house algorithms are used in this research: Voronoi method and grain nucleation method. While Voronoi method is also commonly used in existing research, it can only generate grains in the shape of convex polygon. In contrast, the grain nucleation method may give a model more close to the natural multi-grain nanostructure, where there may be irregular grain boundaries and more intertwined and integrated grains.

For the grain boundaries, amorphous phase atoms are firstly obtained via amorphization process and then filled to the gap between the grains.

These modeling techniques can produce nanopolycrystalline material system with selective and controllable structural feature. In particular, there can be arbitrary kinds of crystallites,

arbitrary phases of crystallites, arbitrary grain geometry, arbitrary grain orientation and amorphous grain boundaries in the material system. These are all structural variables that can be used to study the structural impact on material properties.

6.1.6 Simulated behaviors

Several simulations are performed to demonstrate the capability of this work on understanding the behaviors of nanopolycrystalline materials.

Firstly, Simple tension, simple compression and simple shear tests are performed on single-crystalline solids. In each simulation, the material failure occurs in a featured way that reflects the mechanical loading. Then, material constants, such as young's modulus and shear modulus, are obtained and compared with experimental result. Since the calculated elastic constants are in agreement with experimental results, it is considered that the potential parameters used in the study are of good quality in restoring the macroscopic properties of the materials. Secondly, mechanical response of a large and complex nanopolycrystals is studied. The material failure shows an interesting behavior: most of the dislocations initiate in the grain boundaries thus the failure path lies along the grain boundaries. This simulation is a clear demonstration that the grain boundaries have a key effect on the mechanical properties of nanopolycrystalline solids.

For thermal analysis, heating process, cooling process, and heat conduction simulations are realized with upgraded Nose-Hoover thermostat. The simulation of heating up a block of nanopolycrystal shows that the specimen will sustain the nanocrystalline structure at a relatively high temperature while melt at a higher temperature. The study of thermal stability of nanopolycrystalline materials can be extended such that many interesting phenomena such as melting-point depression can be studied. The simulation of cooling process replicates the phenomenon of grain growth, where multiple grains may merge during the heat treatment. The heat conduction cases show that the upgraded Nose-Hoover thermostat can be used for local temperature control. By controlling the temperature at different regions in the specimen, temperature gradient can be produced between the temperature-controlled regions. Although the testing problems are artificially defined, the simulation realizes distributed temperature control, which is advancement in the NEMD.

Lastly, testing cases with the presence of electromagnetic field are studied. It is noted in this research that while the equation of motion of MD can be modified by simply adding the EM force terms, the integration method needs more attention. Testing cases demonstrate that the original Velocity Verlet method can approximate the time marching by calculating Lorentz force based on half-time-step-lag velocity, but it also introduces undesirable drift in angular momentum. The inversed method, which can be derived from the same scheme of Velocity Verlet method, provides an explicit form to update velocity. Simulation results show that the inversed method will not introduce undesirable drift in angular momentum and thus is considered a better integration method in studying atomistic material systems with the presence of EM field.

6.2 Recommendations for Future Studies

This research provides the groundwork for atomistic modeling and simulation of nanopolycrystalline solids. The applications are anticipated to facilitate the rational design and application of nanostructured materials in the future.

In the meantime, this research has mainly focused on the development of theory and techniques. The performed simulation work demonstrates the capability and validity of the developed approach, and the main interest in these simulation cases is the phenomenological and qualitative behaviors of the sample material system. At current stage, less detailed attention is given to the quantitative comparison between the simulation results and the experimental results. Therefore, in order to investigate realistic problems with practical applications, quantitative study of particular behavior of a particular composition of nanopolycrystalline solids under certain external loading is required. The qualitative study and potential applications of nanopolycrystalline solids are proposed here in several directions and are left for future studies.

6.2.1 Parametric studies of material properties influenced by different interatomic potentials and potential parameters

It is clear that the interatomic potential is the heart of molecular dynamics simulations and dictates the simulated behaviors. This work has established a database of many interatomic potentials and potential parameters, in which each set of potential parameters was obtained by other researchers through fitting with experimental data. It is wise to select a set of potential parameters such that the interested physical properties in the simulations are those that the potential parameters were initially fitted to. Therefore, a careful parametric study on the selection of potential parameters is recommended in each application of simulation study.

6.2.2 Parametric studies of material behaviors influenced by structural variables

The properties of a material are influenced profoundly by its microstructures. This work makes possible to control structural variables such as the kind of crystallites, the phase of crystallites, the grain geometry, the grain orientation and the grain boundaries geometry. It is recommended in the future studies to use these structural variables to investigate the structural impact on material properties, such as grain/grain-boundary ratio study and size-dependency study.

6.2.3 Thermo-mechanical-electrical-magnetic coupling

This research provides a basis for atomistic simulation of multi-physics material behaviors. In the current stage, initial study of nanopolycrystalline material under several physical loadings is conducted and validated. It is anticipated that this research can be used to study complex material systems with more complicated loadings in the future. In particular, thermo- mechanical- electrical- magnetic coupling of nanopolycrystalline materials can be investigated. Interesting topics may include thermoelectricity, piezoelectricity, etc.

BIBLIOGRAPHY

1. Koch, C.C.: Structural nanocrystalline materials : fundamentals and applications.
Cambridge University Press, Cambridge (2007)
2. Suryanarayana, C., Koch, C.C.: Nanocrystalline materials – Current research and future directions. *Hyperfine Interact* **130**(1-4), 5-44 (2000). doi:10.1023/a:1011026900989
3. Dunitz, J.D., Bernstein, J.: Disappearing Polymorphs. *Accounts of Chemical Research* **28**(4), 193-200 (1995). doi:10.1021/ar00052a005
4. Bernstein, J.: Polymorphism in molecular crystals. *International Union of Crystallography monographs on crystallography*, vol. 14. Oxford University Press, OxfordClarendon Press ; New York (2002)
5. Braga, D., Grepioni, F., Maini, L., Polito, M.: Crystal Polymorphism and Multiple Crystal Forms. In: Hosseini, M.W. (ed.) *Molecular Networks*, vol. 132. *Structure and Bonding*, pp. 87-95. Springer Berlin Heidelberg, (2009)
6. Atkins, P.W., Walters, V., De Paula, J.: *Physical Chemistry*. Macmillan Higher Education, (2006)
7. Hornbogen, E.: Hundred years of precipitation hardening. *Journal of Light Metals* **1**(2), 127-132 (2001). doi:[http://dx.doi.org/10.1016/S1471-5317\(01\)00006-2](http://dx.doi.org/10.1016/S1471-5317(01)00006-2)
8. Merica, P.D., Waltenberg, R.G.: Heat treatment of duralumin. *Scientific papers of the Bureau of Standards*, vol. no 347. Govt. Print. Off., Washington, (1919)

9. Preston, G.: Structure of age-hardened aluminium-copper alloys. *Nature* **142**, 570 (1938).
10. Guinier, A.: Structure of age-hardened aluminium-copper alloys. *Nature* **142**, 569-570 (1938).
11. Silcock, J.M., Heal, T.J., Hardy, H.K.: Structural ageing characteristics of binary aluminium-copper alloys. *Journal of the Institute of Metals* **82**, 239-248 (1953).
12. Cohen, J.: The early stages of solute distribution below a transition temperature. *Metallurgical Transactions A* **23**(10), 2685-2697 (1992).
13. Gleiter, H.: Nanocrystalline materials. *Progress in Materials Science* **33**(4), 223-315 (1989).
14. Van Swygenhoven, H., Derlet, P., Hasnaoui, A.: Atomic mechanism for dislocation emission from nanosized grain boundaries. *Physical Review B* **66**(2), 024101 (2002).
15. Yamakov, V., Wolf, D., Phillpot, S.R., Mukherjee, A.K., Gleiter, H.: Dislocation processes in the deformation of nanocrystalline aluminium by molecular-dynamics simulation. *Nature materials* **1**(1), 45-49 (2002).
16. Wolf, D., Yamakov, V., Phillpot, S., Mukherjee, A., Gleiter, H.: Deformation of nanocrystalline materials by molecular-dynamics simulation: relationship to experiments? *Acta Materialia* **53**(1), 1-40 (2005).
17. Ovid'ko, I.i.a.A.e., Tsakalakos, T., Ovid'ko, I.A., Vasudevan, A.K.: Nanostructures: synthesis, functional properties and applications, vol. 128. Springer, (2003)

18. Van Swygenhoven, H., Farkas, D., Caro, A.: Grain-boundary structures in polycrystalline metals at the nanoscale. *Physical Review B* **62**(2), 831 (2000).
19. Van Swygenhoven, H., Derlet, P.: Grain-boundary sliding in nanocrystalline fcc metals. *Physical Review B* **64**(22), 224105 (2001).
20. Van Swygenhoven, H., Derlet, P., Frøseth, A.: Stacking fault energies and slip in nanocrystalline metals. *Nature materials* **3**(6), 399-403 (2004).
21. Derlet, P., Van Swygenhoven, H.: Length scale effects in the simulation of deformation properties of nanocrystalline metals. *Scripta Materialia* **47**(11), 719-724 (2002).
22. Yamakov, V., Wolf, D., Phillpot, S., Gleiter, H.: Deformation twinning in nanocrystalline Al by molecular-dynamics simulation. *Acta Materialia* **50**(20), 5005-5020 (2002).
23. Yamakov, V., Wolf, D., Phillpot, S., Mukherjee, A., Gleiter, H.: Deformation-mechanism map for nanocrystalline metals by molecular-dynamics simulation. *Nature materials* **3**(1), 43-47 (2003).
24. Kumar, K., Van Swygenhoven, H., Suresh, S.: Mechanical behavior of nanocrystalline metals and alloys. *Acta Materialia* **51**(19), 5743-5774 (2003).
25. Samaras, M., Derlet, P., Van Swygenhoven, H., Victoria, M.: Stacking fault tetrahedra formation in the neighbourhood of grain boundaries. *Nuclear Instruments and Methods in Physics Research Section B: Beam Interactions with Materials and Atoms* **202**, 51-55 (2003).

26. Hasnaoui, A., Derlet, P., Van Swygenhoven, H.: Interaction between dislocations and grain boundaries under an indenter—a molecular dynamics simulation. *Acta Materialia* **52**(8), 2251-2258 (2004).
27. Frøseth, A., Van Swygenhoven, H., Derlet, P.: The influence of twins on the mechanical properties of nc-Al. *Acta Materialia* **52**(8), 2259-2268 (2004).
28. Rapaport, D.C.: *The art of molecular dynamics simulation*, 2nd ed. Cambridge University Press, Cambridge, UK ; New York, NY (2004)
29. Frenkel, D., Smit, B.: *Understanding molecular simulation : from algorithms to applications*, 2nd ed. Computational science series, vol. 1. Academic Press, San Diego (2002)
30. Haile, J.M. (ed.) *Molecular Dynamics Simulation: Elementary Methods* Wiley-Interscience, (1997)
31. Allen, M.P., Tildesley, D.J.: *Computer simulation of liquids*. Oxford University Press, Oxford England (1987)
32. Irving, J.H., Kirkwood, J.G.: The Statistical Mechanical Theory of Transport Processes. IV. The Equations of Hydrodynamics. *The Journal of Chemical Physics* **18**(6), 817-829 (1950). doi:doi:<http://dx.doi.org/10.1063/1.1747782>
33. Hardy, R.J.: Formulas for determining local properties in molecular-dynamics simulations: Shock waves. *The Journal of Chemical Physics* **76**(1), 622-628 (1982). doi:doi:<http://dx.doi.org/10.1063/1.442714>

34. Muller-Plathe, F.: A simple nonequilibrium molecular dynamics method for calculating the thermal conductivity. *The Journal of Chemical Physics* **106**(14), 6082-6085 (1997). doi:10.1063/1.473271
35. Castejon, H.J.: Nonequilibrium Molecular Dynamics Calculation of the Thermal Conductivity of Solid Materials. *The Journal of Physical Chemistry B* **107**(3), 826-828 (2002). doi:10.1021/jp021189z
36. Baranyai, A., aacute: Heat flow studies for large temperature gradients by molecular dynamics simulation. *Physical Review E* **54**(6), 6911 (1996).
37. Lepri, S., Livi, R., Politi, A.: Thermal conduction in classical low-dimensional lattices. *Physics Reports* **377**(1), 1-80 (2003). doi:Doi: 10.1016/s0370-1573(02)00558-6
38. Poulidakos, D., Arcidiacono, S., Maruyama, S.: Molecular dynamics simulation in nanoscale heat transfer: A review. *Microscale Thermophysical Engineering* **7**(3), 181-206 (2003).
39. Chantrenne, P., Barrat, J.: Finite size effects in determination of thermal conductivities: comparing molecular dynamics with simple models. *ASME Journal of Heat Transfer* **126**, 577-585 (2004).
40. Tokumasu, T., Kamijo, K.: Molecular dynamics study for the thermal conductivity of diatomic liquid. *Superlattices and Microstructures* **35**(3-6), 217-225 (2004). doi:DOI: 10.1016/j.spmi.2003.11.003
41. Weinan, E., Li, D.: The Andersen thermostat in molecular dynamics. *Commun Pur Appl Math* **61**(1), 96-136 (2008).

42. Li, D.: On the rate of convergence to equilibrium of the Andersen thermostat in molecular dynamics. *J Stat Phys* **129**(2), 265-287 (2007). doi:DOI 10.1007/s10955-007-9391-0
43. Koopman, E.A., Lowe, C.P.: Advantages of a Lowe-Andersen thermostat in molecular dynamics simulations. *J Chem Phys* **124**(20) (2006). doi:204103
10.1063/1.2198824
44. Stoyanov, S.D., Groot, R.D.: From molecular dynamics to hydrodynamics: A novel Galilean invariant thermostat. *J Chem Phys* **122**(11) (2005). doi:114112
10.1063/1.1870892
45. Chen, L.J., Lu, Z.Y., Qian, H.J., Li, Z.S., Sun, C.C.: The effects of Lowe-Andersen temperature controlling method on the polymer properties in mesoscopic simulations. *J Chem Phys* **122**(10) (2005). doi:104907
10.1063/1.1860351
46. Sturgeon, J.B., Laird, B.B.: Symplectic algorithm for constant-pressure molecular dynamics using a Nose-Poincare thermostat. *J Chem Phys* **112**(8), 3474-3482 (2000).
47. Lowe, C.P.: An alternative approach to dissipative particle dynamics. *Europhysics Letters* **47**(2), 145-151 (1999).
48. Sarman, S., Evans, D.J., Baranyai, A.: Extremum Properties of the Gaussian Thermostat. *Physica A* **208**(2), 191-204 (1994).

49. Andersen, H.C.: Molecular-Dynamics Simulations at Constant Pressure and-or Temperature. *J Chem Phys* **72**(4), 2384-2393 (1980).
50. Watanabe, H., Kobayashi, H.: Ergodicity of a thermostat family of the Nose-Hoover type. *Phys Rev E Stat Nonlin Soft Matter Phys* **75**(4 Pt 1), 040102 (2007).
51. Teramoto, T.: The Nose thermostat for the pattern formation dynamics. *Mol Simulat* **33**(1-2), 71-75 (2007). doi:Doi 10.1080/08927020601052914
52. Hoover, W.G., Aoki, K., Hoover, C.G., De Groot, S.V.: Time-reversible deterministic thermostats. *Physica D-Nonlinear Phenomena* **187**(1-4), 253-267 (2004).
doi:10.1016/j.physd.2003.09.016
53. Nose, S.: An improved symplectic integrator for Nose-Poincare thermostat. *J Phys Soc Jpn* **70**(1), 75-77 (2001).
54. Rateitschak, K., Klages, R., Hoover, W.G.: The Nose-Hoover thermostated Lorentz gas. *J Stat Phys* **101**(1-2), 61-77 (2000).
55. Hoover, W.G.: Generalization of Noses Isothermal Molecular-Dynamics - Non-Hamiltonian Dynamics for the Canonical Ensemble. *Phys Rev A* **40**(5), 2814-2815 (1989).
56. Hoover, W.G.: Constant-Pressure Equations of Motion. *Phys Rev A* **34**(3), 2499-2500 (1986).
57. Hoover, W.G.: Canonical Dynamics - Equilibrium Phase-Space Distributions. *Phys Rev A* **31**(3), 1695-1697 (1985).

58. Nose, S.: A Unified Formulation of the Constant Temperature Molecular-Dynamics Methods. *J Chem Phys* **81**(1), 511-519 (1984).
59. Martyna, G.J., Klein, M.L., Tuckerman, M.: NOSE-HOOVER CHAINS - THE CANONICAL ENSEMBLE VIA CONTINUOUS DYNAMICS. *J Chem Phys* **97**(4), 2635-2643 (1992).
60. Gueret, P., Merat, P., Moles, M., Vigier, J.P.: Stable States of a Relativistic Harmonic-Oscillator Imbedded in a Random Stochastic Thermostat. *Lett Math Phys* **3**(1), 47-56 (1979).
61. Gornostyrev, Y.N., Zhdkhin, D.I., Katsnel'son, M.I., Trefilov, A.V.: Stochastic resonance between limit cycles. Spring pendulum in a thermostat. *Jetp Lett+* **69**(8), 630-635 (1999).
62. Evans, D.J., Baranyai, A.: The Gaussian Thermostat, Phase-Space Compression and the Conjugate Pairing Rule. *Molecular Physics* **77**(6), 1209-1216 (1992).
63. Berendsen, H.J.C., Postma, J.P.M., Vangunsteren, W.F., Dinola, A., Haak, J.R.: Molecular-Dynamics with Coupling to an External Bath. *J Chem Phys* **81**(8), 3684-3690 (1984).
64. Golo, V.L., Shaitan, K.V.: Dynamic attractor for Berendsen's thermostat and the slow dynamics. *Biofizika* **47**(4), 611-617 (2002).
65. Khalili, M., Liwo, A., Jagielska, A., Scheraga, H.A.: Molecular dynamics with the united-residue model of polypeptide chains. II. Langevin and Berendsen-Bath

- dynamics and tests on model alpha-helical systems. *J Phys Chem B* **109**(28), 13798-13810 (2005). doi:10.1021/jp058007w
66. Lemak, A.S., Balabaev, N.K.: ON THE BERENDSEN THERMOSTAT. *Mol Simulat* **13**(3), 177-187 (1994).
67. Mudi, A., Chakravarty, C.: Effect of the Berendsen thermostat on the dynamical properties of water. *Molecular Physics* **102**(7), 681-685 (2004).
doi:10.1080/00268970410001698937
68. Yang, Z., Lee, J.D., Eskandarian, A.: Objectivity Incorporated Molecular Dynamics. (2014).
69. Eringen, A.C.: *Mechanics of continua*. R. E. Krieger Pub. Co., (1980)
70. Eringen, A.C.: *Microcontinuum Field Theories.: Volume 1, Foundations and solids*. Springer Verlag, (1999)
71. Eringen, A.C.: *Microcontinuum Field Theories: II. Fluent Media*. Springer, (2001)
72. Li, J., Lee, J.D.: Reformulation of the Nosé–Hoover thermostat for heat conduction simulation at nanoscale. *Acta Mechanica* **225**(4-5), 1223-1233 (2014).
doi:10.1007/s00707-013-1046-4
73. Xu, R., Liu, B., He, X.Q., Li, D.C.: Kinetic Energy-Based Temperature Computation in Non-Equilibrium Molecular Dynamics Simulation. *J Comput Theor Nanos* **9**(3), 428-433 (2012). doi:DOI 10.1166/jctn.2012.2042
74. de Groot, S.R., Suttrop, L.G.: *Foundations of electrodynamics*. North-Holland, (1972)

75. Süli, E., Mayers, D.F.: An introduction to numerical analysis. Cambridge University Press, Cambridge ; New York (2003)
76. Ziman, J.M.: Principles of the theory of solids, 2d ed. University Press, Cambridge Eng. (1972)
77. Ewald, P.P.: Die Berechnung optischer und elektrostatischer Gitter-potentiale. *Ann. Phys.* **64**, 253-287 (1921).
78. Wolf, D., Keblinski, P., Phillpot, S., Eggebrecht, J.: Exact method for the simulation of Coulombic systems by spherically truncated, pairwise r^{-1} summation. *The Journal of Chemical Physics* **110**(17), 8254-8282 (1999).
79. Lennard-Jones, J.E.: Cohesion. *Proceedings of the Physical Society* **43**(5), 461 (1931).
80. Born, M., Mayer, J.E.: Zur Gittertheorie der Ionenkristalle. *Zeitschrift für Physik A Hadrons and Nuclei* **75**(1), 1-18 (1932). doi:10.1007/bf01340511
81. Morse, P.M.: Diatomic Molecules According to the Wave Mechanics. II. Vibrational Levels. *Physical Review* **34**(1), 57 (1929).
82. Gale, J.D., Rohl, A.L.: The General Utility Lattice Program (GULP). *Molecular Simulation* **29**(5), 291-341 (2003).
83. Daw, M.S., Baskes, M.I.: Embedded-Atom Method - Derivation and Application to Impurities, Surfaces, and Other Defects in Metals. *Physical Review B* **29**(12), 6443-6453 (1984).

84. Sutton, A.P., Chen, J.: Long-range Finnis–Sinclair potentials. *Philosophical Magazine Letters* **61**(3), 139 - 146 (1990).
85. Finnis, M.W., Sinclair, J.E.: A simple empirical N -body potential for transition metals. *Philosophical Magazine A* **50**(1), 45 - 55 (1984).
86. Tersoff, J.: New Empirical-Approach for the Structure and Energy of Covalent Systems. *Physical Review B* **37**(12), 6991-7000 (1988).
87. Tersoff, J.: Modeling solid-state chemistry: Interatomic potentials for multicomponent systems. *Physical Review B* **39**(8), 5566 (1989).
88. Stillinger, F.H., Weber, T.A.: Computer simulation of local order in condensed phases of silicon. *Physical Review B* **31**(8), 5262-5271 (1985).
89. Catlow, C.R.A.: *Computer Modeling in Inorganic Crystallography*. Elsevier Science, (1997)
90. Catlow, C.R.A., Mackrodt, W.C.: *Computer simulation of solids*. Springer-Verlag, (1982)
91. Lalena, J.N., Cleary, D.A., Weiser, M.W.: *Principles of Inorganic Materials Design*. Wiley, (2010)
92. Bush, T.S., Gale, J.D., Catlow, C.R.A., Battle, P.D.: Self-consistent interatomic potentials for the simulation of binary and ternary oxides. *Journal of Materials Chemistry* **4**(6), 831-837 (1994). doi:10.1039/jm9940400831

93. Lewis, G.V., Catlow, C.R.A.: Potential Models for Ionic Oxides. *J Phys C Solid State* **18**(6), 1149-1161 (1985).
94. M. Woodley, S., D. Battle, P., D. Gale, J., Richard A. Catlow, C.: The prediction of inorganic crystal structures using a genetic algorithm and energy minimisation. *Physical Chemistry Chemical Physics* **1**(10), 2535-2542 (1999).
95. Levy, M.R., Grimes, R.W., Sickafus, K.E.: Disorder processes in A₃B₃O₃ compounds: implications for radiation tolerance. *Philosophical Magazine* **84**(6), 533-545 (2004). doi:10.1080/1478643032000158297
96. Collins, D.R., Catlow, C.R.A.: Computer-Simulation of Structures and Cohesive Properties of Micas. *Am Mineral* **77**(11-12), 1172-1181 (1992).
97. Minervini, L., Grimes, R.W., Sickafus, K.E.: Disorder in Pyrochlore Oxides. *Journal of the American Ceramic Society* **83**(8), 1873-1878 (2000). doi:10.1111/j.1151-2916.2000.tb01484.x
98. Minervini, L., Grimes, R.W., Tabira, Y., Withers, R.L., Sickafus, K.E.: The oxygen positional parameter in pyrochlores and its dependence on disorder. *Philosophical Magazine A* **82**(1), 123-135 (2002). doi:10.1080/01418610110066041
99. Exner, M., Donnerberg, H., Catlow, C., Schirmer, O.: Computer simulation of defects in KTaO₃. *Physical Review B* **52**(6), 3930-3940 (1995). doi:10.1103/PhysRevB.52.3930

100. Sepliarsky, M., Stachiotti, M.G., Migoni, R.L.: Structural Instabilities in K₂O₃ and K₂NaO₃ Described by the Nonlinear Oxygen Polarizability Model. *Physical Review B* **52**(6), 4044-4049 (1995).
101. Tinte, S., Stachiotti, M.G., Sepliarsky, M., Migoni, R.L., Rodriguez, C.O.: Atomistic modelling of BaTiO₃ based on first-principles calculations. *J Phys-Condens Mat* **11**(48), 9679-9690 (1999). doi:Doi 10.1088/0953-8984/11/48/325
102. Chen, J., Mi, J.G., Chan, K.Y.: Comparison of different mixing rules for prediction of density and residual internal energy of binary and ternary Lennard-Jones mixtures. *Fluid Phase Equilib* **178**(1-2), 87-95 (2001).
103. Mirskaya, K.V.: Combining Rules for Interatomic Potential Functions of Buckingham Form. *Tetrahedron* **29**(5), 679-682 (1973). doi:Doi 10.1016/0040-4020(73)80078-X
104. Buckingham, R.A.: The Classical Equation of State of Gaseous Helium, Neon and Argon, vol. 168. vol. 933(1938)
105. Chen, J., Lee, J.D.: Multiscale Modeling of Fracture: Buckingham Catastrophe and Remedy. *Int. J. Terraspace Sci. Eng* **3**, 177-183 (2011).
106. Chen, J., Lee, J.D.: The Buckingham Catastrophe in multiscale modelling of fracture. *International Journal of Theoretical and Applied Multiscale Mechanics* **2**(1), 3-11 (2011).
107. Chen, J., Lee, J.: Multiscale modeling of fracture of MgO: Sensitivity of interatomic potentials. *Theoretical and Applied Fracture Mechanics* **53**(1), 74-79 (2010).
108. Mindat.org: Rock Salt. <http://www.mindat.org/min-5538.html>. Accessed 12/20/2014

109. Seitz, F.: The Modern Theory of Solids. McGraw-Hill Book Company, Incorporated, (1940)
110. Anthony, J.W.: Handbook of Mineralogy: Halides, Hydroxides, Oxides. Mineral Data Publishing, (1997)
111. Mindat.org: Perovskite Group. <http://www.mindat.org/min-29176.html>. Accessed 12/20/2014
112. Mindat.org: Wurtzite. <http://www.mindat.org/min-4318.html>. Accessed 12/20/2014
113. Subramanian, M.A., Aravamudan, G., Subba Rao, G.V.: Oxide pyrochlores — A review. Progress in Solid State Chemistry **15**(2), 55-143 (1983).
doi:[http://dx.doi.org/10.1016/0079-6786\(83\)90001-8](http://dx.doi.org/10.1016/0079-6786(83)90001-8)
114. Mindat.org: Pyrochlore Group. <http://www.mindat.org/min-3316.html>. Accessed 12/20/2014
115. Springer: Material Science Online Database.
<http://www.springermaterials.com/docs/index.html>. Accessed 12/20/2014
116. Chen, D.: Structural modeling of nanocrystalline materials. Computational Materials Science **3**(3), 327-333 (1995). doi:[http://dx.doi.org/10.1016/0927-0256\(94\)00072-K](http://dx.doi.org/10.1016/0927-0256(94)00072-K)
117. D'Agostino, G., Van Swygenhoven, H.: Structural and mechanical properties of a simulated nickel nanophase. In: MRS Proceedings 1995, p. 293. Cambridge Univ Press

118. Van Swygenhoven, H., Caro, A.: Plastic behavior of nanophase Ni: a molecular dynamics computer simulation. *Applied Physics Letters* **71**(12), 1652-1654 (1997).
119. Van Swygenhoven, H., Caro, A.: Molecular dynamics computer simulation of nanophase Ni: structure and mechanical properties. *Nanostructured Materials* **9**(1), 669-672 (1997).
120. Phillpot, S., Wolf, D., Gleiter, H.: A structural model for grain boundaries in nanocrystalline materials. *Scripta metallurgica et materialia* **33**(8), 1245-1251 (1995).
121. Phillpot, S., Wolf, D., Gleiter, H.: Molecular-dynamics study of the synthesis and characterization of a fully dense, three-dimensional nanocrystalline material. *Journal of Applied Physics* **78**(2), 847-861 (1995).
122. Aurenhammer, F.: Voronoi diagrams—a survey of a fundamental geometric data structure. *ACM Computing Surveys (CSUR)* **23**(3), 345-405 (1991).
123. Goldstein, H., Poole, C.P., Safko, J.L.: *Classical mechanics*, 3rd ed. Addison Wesley, San Francisco (2002)
124. Magnesium oxide (MgO) Young's, shear and bulk moduli, Poisson's ratio. In: Madelung, O., Rössler, U., Schulz, M. (eds.) *II-VI and I-VII Compounds; Semimagnetic Compounds*, vol. 41B. *Landolt-Börnstein - Group III Condensed Matter*, pp. 1-3. Springer Berlin Heidelberg, (1999)
125. AZO-Materials: *Magnesia - Magnesium Oxide (MgO) Properties & Applications*. <http://www.azom.com/properties.aspx?ArticleID=54>. Accessed 12/20/2014

126. Xiong, L.M., Chen, Y.P., Lee, J.D.: Atomistic measure of the strength of MgO nanorods. *Theoretical and Applied Fracture Mechanics* **46**(3), 202-208 (2006).
doi:<http://dx.doi.org/10.1016/j.tafmec.2006.09.007>
127. Haynes, W.M.: *CRC Handbook of Chemistry and Physics*, 93rd Edition. Taylor & Francis, (2012)
128. Jiang, A., Awasthi, N., Kolmogorov, A., Setyawan, W., Börjesson, A., Bolton, K., Harutyunyan, A., Curtarolo, S.: Theoretical study of the thermal behavior of free and alumina-supported Fe-C nanoparticles. *Physical Review B* **75**(20), 205426 (2007).
129. Lopeandía, A.F., Rodríguez-Viejo, J.: Size-dependent melting and supercooling of Ge nanoparticles embedded in a SiO₂ thin film. *Thermochimica Acta* **461**(1–2), 82-87 (2007). doi:<http://dx.doi.org/10.1016/j.tca.2007.04.010>
130. Sun, J., Simon, S.L.: The melting behavior of aluminum nanoparticles. *Thermochimica Acta* **463**(1–2), 32-40 (2007).
doi:<http://dx.doi.org/10.1016/j.tca.2007.07.007>

APPENDICES

APPENDIX - I PROOF OF THE OBJECTIVITY OF THE THERMAL VELOCITY

To begin with, an atomic material system or sub-system, which has N atoms, each with mass m^i , position vector \mathbf{r}^i , and velocity vector \mathbf{v}^i ; $i = 1, 2, 3, \dots, N$.

The total mass, position of the centroid and the bulk velocity are:

$$M \equiv \sum_{i=1}^N m^i \quad (\text{A-1.1})$$

$$\bar{\mathbf{r}} \equiv \left(\sum_{i=1}^N m^i \mathbf{r}^i \right) / M \quad (\text{A-1.2})$$

$$\bar{\mathbf{v}} \equiv \left(\sum_{i=1}^N m^i \mathbf{v}^i \right) / M \quad (\text{A-1.3})$$

The relative position and relative velocity are defined as

$$\hat{\mathbf{r}}^i \equiv \mathbf{r}^i - \bar{\mathbf{r}} \quad (\text{A-1.4})$$

$$\hat{\mathbf{v}}^i \equiv \mathbf{v}^i - \bar{\mathbf{v}} \quad (\text{A-1.5})$$

The total angular momentum is

$$\mathbf{L} = \sum_{i=1}^N m^i \hat{\mathbf{r}}^i \times \hat{\mathbf{v}}^i \quad \text{or} \quad L_n = e_{nkl} \sum_{i=1}^N m^i \hat{r}_k^i \hat{v}_l^i \quad (\text{A-1.6})$$

The moment of inertia of the atomic system with respect to the centroid is

$$J_{np} \equiv \sum_{i=1}^N m^i (\hat{r}_k^i \hat{r}_k^i \delta_{np} - \hat{r}_n^i \hat{r}_p^i) \quad (\text{A-1.7})$$

Angular velocity of the system is

$$\mathbf{L} = \mathbf{J}\boldsymbol{\omega} \Rightarrow \boldsymbol{\omega} = \mathbf{J}^{-1}\mathbf{L} \quad (\text{A-1.8})$$

Then the part of velocity that the i^{th} atom contributes to the rotation is

$$\boldsymbol{\eta}^i = \boldsymbol{\omega} \times \hat{\mathbf{r}}^i \quad \text{or} \quad \eta_n^i = e_{nkl} \omega_k \hat{r}_l^i \quad (\text{A-1.9})$$

With above information, the expression of the thermal velocity is obtained:

$$\tilde{\mathbf{v}}^i \equiv \mathbf{v}^i - \bar{\mathbf{v}} - \boldsymbol{\eta}^i \quad (\text{A-1.10})$$

Or in index notation

$$\tilde{v}_k^i = v_k^i - \frac{1}{M} \sum_{j=1}^N m^j v_k^j - e_{kij} J_{il}^{-1} \left(e_{lmn} \sum_{j=1}^N m^j \hat{r}_m^j \hat{v}_n^j \right) \hat{r}_j^i \quad (\text{A-1.11})$$

Theorem 1. The objective velocity $\tilde{\mathbf{v}}^i$ is an objective vector, i.e. it obeys the transformation law

$$\left(\tilde{\mathbf{v}}_k^i\right)^* = Q_{kl} \tilde{\mathbf{v}}_l^i \quad (\text{A-1.12})$$

Proof:

The right hand side of Eq. (A-1.12) can be written as:

$$Q_{kl} \tilde{\mathbf{v}}_l^i = Q_{kl} \left[\mathbf{v}_l^i - \frac{1}{M} \sum_{j=1}^N m^j \mathbf{v}_l^j - e_{lij} J_{ip}^{-1} \left(e_{prs} \sum_{j=1}^N m^j \hat{\mathbf{r}}_r^j \hat{\mathbf{v}}_s^j \right) \hat{\mathbf{r}}_j^i \right] \quad (\text{A-1.13})$$

By using the formula

$$e_{ijk} e_{lmn} = \delta_{il} (\delta_{jm} \delta_{kn} - \delta_{jn} \delta_{km}) + \delta_{im} (\delta_{jn} \delta_{kl} - \delta_{jl} \delta_{kn}) + \delta_{in} (\delta_{jl} \delta_{km} - \delta_{jm} \delta_{kl}) \quad (\text{A-1.14})$$

It can be further derived as

$$\begin{aligned} Q_{kl} \tilde{\mathbf{v}}_l^i &= Q_{kl} \mathbf{v}_l^i - Q_{kl} \left(\frac{1}{M} \sum_{j=1}^N m^j \mathbf{v}_l^j \right) - Q_{kl} (e_{lij} e_{prs}) J_{ip}^{-1} \left(\sum_{j=1}^N m^j \hat{\mathbf{r}}_r^j \hat{\mathbf{v}}_s^j \right) \hat{\mathbf{r}}_j^i \\ &= Q_{kl} \mathbf{v}_l^i - Q_{kl} \left(\frac{1}{M} \sum_{j=1}^N m^j \mathbf{v}_l^j \right) \\ &\quad - \left[Q_{kp} (J_{rp}^{-1} \hat{\mathbf{r}}_s^i - J_{sp}^{-1} \hat{\mathbf{r}}_r^i) + Q_{kr} (J_{sp}^{-1} \hat{\mathbf{r}}_p^i - J_{pp}^{-1} \hat{\mathbf{r}}_s^i) + Q_{ks} (J_{pp}^{-1} \hat{\mathbf{r}}_r^i - J_{rp}^{-1} \hat{\mathbf{r}}_p^i) \right] \left(\sum_{j=1}^N m^j \hat{\mathbf{r}}_r^j \hat{\mathbf{v}}_s^j \right) \end{aligned} \quad (\text{A-1.15})$$

Recall the definition of objectively equivalent motions as in Eq.(2.25):

$$\left(x_k^i\right)^* = Q_{kl} x_l^i + b_k \quad (\text{A-1.16})$$

We can write down the position vectors in starred reference frame:

$$\begin{aligned} \left(r_k^i\right)^* &= Q_{kl} r_l^i + b_k \\ \left(\bar{r}_k^i\right)^* &= \left(\sum_{i=1}^N m^i Q_{kl} r_l^i + \sum_{i=1}^N m^i b_k \right) / M = Q_{kl} \bar{r}_l^i + b_k \\ \left(\hat{r}_k^i\right)^* &= \left(r_k^i\right)^* - \left(\bar{r}_k^i\right)^* = Q_{kl} \hat{r}_l^i \end{aligned} \quad (\text{A-1.17})$$

and the velocity vectors in starred reference frame:

$$\begin{aligned} \left(v_k^i\right)^* &= Q_{kl} v_l^i + \dot{Q}_{kl} r_l^i + \dot{b}_k \\ \left(\bar{v}_k^i\right)^* &= Q_{kl} \bar{v}_l^i + \dot{Q}_{kl} \bar{r}_l^i + \dot{b}_k \\ \left(\hat{v}_k^i\right)^* &= Q_{kl} \hat{v}_l^i + \dot{Q}_{kl} \hat{r}_l^i \end{aligned} \quad (\text{A-1.18})$$

The moment of inertia and its inverse matrix are both objective:

$$\begin{aligned} \left(J_{np}\right)^* &= \sum_{i=1}^N m^i \left[\left(\hat{r}_k^i\right)^* \left(\hat{r}_k^i\right)^* \delta_{np} - \left(\hat{r}_n^i\right)^* \left(\hat{r}_p^i\right)^* \right] \\ &= Q_{nr} Q_{ps} \sum_{i=1}^N m^i \left(\hat{r}_k^i \hat{r}_k^i \delta_{rs} - \hat{r}_r^i \hat{r}_s^i \right) \\ &= Q_{nr} Q_{ps} J_{rs} \\ \left(J_{np}^{-1}\right)^* &= Q_{nr} Q_{ps} \left(J_{rs}^{-1}\right) \end{aligned} \quad (\text{A-1.19})$$

The results of Eq.(A-1.17) - (A-1.19) and also the definition in Eq.(A-1.11) can be used to further derive the left side of Eq.(A-1.12) :

$$\begin{aligned}
(\hat{v}_k^i)^* &= \mathcal{Q}_{kl} v_l^i - \mathcal{Q}_{kl} \left(\frac{1}{M} \sum_{j=1}^N m^j v_l^j \right) + \dot{\mathcal{Q}}_{kl} \hat{r}_l^i \\
&\quad - e_{kij} \left(\mathcal{Q}_{ip} \mathcal{Q}_{lq} J_{pq}^{-1} \right) \left\{ e_{lmn} \left[\mathcal{Q}_{mr} \mathcal{Q}_{ns} \left(\sum_{j=1}^N m^j \hat{r}_r^j \hat{v}_s^j \right) + \mathcal{Q}_{mr} \dot{\mathcal{Q}}_{ns} \left(\sum_{j=1}^N m^j \hat{r}_r^j \hat{r}_s^j \right) \right] \right\} \mathcal{Q}_{jt} \hat{r}_t^i \\
&= \mathcal{Q}_{kl} v_l^i - \mathcal{Q}_{kl} \left(\frac{1}{M} \sum_{j=1}^N m^j v_l^j \right) - (e_{kij} e_{lmn}) \left[\mathcal{Q}_{ip} \mathcal{Q}_{lq} J_{pq}^{-1} \mathcal{Q}_{mr} \mathcal{Q}_{ns} \left(\sum_{j=1}^N m^j \hat{r}_r^j \hat{v}_s^j \right) \right] \mathcal{Q}_{jt} \hat{r}_t^i \\
&\quad + \dot{\mathcal{Q}}_{kl} \hat{r}_l^i - (e_{kij} e_{lmn}) \left[\mathcal{Q}_{ip} \mathcal{Q}_{lq} J_{pq}^{-1} \mathcal{Q}_{mr} \dot{\mathcal{Q}}_{ns} \left(\sum_{j=1}^N m^j \hat{r}_r^j \hat{r}_s^j \right) \right] \mathcal{Q}_{jt} \hat{r}_t^i \\
&= \left\{ \mathcal{Q}_{kl} v_l^i - \mathcal{Q}_{kl} \left(\frac{1}{M} \sum_{j=1}^N m^j v_l^j \right) \right. \\
&\quad \left. - \left[J_{pp}^{-1} (\mathcal{Q}_{ks} \hat{r}_r^i - \mathcal{Q}_{kr} \hat{r}_s^i) + J_{rp}^{-1} (\mathcal{Q}_{kp} \hat{r}_s^i - \mathcal{Q}_{ks} \hat{r}_p^i) + J_{sp}^{-1} (\mathcal{Q}_{kr} \hat{r}_p^i - \mathcal{Q}_{kp} \hat{r}_r^i) \right] \left(\sum_{j=1}^N m^j \hat{r}_r^j \hat{v}_s^j \right) \right\} \\
&\quad + \left\{ \dot{\mathcal{Q}}_{kl} \hat{r}_l^i - (e_{kij} e_{lmn}) \left[\mathcal{Q}_{ip} \mathcal{Q}_{lq} J_{pq}^{-1} \mathcal{Q}_{mr} \dot{\mathcal{Q}}_{ns} \left(\sum_{j=1}^N m^j \hat{r}_r^j \hat{r}_s^j \right) \right] \mathcal{Q}_{jt} \hat{r}_t^i \right\}
\end{aligned} \tag{A-1.20}$$

Note that the term in the first bracket in the last line of Eq.(A-1.20) is identical to the result in Eq.(A-1.15). Therefore, the remaining of the proof is equivalent to prove

$$\dot{\mathcal{Q}}_{kl} \hat{r}_l^i - (e_{kij} e_{lmn}) \left[\mathcal{Q}_{ip} \mathcal{Q}_{lq} J_{pq}^{-1} \mathcal{Q}_{mr} \dot{\mathcal{Q}}_{ns} \left(\sum_{j=1}^N m^j \hat{r}_r^j \hat{r}_s^j \right) \right] \mathcal{Q}_{jt} \hat{r}_t^i = 0 \tag{A-1.21}$$

Suppose that at time t , the atomic system is brought back to the original orientation (i.e. $\mathbf{Q} = \mathbf{1}$, having only constant translational and angular velocities). Also, identify that

$$\sum_{j=1}^N m^j \hat{r}_r^j \hat{r}_s^j = -J_{rs} + \frac{1}{2} J_{pp} \delta_{ij} \tag{A-1.22}$$

Eq. (A-1.21) becomes

$$\begin{aligned}
& J_{pp}^{-1} J_{qq} \dot{Q}_{kl} - J_{pk}^{-1} J_{qq} \dot{Q}_{pl} + J_{pl}^{-1} J_{qq} \dot{Q}_{pk} + J_{pk}^{-1} J_{ls} \dot{Q}_{ps} \\
& - J_{pl}^{-1} J_{kq} \dot{Q}_{pq} + J_{pp}^{-1} J_{kq} \dot{Q}_{lq} - J_{pp}^{-1} J_{lq} \dot{Q}_{kq} + \dot{Q}_{kl} = 0
\end{aligned} \tag{A-1.23}$$

Note that in Eq.(A-1.23), only a non-singular symmetric matrix \mathbf{J} and an antisymmetric matrix $\dot{\mathbf{Q}}$ are involved. \mathbf{J} has six independent variables and $\dot{\mathbf{Q}}$ has three independent variables. No neat proof of Eq.(A-1.23) is ready in hand. But one may verify it by using nine symbols to write out the full matrix form. This part of proof is straightforward but too tedious to be shown here. Alternatively, this equation can be verified via computer software.

APPENDIX - II DERIVATION OF FICTITIOUS FORCE AND PROOF OF THE OBJECTIVITY OF THE DIFFERENCE BETWEEN THE APPARENT ACCELERATION AND THE FICTITIOUS FORCE-INDUCED ACCELERATION

From principle of objectivity, two equivalent motions in two reference frame (starred reference frame and un-starred reference frame) are related to each other by:

$$\mathbf{x}^* = \mathbf{Q}\mathbf{x} + \mathbf{b} \quad (\text{A-2.1})$$

In the first approach to derive the fictitious force, we can directly differentiate Eq.(A-2.1) with respect to time to get

$$\mathbf{v}^* = \mathbf{Q}\mathbf{v} + \dot{\mathbf{Q}}\mathbf{x} + \dot{\mathbf{b}} \quad (\text{A-2.2})$$

$$\mathbf{a}^* = \mathbf{Q}\mathbf{a} + \ddot{\mathbf{Q}}\mathbf{x} + 2\dot{\mathbf{Q}}\mathbf{v} + \ddot{\mathbf{b}} \quad (\text{A-2.3})$$

If the un-starred system is an inertial system and the starred system is a non-inertial system, we can denote the acceleration due to fictitious force in the non-inertial system as

$$\mathbf{i}^* = \ddot{\mathbf{Q}}\mathbf{x} + 2\dot{\mathbf{Q}}\mathbf{v} + \ddot{\mathbf{b}} \quad (\text{A-2.4})$$

Hence we obtain the relation:

$$(\mathbf{a}^* - \mathbf{i}^*) = \mathbf{Q}\mathbf{a} \quad (\text{A-2.5})$$

In the second approach, we rewrite Eq.(A-2.1)

$$\mathbf{x} = \mathbf{Q}^{-1}\mathbf{x}^* - \mathbf{Q}^{-1}\mathbf{b} \quad (\text{A-2.6})$$

Using the definitions of angular velocity vector and angular velocity tensor, and property of transformation matrix

$$\boldsymbol{\Omega} = \dot{\mathbf{Q}}\mathbf{Q}^T \quad (\text{A-2.7})$$

$$\boldsymbol{\Omega}(\cdot) = -\boldsymbol{\omega} \times (\cdot) \quad (\text{A-2.8})$$

$$\mathbf{Q}^{-1} = \mathbf{Q}^T \quad (\text{A-2.9})$$

and using the relation in Eq.(A-2.6), Eq.(A-2.2) can be further derived as

$$\begin{aligned} \mathbf{v}^* &= \mathbf{Q}\mathbf{v} + \dot{\mathbf{Q}}(\mathbf{Q}^{-1}\mathbf{x}^* - \mathbf{Q}^{-1}\mathbf{b}) + \dot{\mathbf{b}} \\ &= \mathbf{Q}\mathbf{v} + \boldsymbol{\Omega}\mathbf{x}^* - \boldsymbol{\Omega}\mathbf{b} + \dot{\mathbf{b}} \\ &= \mathbf{Q}\mathbf{v} - \boldsymbol{\omega} \times \mathbf{x}^* + \boldsymbol{\omega} \times \mathbf{b} + \dot{\mathbf{b}} \end{aligned} \quad (\text{A-2.10})$$

$$\mathbf{v} = \mathbf{Q}^{-1}\mathbf{v}^* + \mathbf{Q}^{-1}(\boldsymbol{\omega} \times \mathbf{x}^*) - \mathbf{Q}^{-1}(\boldsymbol{\omega} \times \mathbf{b}) - \mathbf{Q}^{-1}\dot{\mathbf{b}} \quad (\text{A-2.11})$$

Now the acceleration is obtained by differentiating Eq.(A-2.10) with respect to time:

$$\mathbf{a}^* = \dot{\mathbf{Q}}\mathbf{v} + \mathbf{Q}\mathbf{a} - \dot{\boldsymbol{\omega}} \times \mathbf{x}^* - \boldsymbol{\omega} \times \dot{\mathbf{x}}^* + \dot{\boldsymbol{\omega}} \times \mathbf{b} + \boldsymbol{\omega} \times \dot{\mathbf{b}} + \ddot{\mathbf{b}} \quad (\text{A-2.12})$$

Substituting Eq.(80) into Eq.(81), it results

$$\begin{aligned}
\mathbf{a}^* &= \dot{\mathbf{Q}}\left(\mathbf{Q}^{-1}\mathbf{v}^* + \mathbf{Q}^{-1}(\boldsymbol{\omega} \times \mathbf{x}^*) - \mathbf{Q}^{-1}(\boldsymbol{\omega} \times \mathbf{b}) - \mathbf{Q}^{-1}\dot{\mathbf{b}}\right) + \mathbf{Q}\mathbf{a} - \dot{\boldsymbol{\omega}} \times \mathbf{x}^* - \boldsymbol{\omega} \times \mathbf{v}^* + \dot{\boldsymbol{\omega}} \times \mathbf{b} + \boldsymbol{\omega} \times \dot{\mathbf{b}} + \ddot{\mathbf{b}} \\
&= \mathbf{Q}\mathbf{a} + \boldsymbol{\Omega}\mathbf{v}^* + \boldsymbol{\Omega}(\boldsymbol{\omega} \times \mathbf{x}^*) - \boldsymbol{\Omega}(\boldsymbol{\omega} \times \mathbf{b}) - \boldsymbol{\Omega}\dot{\mathbf{b}} - \dot{\boldsymbol{\omega}} \times \mathbf{x}^* - \boldsymbol{\omega} \times \mathbf{v}^* + \dot{\boldsymbol{\omega}} \times \mathbf{b} + \boldsymbol{\omega} \times \dot{\mathbf{b}} + \ddot{\mathbf{b}} \\
&= \mathbf{Q}\mathbf{a} + \left[-2\boldsymbol{\omega} \times \mathbf{v}^* - \boldsymbol{\omega} \times (\boldsymbol{\omega} \times \mathbf{x}^*) - \dot{\boldsymbol{\omega}} \times \mathbf{x}^*\right] + \left[2\boldsymbol{\omega} \times \dot{\mathbf{b}} + \boldsymbol{\omega} \times (\boldsymbol{\omega} \times \mathbf{b}) + \dot{\boldsymbol{\omega}} \times \mathbf{b}\right] + \ddot{\mathbf{b}}
\end{aligned} \tag{A-2.13}$$

If the un-starred system is an inertial system and the starred system is a non-inertial system, we can denote the acceleration due to fictitious force in the non-inertial system as

$$\mathbf{i}^* = \left[-2\boldsymbol{\omega} \times \mathbf{v}^* - \boldsymbol{\omega} \times (\boldsymbol{\omega} \times \mathbf{x}^*) - \dot{\boldsymbol{\omega}} \times \mathbf{x}^*\right] + \left[2\boldsymbol{\omega} \times \dot{\mathbf{b}} + \boldsymbol{\omega} \times (\boldsymbol{\omega} \times \mathbf{b}) + \dot{\boldsymbol{\omega}} \times \mathbf{b}\right] + \ddot{\mathbf{b}} \tag{A-2.14}$$

Again we obtain the relation as in Eq.(A-2.5). Equation (A-2.4) and Eq.(A-2.14) are equivalent expressions for fictitious force, where the difference is the use of different description of motion.

Equation (A-2.5) provides the relation between the descriptions of a motion in an inertial frame (un-starred) and a non-inertial frame (starred). Note that the fictitious force vanishes ($\mathbf{i} = 0$) in the inertial system ($\ddot{\mathbf{Q}} = \dot{\mathbf{Q}} = \ddot{\mathbf{b}} = 0$ or $\dot{\boldsymbol{\omega}} = \boldsymbol{\omega} = \dot{\mathbf{b}} = 0$). We can include the fictitious term too for the inertial system so that

$$(\mathbf{a}^* - \mathbf{i}^*) = \mathbf{Q}(\mathbf{a} - \mathbf{i}) \tag{A-2.15}$$

Furthermore, the descriptions of a motion in two non-inertial systems (*1 and *2) can be connected via the inertial system.

$$\begin{aligned}
(\mathbf{a}^{*1} - \mathbf{i}^{*1}) &= \mathbf{Q}_1 (\mathbf{a} - \mathbf{i}) \\
(\mathbf{a}^{*2} - \mathbf{i}^{*2}) &= \mathbf{Q}_2 (\mathbf{a} - \mathbf{i}) \\
(\mathbf{a}^{*2} - \mathbf{i}^{*2}) &= \mathbf{Q}_2 \mathbf{Q}_1^{-1} (\mathbf{a}^{*1} - \mathbf{i}^{*1})
\end{aligned}
\tag{A-2.16}$$

Then, we conclude that the relation Eq.(A-2.15) holds for all reference frames. Therefore, the difference between the apparent acceleration and the fictitious force-induced acceleration satisfies tensor transformation law, which means this combination $(\mathbf{a} - \mathbf{i})$ is objective.

APPENDIX - III FLOW CHART OF PROGRAM POLY

